



Strongly focused vortices and pinhole scanning microscopy

THESIS

submitted in partial fulfillment of the
requirements for the degree of

MASTER OF SCIENCE

in

PHYSICS

Author :	W.G. Stam
Student ID :	s0801542
Supervisor :	Dr. W. Löffler
2 nd corrector :	Prof. Dr. J. van Noort

Leiden, The Netherlands, December 17, 2019

Strongly focused vortices and pinhole scanning microscopy

W.G. Stam

Huygens-Kamerlingh Onnes Laboratory, Leiden University
P.O. Box 9500, 2300 RA Leiden, The Netherlands

December 17, 2019

Abstract

Over the last few decades, several methods have been explored and applied to circumvent the Abbe-Rayleigh diffraction limit, probably most importantly, stochastic super-resolution fluorescence microscopy methods.

Another possibility, relying only on linear classical optics, is to exploit optical superoscillations, and is far less explored to date. In this project we explore the use of optical vortices for super-resolution far-field imaging. For this, we investigate strongly focused optical fields using a number of theoretical methods, we implement an experiment where a micro-pinhole is scanned through the focus, and, explore spin-orbit interactions of strongly focused optical fields. We find that our micron-sized pinhole is able to discern structures much smaller than its own size and leads to an enhancement of the spin-orbit interaction. Our method can be implemented as a simple and fast tool for characterizing the intensity distribution of a focused field with high resolution.

Contents

Acknowledgements	iii
List of Abbreviations	v
List of Figures	vii
List of Tables	viii
1 Introduction	1
1.1 The Diffraction Limit and beyond	1
1.2 Vortices and superoscillations	3
1.3 Goal	6
1.4 Structure of this thesis	6
2 Theoretical Considerations	7
2.1 Vortex modes	8
2.2 Diffraction Theory	11
2.2.1 Optical Propagation	11
2.2.2 Strong Focusing	12
2.3 Computational Methods	15
2.3.1 3D Fourier transform	15
2.3.2 2D Fourier transform	16
2.3.3 Analytic solutions of the azimuthal integral	16
3 Simulations	19
3.1 Simulation Results	19
3.2 Methodology	29
3.3 Method comparison	31

4	Experimental Method & Setup	35
4.1	Mode preparation	35
4.1.1	Spatial Light Modulator (SLM)	36
4.2	Near Field Scanning Technique	41
5	Results and Discussion	43
5.1	Pinhole action	43
5.2	Spin-orbit interaction	46
5.3	Superresolution	50
6	Conclusion and Outlook	53
6.1	Conclusion	53
6.2	Outlook	53
A	Theoretical Derivations	55
A.1	Optical Propagator	55
A.2	Fraunhofer Diffraction and the 2D Fourier Transform	56
A.3	Vector Transformation Matrix	58
A.4	Full analytic solutions of the azimuthal integral	59
B	Simulation Results	63
B.1	Focal planes of LG modes	64
B.1.1	Radially and azimuthally polarized doughnut modes	73
B.2	XZ-slices of LG modes	74
C	Experimental Results	77

Acknowledgement

This report is written by a single author, but I was not alone in my endeavors. First and foremost I want to thank my supervisor Dr. Wolfgang Löffler, without whom I would not have been able to discern the richness of the physics within this research. Secondly, I want to thank Dr. Henk Snijders, who has helped me several times in the lab, and, Prof. Dr. Martin van Exter, with whom I had several helpful discussions. For feedback and comments I want to thank Jeroen van Doorn, MSc., Jonathan Pilgram, Petr Steindl, MSc., Mirjam Riedinger, MSc., and, Pim Overgaauw, MSc., who all helped shaping up this manuscript.

List of Abbreviations

OAM Orbital Angular Momentum

SAM Spin Angular Momentum

HG Hermite-Gaussian

LG Laguerre-Gaussian

SLM Spatial Light Modulator

SO Spin-orbit

lcp Left-handed circular polarization

rcp Right-handed circular polarization

List of Figures

1.1	Resolved and unresolved Airy-discs	2
1.2	Superoscillation in one dimension	4
1.3	Superoscillation in two dimensions	5
2.1	Gaussian beam	9
2.2	Higher order modes	10
2.3	Strong Focusing Geometry	13
3.1	Focused Gaussian linearly polarized	20
3.2	Focused Gaussian cross sections	21
3.3	Focused Gaussian circularly polarized	22
3.4	Focused LG ₁₀ mode circularly polarized	24
3.5	SO coupling: p -modes in cross- and z -polarization components	25
3.6	Focused LG ₂₀ mode circularly polarized	26
3.7	Focused radial and azimuthally polarized doughnut modes	28
3.8	Method comparison: Gaussian beam	31
3.9	Method comparison: Cross-sections	32
3.10	Method comparison: Duration	34
4.1	Experimental Setup	36
4.2	SLM hologram	37
4.3	Zernike polynomials	38
4.4	Fourier plane result	39
4.5	Incident field result	39
4.6	Pinhole electron micrograph	42
5.1	Comparison of pinhole action	45
5.2	20× microscope objective results	47
5.3	20× microscope objective results for LG ₁₀ modes	48

5.4	100× microscope objective results for LG ₁₀ modes	48
5.5	Polarization effect of pinhole convolution	49
5.6	100× microscope objective results for LG ₂₀ modes	51
A.1	Fraunhofer Diffraction	56
B.1	Focused Gaussian beam	64
B.2	Focused LG ₁₀ mode	65
B.3	Focused LG ₂₀ mode	66
B.4	Focused LG ₀₁ mode	67
B.5	Focused LG ₁₁ mode	68
B.6	Focused LG ₂₁ mode	69
B.7	Focused LG ₀₂ mode	70
B.8	Focused LG ₁₂ mode	71
B.9	Focused LG ₂₂ mode	72
B.10	Focused azimuthal and radial doughnut modes	73
B.11	Focused Gaussian mode	74
B.12	Focused LG ₁₀ mode	75
B.13	Focused LG ₂₀ mode	76
C.1	4×/10× microscope objective results	77
C.2	20× microscope objective results	78
C.3	50× microscope objective results	79
C.4	100× microscope objective results	80
C.5	20× and 100× Objective 2D slices	81

List of Tables

3.1	Modes in the focused components of a linearly polarized Gaussian.	21
3.2	Modes in the focused components of a circularly polarized Gaussian.	22
3.3	Modes in the focused components of a circularly polarized LG ₁₀ mode.	25
3.4	Modes in the focused components of a circularly polarized LG ₂₀ mode.	25
3.5	Modes in the focused components of a radially or azimuthally polarized doughnut mode.	27
4.1	List of microscope objectives	40
5.1	Experimental beam waist parameters	50

Introduction

1.1 The Diffraction Limit and beyond

The Abbe-Rayleigh diffraction limit has long thwarted advances in the resolution of optical microscopy [1, p. 97][2, p. 281][3, 4]. Mathematically, for any imaging system using waves, it is stated:

$$d = 1.22\lambda/2NA \quad (\text{Abbe}), \quad (1.1)$$

$$\theta = 1.22\lambda/D \quad (\text{Rayleigh}), \quad (1.2)$$

where d, θ is the minimum distance/angle one needs to resolve two spots, λ is the wavelength, NA is the numerical aperture of the system and D is the diameter of the optical element. The factor 1.22 is due to the fact that the first zero of the Airy disk or first order Bessel function appears at 1.22, see Figure 1.1.

In order to image structures smaller than the diffraction limit for optical systems, it seems like a logical choice to use electron microscopy, or other particle beams, because electrons have a much smaller wavelength, and therefore, the diffraction limit for electrons is of a much smaller scale. However, these techniques have their own complications. It is not the purpose of this thesis to discuss the limitations of electron microscopy, but rather to explore methods to circumvent the diffraction limit itself.

One might ask the question, why is there a diffraction limit at all? If we

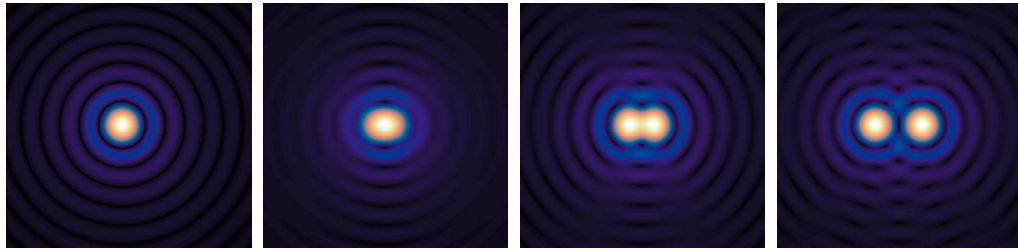


Figure 1.1: Diffraction pattern of a circular aperture illuminated by two point sources. The left figure is of a single point source. In the second figure from the left, the two point sources cannot be distinguished by conventional means because the separation is half the required factor 1.22. In the third (separation of exactly 1.22) and last figure (separation of two times 1.22) the point sources are far enough away and can be distinguished. The contrast of the pictures is enhanced by taking the 4th root of the intensity in order to see the Airy rings more clearly.

look at the second figure of Figure 1.1, we see that pattern is not a perfect Airy disk, because the light did not originate from a single point source. For example, if we would have the prior information that the light originated from two points sources, we can easily deconvolute the signal to image the two sources at a distance smaller than the resolution limit. Even without this prior information, deconvolution microscopy can calculate whether it is a single, double or multiple point source with a slightly better resolution than the Abbe limit, but this requires increasingly bright illumination [5]. We see that in principle, the Abbe limit can be beaten.

Over the last few decades, several novel techniques have been developed to image well beyond the diffraction limit. Imaging beyond the diffraction limit is called superresolution or subdiffraction imaging.

In the example, we stated that prior information on the sample can help to image beyond the diffraction limit. This is one type of superresolution and is best explained with the example of fluorescence microscopy. A strong laser pulse excites a random number of sources, which in turn emit photons that can be detected and thus localizes the active sources. Another pulse de-excites the sources and the experiment is repeated. By repeating the experiment a number of times an image can be constructed where the sources can be localized with a much better resolution than the Abbe limit. There are several distinct techniques of fluorescence microscopy beating the diffraction limit based on this principle including PALM, STORM and STED microscopy [5–7].

Stochastic techniques are not the only way to beat the diffraction limit. Another technique is near-field optical microscopy, for which methods were already proposed in the 1920s [8]. A probe, smaller than the diffraction limit, is inserted into the optical near-field of the sample and the probe is then scanned through the field. There are several types of nano-probes one could use, among others: optical fibers, small aperture probes (pinholes) or nanoparticles. Optical fibers and pinholes simply collect the field at a tiny spot, while nanoparticles scatter the light, which converts evanescent modes into propagating ones [1, Ch. 6] [9–11].

The list of superresolution techniques continues with optical needles [12], saturation microscopy, ‘perfect’ lenses constructed with meta-materials [13–15], superoscillatory filters [16, 17], and quantum entangled photons [5] and so on. See for a review [18–21]. In this thesis we shall investigate yet another type of superresolution possible, by making use of the sub-diffraction limit structure of the incident light itself. In this thesis, we will investigate the sub-diffraction limit structure of light using a pinhole. Our measurement technique is a form of superresolution technique called near-field optical microscopy [22].

1.2 Vortices and superoscillations

A couple of superresolution techniques can be based on the mathematical concept of superoscillations [4]. The idea of superoscillations originated in the 60s [23–25] and more ideas for superresolution techniques were discovered in the 50s (antenna superdirectivity). Aharonov and Berry surmised that mathematical superoscillations could be useful for physical measurements around 1990 [25–27], but only recently it became clear that far-field optical superresolution techniques almost always require superoscillations [13, 28], and that previously discovered techniques, such as antenna superdirectivity, make use of superoscillations. Superoscillations and vortices are ubiquitous in optics, even speckle patterns are full of them [29].

Superoscillations are oscillations that are faster than their fastest Fourier component. It is very easy to show that such functions exist with the following example taken from Berry [28, 30]:

$$f(x) = (\cos(x) + ia \sin(x))^N, \quad (1.3)$$

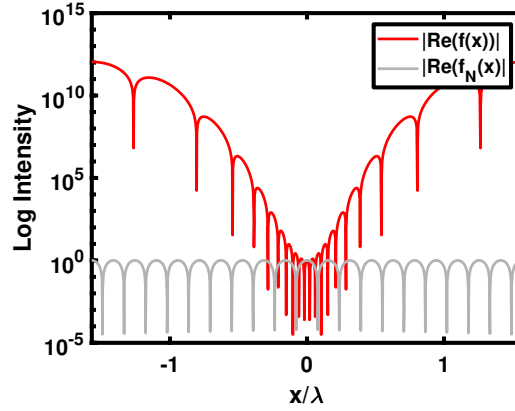


Figure 1.2: A superoscillation in one dimension. The superoscillatory function $f(x)$ is plotted together with its highest Fourier component $f_N(x)$. In this example, the parameter $a = 4$ indicates the degree of superoscillation and $N = 20$ measures the size of the area in which the superoscillation persists.

where $a > 1$ and N is a large integer. It can be shown that the highest Fourier component is:

$$f_N(x) = \exp(iNx). \quad (1.4)$$

which means the function is bandlimited. However, in Figure 1.2 we see that the function oscillates faster than its fastest Fourier component for a limited region. Two fundamental characteristics of superoscillations can already be seen in this figure. The first is that the superoscillations generally persist over a small area, and the second is that superoscillations are always accompanied by an exponentially decreasing amplitude in the area of the superoscillation together with side-lobes that have exponentially higher amplitude. The last characteristic especially complicates practical use of superoscillations.

Another example that takes us a little closer to optics is the perturbed Bessel beam taken from Berry [31, 32]:

$$g(\mathbf{r}, \ell) = J_\ell(2\pi\rho)e^{i\ell\phi} + \varepsilon J_0(2\pi\rho), \quad (1.5)$$

where ρ , ϕ are polar coordinates, ℓ is the order of the Bessel function J_ℓ and ε is a small perturbation constant. In Figure 1.3 ten ‘vortices’ are visible. In this example, the wavelength or highest Fourier component is $\lambda = 1$. The distance between two vortices is $0.2655 \cdot 2\pi/\ell = 0.16$, smaller than the wavelength. Thus, we see that the amplitude is superoscillatory. In fact, a vortex is superoscillatory by nature due to its phase distribution.

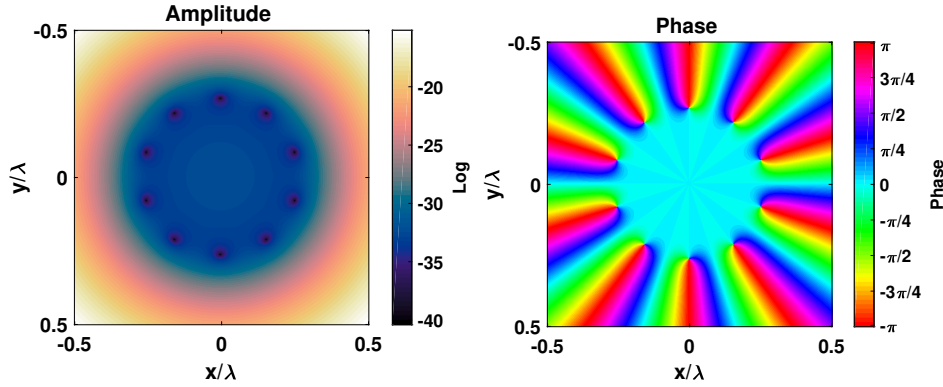


Figure 1.3: Superoscillation in two dimensions. The superoscillatory function $g(\mathbf{r}, \ell)$ is plotted with $\varepsilon = 10^{-7}$ and order $\ell = 10$. The amplitude is plotted on the left and the phase on the right.

Considering a loop around the vortex core, the phase changes more and more rapidly as we approach the core. A vortex beam generally carries orbital angular momentum because of its phase distribution. Taking a loop around the vortex core, the phase changes by $2\pi\ell$, where ℓ is the topological charge of the vortex. This is also a measure for its Orbital Angular Momentum (OAM), each photon carries $\ell\hbar$ OAM. The most commonly encountered vortex modes are Laguerre-Gaussian (LG) modes, that have a dark vortex core with topological charge ℓ . Vectorial beams can also carry Spin Angular Momentum (SAM) through their polarization. Circularly polarized light carries $s\hbar$ SAM per photon, where $s = 1$ for Right-handed circular polarization (rcp) and $s = -1$ for Left-handed circular polarization (lcp). The strong focusing regime is characterized by the fact that OAM and SAM become coupled, through Spin-orbit (SO) coupling [33–35]. In this thesis, we will see evidence of the SO coupling of LG₁₀ modes with opposite circular polarization.

Bessel beams, but also LG modes do not change their shape upon propagation [36], and their vortices are topologically stable features of the wave [4]. This can also be understood as the conservation of total angular momentum as the charge ℓ of a vortex beam can not change upon propagation. Superoscillations always operate in dark regions which is evident for vortex beams. According to Berry [4], the vortices can be arbitrarily narrow because there is no Abbe limit for dark light.

1.3 Goal

The main goal of this thesis is simple: We aim to create a beam with subdiffraction structure. In order to show that the created optical field has said structure, we need a superresolution measuring technique. We have utilized a near field scanning technique involving scanning over the field with a small aperture to characterize the intensity distribution of the field. What is or what is not subdiffraction is defined by the optical apparatus in use. In our case we will strongly focus the field with a high NA microscope objective; the size of the microscope objective will define the diffraction limit and we will test our method accordingly. Thus, we will show superresolution methods in a twofold way. Firstly, we will have produced a beam that has subdiffraction structure and secondly, we will use a superresolution measurement technique to show that it has said structure.

A second goal is to use our method to investigate the tightly focused intensity distribution of vortex modes experimentally and by numerical simulation. In the tight focusing (or strong focusing) regime the SAM of the circularly polarized light can interact with the OAM of the vortex mode through SO coupling. We will investigate the robustness of the vortex core under tight focusing for various tightly focused modes.

1.4 Structure of this thesis

After this introductory chapter there are five further chapters. In Chapter 2 the theory of strongly focused fields is treated and methods to tackle the Debye integral are discussed. These methods are implemented in simulations, of which the results are discussed in Chapter 3. The experimental method and results are discussed in subsequently Chapter 4 and Chapter 5. Finally, we conclude this thesis in Chapter 6, including an outlook on further research.

This thesis further contains three appendices. In Appendix A some details of Chapter 2 are discussed. In Appendix B and Appendix C respectively all of the simulation results and experimental results are systematically displayed.

Theoretical Considerations

In this chapter, the theory of calculating the focused field distribution is discussed. This is generally done in two steps. First, a paraxial input field is considered, and second, the field is refracted by the focusing apparatus. The action of the focusing apparatus is modeled by a geometrical construction that transforms the flat 2D incident beam propagating in the z -direction to a spherical shell propagating towards the focal point. This chapter will first set up a derivation for paraxial incident fields and subsequently, show several methods for calculating the focused field distribution.

A fundamental equation governing the field of optics is called the Helmholtz equation:

$$\left(\nabla^2 + k^2\right) \mathbf{E} = 0. \quad (2.1)$$

The Helmholtz equation is a special case of the wave equation, which can be readily derived from Maxwell's equation in vacuum, for separable solutions of the type $\mathbf{E} = \mathbf{E}_0 e^{i\omega t}$ with $\omega = c|\mathbf{k}|$ the frequency of the light. The Helmholtz equation allows plane wave and spherical wave solutions. The infinite, monochromatic, plane wave solution can be written as:

$$\mathbf{E}(\mathbf{r}, t) = \mathbf{E}_0 e^{i(\mathbf{k}\cdot\mathbf{r} - \omega t)}. \quad (2.2)$$

A general solution to the Helmholtz equation in terms of plane wave solutions is called the angular spectrum representation [37, pp. 109-114][1, pp. 38-41]:

$$\mathbf{E}(\mathbf{r}) = \iint \mathbf{E}(k_x, k_y) e^{i(k_x x + k_y y \pm k_z z)} dk_x dk_y \quad (2.3)$$

where the integral is taken over all k values to account for propagating and evanescent waves. As $k_z \equiv \sqrt{k^2 - k_\perp^2}$ becomes imaginary for $k_\perp \equiv \sqrt{k_x^2 + k_y^2} > k$, the waves are exponentially decaying and are called *evanescent* waves. The \pm -sign accounts for both forward and backward propagating waves along the z -direction [1, p. 27][38, Ch. 1][39, Ch. 8.3].

2.1 Vortex modes

An in particular useful approximation of Equation 2.1 is the paraxial approximation, resulting in solutions important in beam and resonator optics [40]. Laser beams can be prepared into a variety of exotic modes. Limiting ourselves to monochromatic and coherent light, a mode is usually characterized by its spatial distribution of intensity, phase, and polarization direction in the transverse plane.

In the paraxial regime, we can approximate Equation 2.1 by using a solution of the form $E(\mathbf{r}) = u(\mathbf{r})e^{-ikz}$, where u is a *slowly* varying function of z . Under this assumption, u solves the *paraxial Helmholtz* equation

$$\left(\nabla_\perp^2 - 2ik\partial_z \right) u = 0, \quad (2.4)$$

where $\nabla_\perp^2 \equiv \partial_x^2 + \partial_y^2$ is the transverse part of the Laplacian. A fundamental solution to this differential equation is the Gaussian beam. A scalar representation of the Gaussian beam or TEM₀₀-mode is the following:

$$u^{\text{Gauss}}(\mathbf{r}) = \frac{\sqrt{2/\pi}}{w(z)} e^{-\frac{\rho^2}{w(z)^2}} e^{-i\left(\frac{k\rho^2}{2R(z)} - \Phi(z)\right)}, \quad (2.5)$$

where ρ is the radial distance from the optical axis of the beam, z is the propagation direction, $w(z) = w_0 \sqrt{1 + (z/z_R)^2}$ is the spot size or beam waist parameter with $z_R = \pi w_0^2/\lambda$ the Rayleigh range, $R(z) = z(1 + (z_R/z)^2)$ the radius of curvature and $\Phi(z) = \arctan(z/z_R)$ is the Gouy

phase due to a small longitudinal component of the wave near the beam waist [41, pp. 153-155]. Taking a slice at an arbitrary z we see that the field is of the form $E(\mathbf{r}) \propto A e^{-\alpha r^2} e^{i\beta}$, with A, α, β constants; in essence this yields a Gaussian intensity distribution with a flat phase distribution. In principle, this fundamental Gaussian mode can be prepared in different transverse polarizations: flat linear or circular polarization or the slightly more exotic radially outward or azimuthal polarization distributions.

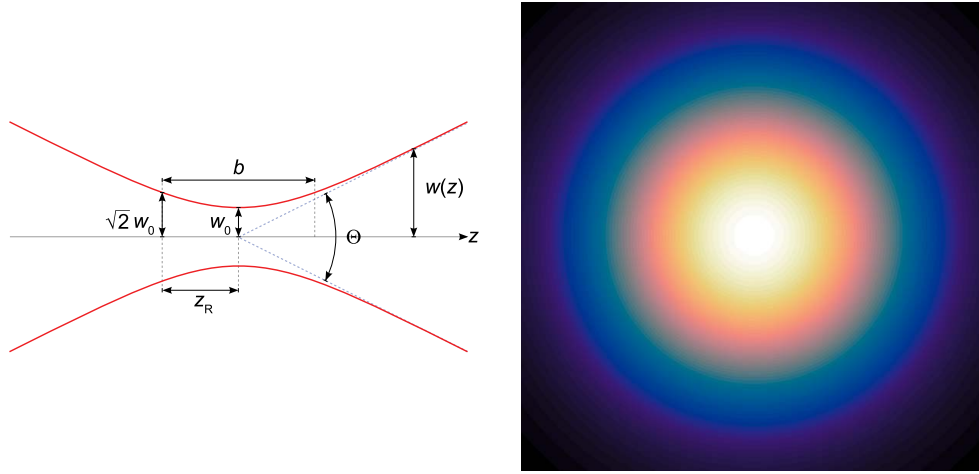


Figure 2.1: On the left the parameters of a Gaussian beam are shown. The left figure is taken from Wikipedia Gaussian Beam, accessed 14-10-2019. On the right the Gaussian intensity distribution is plotted.

At this point, we must note that the paraxial Helmholtz equation is separable in its transverse part, which leads to a complete orthogonal set of separable solutions in any basis of the two-dimensional transverse plane [42]. Since the fundamental Gaussian mode is a solution to the Helmholtz equation, which is a linear homogeneous differential equation, any combination of spatial derivatives of the fundamental mode are also solutions to the Helmholtz equation [1, p. 49]. For spatial derivatives in Cartesian coordinates, these are the so-called Hermite-Gaussian (HG) modes or TEM_{nm} modes [43]:

$$u_{nm}^{\text{HG}}(\mathbf{r}) = \frac{C_{nm}^{\text{HG}}}{w(z)} e^{-\frac{\rho^2}{w(z)^2}} e^{-i\left(\frac{k\rho^2}{2R(z)} - (N+1)\Phi(z)\right)} \cdot H_n\left(\frac{\sqrt{2}x}{w(z)}\right) H_m\left(\frac{\sqrt{2}y}{w(z)}\right), \quad (2.6)$$

where $H_{n,m}$ are (physicists') Hermite polynomials of order n, m :

$$H_0(x) = 1, \quad H_1(x) = 2x, \quad H_2(x) = 4x^2 - 2, \dots \quad (2.7)$$

n, m are mode indices, and, $N = n + m$ is the mode order. The factor

$$C_{nm}^{\text{HG}} = 2^{-(n+m)/2} \sqrt{\frac{2}{\pi n! m!}} \quad (2.8)$$

is a normalization constant. Qualitatively for a given z plane, see Figure 2.2, we see a normal Gaussian profile superimposed with $n + m$ number of nodal lines and a phase jump of π at each nodal line. Neglecting normalization and phase factors, setting $z = 0$, and rescaling the coordinates with respect to w_0 the first few modes can be written as:

$$\begin{aligned} u_{00}^{\text{HG}}(\mathbf{r}) &= e^{-\rho^2}, & u_{10}^{\text{HG}}(\mathbf{r}) &= 2xe^{-\rho^2}, \\ u_{01}^{\text{HG}}(\mathbf{r}) &= 2ye^{-\rho^2}, & u_{11}^{\text{HG}}(\mathbf{r}) &= 4xye^{-\rho^2}, \\ u_{02}^{\text{HG}}(\mathbf{r}) &= (4y^2 - 2)e^{-\rho^2}, & u_{20}^{\text{HG}}(\mathbf{r}) &= (4x^2 - 2)e^{-\rho^2}. \end{aligned} \quad (2.9)$$

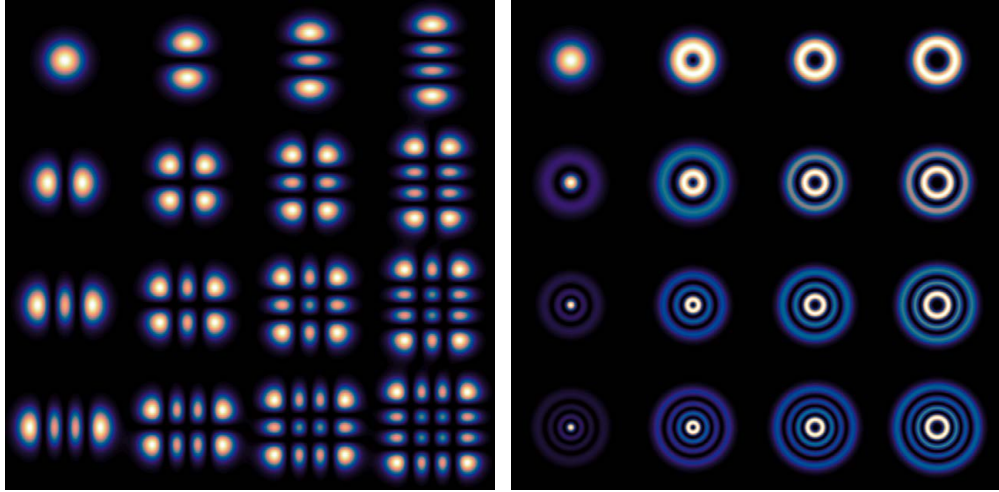


Figure 2.2: Higher-order modes. On the left are the HG modes with n, m from 0, 0 in the upper left corner to 3, 3 in the lower right corner. On the right are the LG modes with the values of ℓ, p in the same way as the HG modes.

A second set of orthogonal solutions can be obtained in polar coordinates and are called Laguerre-Gaussian (LG) modes [40]:

$$u_{\ell p}^{\text{LG}}(\mathbf{r}) = \frac{C_{\ell p}^{\text{LG}}}{w(z)} (-1)^p \left(\frac{\rho\sqrt{2}}{w(z)} \right)^{|\ell|} e^{-\frac{\rho^2}{w(z)^2}} e^{-i\left(\frac{k\rho^2}{2R(z)} - (N+1)\Phi(z)\right)} e^{-i\ell\phi} L_p^{|\ell|} \left(\frac{2\rho^2}{w(z)^2} \right), \quad (2.10)$$

where L_p^l are the generalized Laguerre polynomials

$$\begin{aligned} L_0^\ell(x) &= 1, & L_1^\ell(x) &= -x + \ell + 1, \\ L_2^\ell(x) &= \frac{x^2}{2} - (\ell + 2)x + \frac{(\ell + 2)(\ell + 1)}{2}, \dots \end{aligned} \quad (2.11)$$

p the radial, ℓ the azimuthal indices, and, $N = 2p + |\ell|$ is the mode order. Lastly, the factor

$$C_{\ell p}^{LG} = \sqrt{\frac{2p!}{\pi(p + |\ell|)!}} \quad (2.12)$$

is a normalization constant. The first few LG modes, at $z = 0$ and neglecting normalization and phase factors, can be written as:

$$\begin{aligned} u_{00}^{LG}(\mathbf{r}) &= e^{-\rho^2}, & u_{01}^{LG}(\mathbf{r}) &= (-2\rho^2 + 1)e^{-\rho^2}, \\ u_{\pm 10}^{LG}(\mathbf{r}) &= \rho e^{-\rho^2} e^{\mp i\phi}, & u_{\pm 11}^{LG}(\mathbf{r}) &= (-2\rho^3 + \rho)e^{-\rho^2} e^{\mp i\phi}, \\ u_{\pm 20}^{LG}(\mathbf{r}) &= \rho^2 e^{-\rho^2} e^{\mp 2i\phi}, & u_{\pm 21}^{LG}(\mathbf{r}) &= \rho^2(-2\rho^2 + 1 \pm 2)e^{-\rho^2} e^{\mp 2i\phi}. \end{aligned} \quad (2.13)$$

It is interesting to note that, as both families of solutions form a basis of solutions to the paraxial Helmholtz equation, in principle one can decompose the HG modes into LG modes. In other words, there exists a relation between the HG and LG modes [44–48]. For instance, we have:

$$u_{\pm 10}^{LG}(\mathbf{r}) = u_{10}^{HG} \mp iu_{01}^{HG}, \quad (2.14)$$

$$u_{\pm 20}^{LG}(\mathbf{r}) = u_{20}^{HG} - u_{02}^{HG} \mp 2iu_{11}^{HG}. \quad (2.15)$$

LG modes are the quintessential vortex modes. At the center, due to the factor $e^{-i\ell\phi}$ there is a vortex of topological charge ℓ which means that each photon carries $\ell\hbar$ Orbital Angular Momentum (OAM). In this project, we have mainly used the LG₁₀ and LG₂₀ modes to investigate the properties of vortices.

2.2 Diffraction Theory

2.2.1 Optical Propagation

The Huygens-Fresnel principle states that every point of a wave-front may be considered as a secondary point source (Huygens). The optical field at

any point can be calculated as a sum over these secondary point sources, taking into account (Fresnel) that the secondary wavelets interfere. For any wavefront \mathcal{S} we can calculate the optical field at a point \mathbf{r} by integrating over the field at the wavefront together with the optical propagator or Green's function $G(\mathbf{r}, \mathbf{r}')$ [1, pp. 45-47]:

$$E_{\text{out}}(\mathbf{r}) = \iint_{\mathcal{S}} G(\mathbf{r}, \mathbf{r}') E_{\text{in}}(\mathbf{r}') dS. \quad (2.16)$$

where the optical propagator is given as (see Section A.1):

$$G(\mathbf{r}, \mathbf{r}') = \frac{e^{iks}}{i\lambda s} \quad (2.17)$$

and $s = |\mathbf{r} - \mathbf{r}'|$ is the vector between the position \mathbf{r} of the field to be calculated and the position \mathbf{r}' of the incident field on the surface. Given a surface \mathcal{S} on which an incident field is defined, the above equation calculates the resulting diffracted field at a given location \mathbf{r} .

Two geometries for the surface \mathcal{S} are prevalent for calculating the diffracted field. One of these geometries is well known and yields the field of Fourier physics. On the condition that the aperture (surface) is small with respect to the propagation length ($z \gg x', y'$), it can be derived (see Section A.2) that the diffracted field is simply a Fourier transform of the incident field on the aperture. The method of Fourier analysis to calculate the diffracted field is very powerful, not only because one can use fast Fourier algorithms to calculate the diffracted field, but also because in many cases it is possible to calculate the exact solution in this approximation. This indicates that it might be useful to try something similar in the strong focusing regime.

The second geometry is that of a spherical surface for calculating a strongly focused field, for which the above approximation obviously does not hold, and is discussed next.

2.2.2 Strong Focusing

In the strong focusing regime, we must use another geometrical construction to calculate the field near the focus, and the vector nature of the field can no longer be neglected. A strong focusing apparatus obeying the Abbe sine condition [49]:

$$\rho = f \sin \theta \quad (2.18)$$

is often modeled as in Figure 2.3. An incident paraxial field \mathbf{E}_{in} is transformed at a spherical surface into the transmitted field \mathbf{E}_{t} after which it propagates towards the focal point to become the focused field \mathbf{E}_{out} . The first transformation is a rather simple transformation to do mathematically, but we should note that this is simply a model of how a microscope objective focuses the light. In reality, the microscope objective consists of multiple lenses together transforming the field approximately in the manner we are describing here.

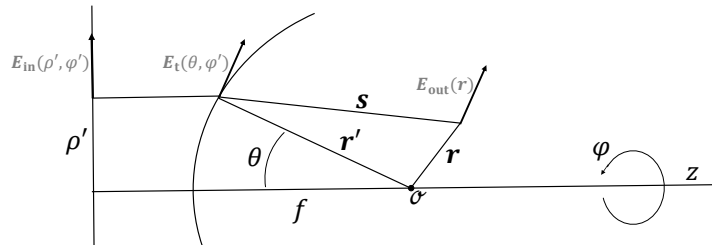


Figure 2.3: Geometrical construction in the strong focusing regime. The vectors \mathbf{E}_{in} , \mathbf{E}_{t} and \mathbf{E}_{out} are drawn at general coordinates. The vector \mathbf{E}_{in} is defined on the flat surface and the vector \mathbf{E}_{t} on the spherical surface. The contribution of the drawn \mathbf{E}_{t} at those coordinates is drawn as an example vector for \mathbf{E}_{out} .

Vector transformation at the lens

Consider the incident vectorial beam in cylindrical coordinates ρ, ϕ . Then, at the lens, the radial direction is transformed to the polar direction and multiplied with the Fresnel coefficient t_p . The azimuthal direction remains unchanged but is multiplied with the Fresnel coefficient t_s [1, pp. 21-22]. This can be expressed as follows [1, pp. 58-59]:

$$\mathbf{E}_{\text{t}} = (t_s(\mathbf{E}_{\text{in}} \cdot \hat{\phi})\hat{\phi} + t_p(\mathbf{E}_{\text{in}} \cdot \hat{\rho})\hat{\theta}) \sqrt{\cos \theta}, \quad (2.19)$$

where the term $\sqrt{\cos \theta}$ is an apodization term due to energy conservation [1, pp. 57-58]. We can also express this transformation as a matrix:

$$\mathbf{E}_{\text{t}} = \mathbf{M}\mathbf{E}_{\text{in}}\sqrt{\cos \theta}. \quad (2.20)$$

where the matrix M is given in Cartesian coordinates as (see Section A.3):

$$\mathbf{M} = \frac{1}{2} \begin{pmatrix} t_s + t_p \cos \theta - (t_s - t_p \cos \theta) \cos 2\phi & -(t_s - t_p \cos \theta) \sin 2\phi \\ -(t_s - t_p \cos \theta) \sin 2\phi & t_s + t_p \cos \theta + (t_s - t_p \cos \theta) \cos 2\phi \\ -2t_p \sin \theta \cos \phi & -2t_p \sin \theta \sin \phi \end{pmatrix}. \quad (2.21)$$

This matrix transforms the two transverse polarization directions of the incident field \mathbf{E}_{in} onto three polarization directions of the transmitted field \mathbf{E}_t .

Propagation toward the focal point

In the second step the transmitted field is propagated towards the focus. To calculate the focused field, we use the geometry in Figure 2.3 where the transmitted field $E_t(\mathbf{r}')$ is defined on a sphere with curvature f [1, pp. 45-55][39, Ch. 8.8][50–52]. Let \mathbf{s} denote again the distance vector $\mathbf{r}' - \mathbf{r}$ between the points on the sphere \mathbf{r}' and the image point \mathbf{r} . According to Equation 2.16:

$$\mathbf{E}_{\text{out}}(\mathbf{r}) = e^{-ikf} \int_S \mathbf{E}_t(\mathbf{r}') \frac{e^{iks}}{i\lambda s} dS. \quad (2.22)$$

It is conventional to set the 0 of the phase in the origin instead of at the spherical surface, hence the term e^{-ikf} . In this case, we will expand s near f , assuming that we are near the focus, i.e. \mathbf{r} small. Note that $f^2 = x'^2 + y'^2 + z'^2$ by construction so that we can write:

$$\begin{aligned} s &= \sqrt{(x - x')^2 + (y - y')^2 + (z - z')^2} = \sqrt{f^2 + r^2 - 2(\mathbf{r} \cdot \mathbf{r}')} \\ &= f \sqrt{1 + \frac{r^2 - 2(\mathbf{r} \cdot \mathbf{r}')}{f^2}} \approx f + \frac{r^2 - 2(\mathbf{r} \cdot \mathbf{r}')}{2f}. \end{aligned} \quad (2.23)$$

We see that in linear approximation in \mathbf{r} we obtain $s = f - \frac{\mathbf{r} \cdot \mathbf{r}'}{f}$ with a dimensionless error of the size of $r^2/2f^2$ (in terms of f). If we plug this into the integral (with using in the denominator again $s \approx f$), we obtain:

$$\mathbf{E}_{\text{out}}(\mathbf{r}) = -\frac{i}{\lambda f} \int_S \mathbf{E}_t(\mathbf{r}') e^{-ik\frac{\mathbf{r} \cdot \mathbf{r}'}{f}} dS. \quad (2.24)$$

This integral is called the Debye-Wolf integral [39, p. 485][53, 54]. The next step is that we perform a coordinate transformation $dS = f^2 d\Omega$, where $d\Omega$ is an integral over the solid angle. We can write $\mathbf{k} = k\mathbf{r}'/f$ such that:

$$\mathbf{E}_{\text{out}}(\mathbf{r}) = -\frac{if}{\lambda} \int_{\Omega} \mathbf{E}_t(\theta, \phi) e^{-i\mathbf{k} \cdot \mathbf{r}} d\Omega. \quad (2.25)$$

Note the similarity of this integral to Equation 2.3 of the angular spectrum representation.

2.3 Computational Methods

To recapitulate, calculating a strongly focused field which is focused obeying the Abbe sine condition is done in three steps.

1. The paraxial incident field \mathbf{E}_{in} is fully characterized using an appropriate basis of modes and polarization.
2. The incident field is transformed into the transmitted field \mathbf{E}_t according to Equation 2.19.
3. The Debye integral is evaluated to obtain \mathbf{E}_{out} near the focus.

The Debye integral cannot be solved analytically, except for maybe a few pathological cases. One can, of course, calculate the integral numerically, but it is computationally expensive, as for each coordinate in three-dimensional space a two dimensional integral must be solved. However, there are several techniques that can decrease the computational time. One such technique relies on converting the integral into a Fourier transform, and is discussed in Subsection 2.3.1 and Subsection 2.3.2. More elegantly, the azimuthal integral can be solved analytically, which reduces the two-dimensional integral into a small set of one-dimensional ones. This method is discussed in Subsection 2.3.3. In the next chapter, we will compare the simulations of the different methods of various input fields.

2.3.1 3D Fourier transform

The Debye integral can be turned into a three dimensional integral over all space by simply multiplying the integrand with a delta function [50, 51, 55, 56]

$$\mathbf{E}_{\text{out}}(\mathbf{r}) = -\frac{if}{\lambda} \int_{\mathcal{V}} \mathbf{E}_t(\mathbf{r}) \delta(|\mathbf{r}| - 1) e^{-i\mathbf{k}\cdot\mathbf{r}} dV. \quad (2.26)$$

Note the resemblance to the 3D Fourier transform:

$$f(\mathbf{k}) = \int_{\mathcal{V}} f(\mathbf{r}) e^{-i\mathbf{k}\cdot\mathbf{r}} \frac{dV}{(2\pi)^{3/2}}. \quad (2.27)$$

Thus, we find:

$$\mathbf{E}_{\text{out}}(\mathbf{r}) = -\frac{if}{\lambda}(2\pi)^{3/2}\mathcal{F}[\mathbf{E}_t(\mathbf{r})\delta(|\mathbf{r}|-1)](k) \quad (2.28)$$

This means that we can implement fast Fourier algorithms and quickly calculate the focused field.

2.3.2 2D Fourier transform

As we only have a field defined on a spherical shell, it is more natural to proceed with a two-dimensional Fourier transform [52, 57]. Considering the on shell angles θ and ϕ , we may transform these into the cylindrical coordinates of the paraxial input field before the lens:

$$\begin{aligned} r &= \sin \theta, & dr &= \cos \theta d\theta, \\ \phi &= \phi, & d\phi &= d\phi, \end{aligned} \quad (2.29)$$

such that

$$d\Omega = \sin \theta d\theta d\phi = \frac{r dr d\phi}{\cos \theta} = \frac{dx dy}{\cos \theta}. \quad (2.30)$$

Filling this into Equation 2.25, we find:

$$\mathbf{E}_{\text{out}}(\mathbf{r}) = -\frac{if}{\lambda} \int_{\Omega} \mathbf{E}_t(\theta, \phi) e^{-i\mathbf{k}\cdot\mathbf{r}} \frac{dx dy}{\cos \theta}. \quad (2.31)$$

Taking E_t zero for angles larger than the opening angle we can extend the integral over the plane and obtain the 2D Fourier integral

$$\begin{aligned} \mathbf{E}_{\text{out}}(\mathbf{r}) &= -\frac{if}{\lambda} \int \frac{\mathbf{E}_t(\theta, \phi) e^{-ik_z z}}{\cos \theta} e^{-i(k_x x + k_y y)} dx dy \\ &= -\frac{if}{\lambda} \mathcal{F}_{2D} \left[\frac{\mathbf{E}_t(\theta, \phi) e^{-ik_z z}}{\cos \theta} \right] (k_x, k_y). \end{aligned} \quad (2.32)$$

2.3.3 Analytic solutions of the azimuthal integral

The Debye integral (Equation 2.25) can be partially solved analytically for the azimuthal integral [1, pp. 59-68]. First, let us write this integral in terms

of the coordinates of the sphere ϕ' and θ' :

$$\mathbf{E}_{\text{out}}(\rho, \phi, z) = -\frac{if}{\lambda} \int_0^{\theta_{\max}} \int_0^{2\pi} \mathbf{E}_t(\theta', \phi') e^{ik(z \cos \theta' + \rho \sin \theta' \cos(\phi' - \phi))} \sin \theta' d\phi' d\theta'. \quad (2.33)$$

We will outline how to solve this integral for a linearly x -polarized Gaussian as incident field. In Section A.4, the full expressions for up to mode order 2 are written down. Let us assume the Fresnel coefficients are 1 for simplicity. We can now express the transmitted field \mathbf{E}_t on the spherical surface as

$$\mathbf{E}_t(\theta, \phi) = \mathbf{E}_{\text{in}}(\theta, \phi) \frac{\sqrt{\cos \theta}}{2} \begin{pmatrix} 1 + \cos \theta - (1 - \cos \theta) \cos 2\phi \\ -(1 - \cos \theta) \sin 2\phi \\ -2 \cos \phi \sin \theta \end{pmatrix}. \quad (2.34)$$

Next, let us calculate the incident field \mathbf{E}_{in} for the Gaussian in terms of the spherical coordinates (f, θ, ϕ) , where $x = f \sin \theta \cos \phi$, $y = f \sin \theta \sin \phi$ by construction:

$$u^{\text{Gauss}}(\mathbf{r}) = e^{-f^2 \sin^2 \theta / w_0^2}. \quad (2.35)$$

Note that inserting these equations into Equation 2.33, there is always the following common factor

$$f_W(\theta) \equiv e^{-f^2 \sin^2 \theta / w_0^2} \sqrt{\cos \theta} \sin \theta e^{ikz \cos \theta} \quad (2.36)$$

that we will write as such. The azimuthal integral can now be evaluated with the following two standard integrals:

$$\begin{aligned} \int_0^{2\pi} \cos(n\phi) e^{ix \cos(\phi' - \phi)} d\phi' &= 2\pi(i^n) J_n(x) \cos(n\phi), \\ \int_0^{2\pi} \sin(n\phi) e^{ix \cos(\phi' - \phi)} d\phi' &= 2\pi(i^n) J_n(x) \sin(n\phi), \end{aligned} \quad (2.37)$$

where J_n is the n th-order Bessel function. In principle, what is left is an integral over the single variable θ . As in Novotny [1, p. 61], it is useful to introduce these abbreviations for the following integrals:

$$\begin{aligned} I_{00} &= \int_0^{\theta_{\max}} f_W(\theta) (1 + \cos \theta) J_0(k\rho \sin \theta) d\theta, & I_{01} &= \int_0^{\theta_{\max}} f_W(\theta) \sin \theta J_1(k\rho \sin \theta) d\theta, \\ I_{02} &= \int_0^{\theta_{\max}} f_W(\theta) (1 - \cos \theta) J_2(k\rho \sin \theta) d\theta. \end{aligned} \quad (2.38)$$

Note that these integrals are still functions of the output coordinates (ρ, z) meaning that we still have to perform each integral numerically for each field point that we want to evaluate. Using these abbreviations, we can write down the focused fields:

$$E_x^{\text{Gauss}}(\mathbf{r}) = -\frac{ikf}{2} \begin{pmatrix} I_{00} + I_{02} \cos 2\varphi \\ I_{02} \sin 2\varphi \\ -2iI_{01} \cos \varphi \end{pmatrix} \quad (2.39)$$

All other LG and HG modes can be obtained in a similar manner. The only difference between the higher order modes and the Gaussian is a polynomial in $\sin \phi$ and $\cos \phi$ for which the integral can be solved using Equation 2.37. See Section A.4 for full expressions of the HG modes up to mode order $N = 2$.

Simulations

This chapter discusses the simulations that were used to calculate the focused field distributions. First, the main simulation results are discussed for the Gaussian, LG₁₀ and LG₂₀ modes. The cross- and z-polarization components intensities are explained and characterized by means of SO coupling. Next, the different methods used to simulate are explained and compared.

3.1 Simulation Results

The theoretical problem at hand is how to calculate the Debye integral, which is valid for strongly focused fields close to the focal point:

$$\mathbf{E}_{\text{out}}(\mathbf{r}) = -\frac{if}{\lambda} \int_{\Omega} \mathbf{E}_t(\theta, \phi) e^{-i\mathbf{k}\cdot\mathbf{r}} d\Omega, \quad (3.1)$$

In the previous chapter it is outlined how to tackle this integral. In this chapter, we will present the numerical results for parameters similar to the experiment, which will be discussed in the next two chapters:

$$\begin{aligned} \text{NA} &= 0.9, & \lambda &= 0.637 \mu\text{m}, \\ f &= 2000 \mu\text{m}, & w_0 &= 1000 \mu\text{m}. \end{aligned} \quad (3.2)$$

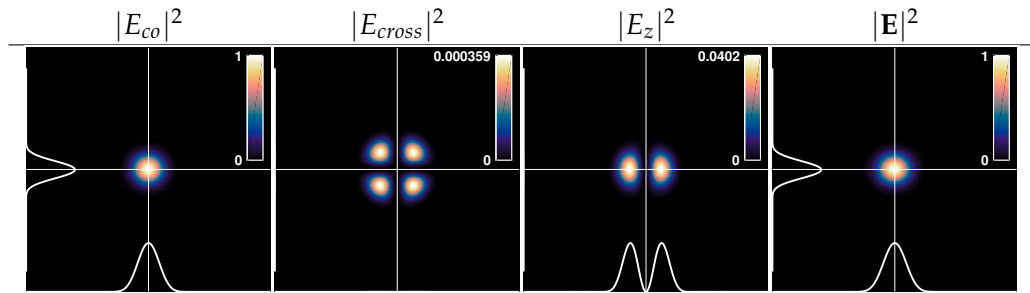


Figure 3.1: Focused field of a linearly polarized Gaussian beam. From left to right are plotted the intensity profiles of the co-, cross-, z-polarization components, and lastly the total intensity.

In this chapter, all figures have been simulated on a $5 \times 5 \mu\text{m}$ grid with 512×512 points. The 2D CZT method (see Section 3.2) has been used unless stated otherwise in the figure caption. Lastly, the total intensity has been normalized in each figure.

Focused field of an incident linearly polarized Gaussian beam

Let us first address the strongly focused Gaussian profile of a linear polarized beam depicted in Figure 3.1. The first most obvious observation is that the cross- and z-components are non-zero. The co-polarization component is the vector component parallel to the incident beam and the cross-polarization component is the vector component orthogonal, but also transverse. Finally, the z-polarization component is the axial component in the direction of propagation. The polarization vector of the incident beam is rotated inwards at the spherical shell on which it is projected, yielding the resulting components. While these cross- and z-polarization components are always slightly non-zero in real beams, this effect only becomes appreciably large in the case of strong focusing. The intensity distribution of the focused field is elongated along the axis of incident polarization, which in this case is the x -direction, see Figure 3.2.¹

Important to note is that the incident field is linearly polarized with a Gaus-

¹This is a known result, found in various sources [1, 43, 57, 58]. Gross [57] reports different values of the intensities of the cross and axial vector components, although the qualitative behavior is the same. The numbers are not the same because they are in fact also dependent on the beam waist w_0 and the focal length f , which we have chosen to fit the experiment.

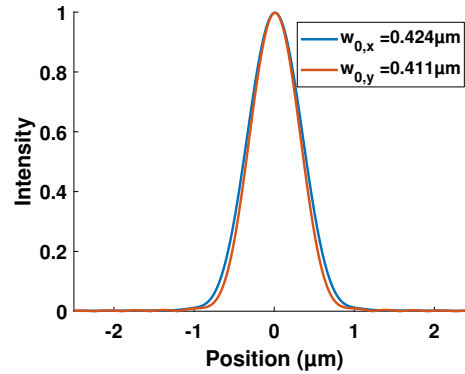


Figure 3.2: Cross-sections along the x - and y -polarization direction of the total intensity drawn with red and blue curves respectively, showing that the total intensity distribution is slightly elongated along the polarization axis.

sian intensity profile, such that the separability in Cartesian coordinates of the field for each vector component is not affected. Therefore, we must obtain HG modes in the cross- and z -polarization components. A common theme that we already discover here is that compared to the co-polarization component, the z -polarization component differs 1 in mode order and 2 in the cross-polarization component. Tabulated:

Table 3.1: Modes in the focused components of a linearly polarized Gaussian.

	mode	$N = n + m$
co	HG ₀₀	0
cross	HG ₁₁	2
z	HG ₀₁	1

where the first column indicates what kind of mode we find in the component of the focused field, and the second column lists the mode order N .

Focused field of an incident circularly polarized Gaussian beam

If we give the incident Gaussian beam circular polarization we find similar results, see Figure 3.3. In the rotational basis — co- and cross-polarization now mean right-hand and left-hand in the circular basis — we obtain the higher order LG modes in cross- and z -polarization components instead of HG modes, and thus, the total intensity remains circularly symmetrical. The

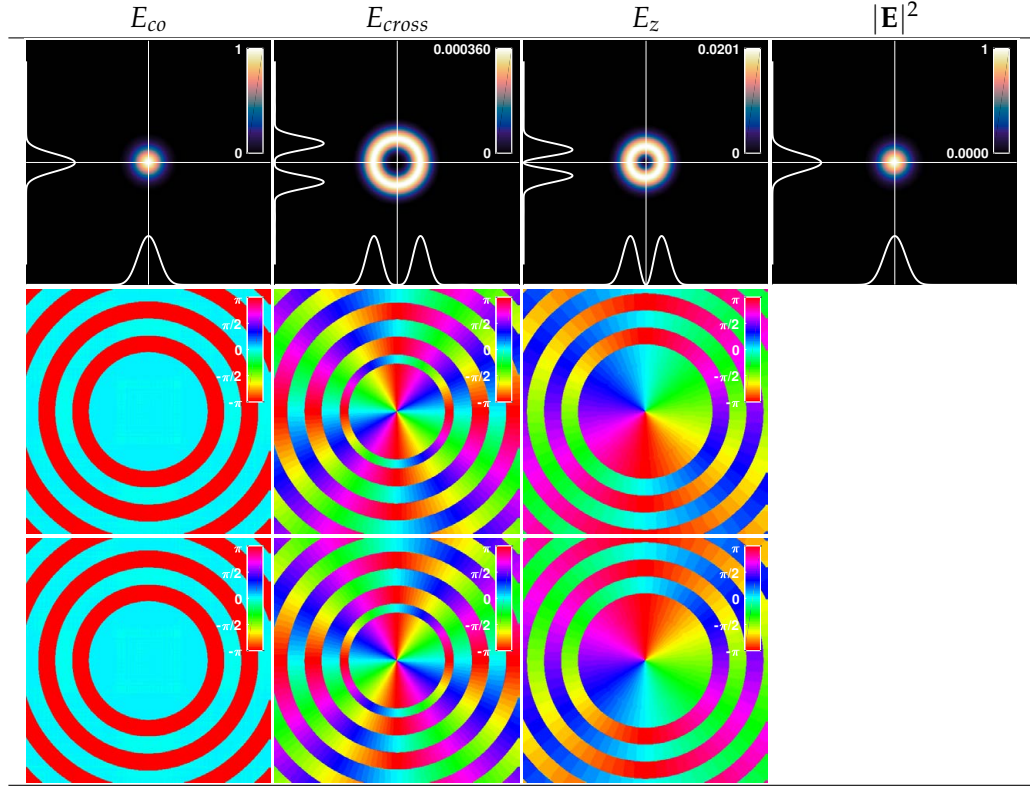


Figure 3.3: Focused field of a circularly polarized Gaussian beam. From left to right are plotted the intensity profiles of the co-, cross-, z-polarization components, and lastly the total intensity. The upper row depicts the equal intensity distributions for both lcp and rcp directions. The second and third row depict the phase distribution of the lcp and rcp directions respectively.

co-polarization component for the focused lcp mode is left hand circular $|L\rangle = (|x\rangle + i|y\rangle)/\sqrt{2}$ and the cross-polarization component is right hand circular $|R\rangle = (|x\rangle - i|y\rangle)/\sqrt{2}$ and vice versa for the focused rcp mode. Again, we have a mode order difference of 2 for the cross-component and 1 for the z-component:

Table 3.2: Modes in the focused components of a circularly polarized Gaussian.

	$s = -1$	$s = 1$	$N = \ell + 2p$
co	LG ₀₀	LG ₀₀	0
cross	LG ₋₂₀	LG ₂₀	2
z	LG ₋₁₀	LG ₁₀	1

where the $s = -1$ and $s = 1$ columns indicate the circular polarization

of the incident beam and list the modes found in the focused field components. The difference between lcp and rcp can be understood in terms of SO coupling. For circular polarized light each photon carries $s\hbar$ SAM, where lcp carries $-\hbar$ and rcp $+\hbar$ SAM per photon. This SAM is partially converted into OAM in case of tight focusing, yielding a vortex core in the z-polarization component [59]. We see this difference in the handedness of the vortex core phase distribution. For lcp, we obtain a LG mode with azimuthal index $\ell = -1$ in the z-polarization component and $\ell = -2$ in the cross-polarization component, and for rcp, we have a LG mode with azimuthal index $\ell = +1$ in the z-polarization component and $\ell = +2$ in the cross-polarization component.

Focused field of an incident circularly polarized LG₁₀ mode

This fact can be made even more clear for the focused circularly polarized LG₁₀ modes where the handedness dictates whether the vortex core survives [60, 61]. Adding the components together to a total intensity for the focused lcp mode, we see that the vortex core of the beam is no longer exactly zero² due to the conversion of SAM into OAM [33, 34]. This profound effect is something we will also encounter in our experiments. For rcp we see in Figure 3.4 that SAM and OAM are parallel and add. For lcp the SAM and OAM are anti-parallel and subtract. Moreover, when the OAM is lowered in this way by SO coupling, the phase distribution acquires a circular phase step that looks very much like the phase step of an LG mode with radial index $p = 1$, see Figure 3.5. In fact, this is a general rule we observed. The mode order is always 2 and 1 higher in the cross-component respectively z-component, while the azimuthal index is also always lowered by 2 and 1 in case of opposite OAM and SAM. The radial index p is increased accordingly. This is further corroborated by higher-order radial modes, see Appendix B for a full list of calculated focus fields.³ We can write for the different polarization components [33]:

$$\text{left hand circular:} \quad \ell_{foc} = (\ell + s + 1), \quad (3.3)$$

$$\text{right hand circular:} \quad \ell_{foc} = (\ell + s - 1), \quad (3.4)$$

$$\text{z:} \quad \ell_{foc} = (\ell + s), \quad (3.5)$$

²See also the simulations of Zhao et al. [35].

³This ‘rule’ was already discovered for the axial component by Klimov [62] and the vortex order for each component has been calculated by Bliokh [33]. To the best of our knowledge, the increase in the radial index p has not been discovered.

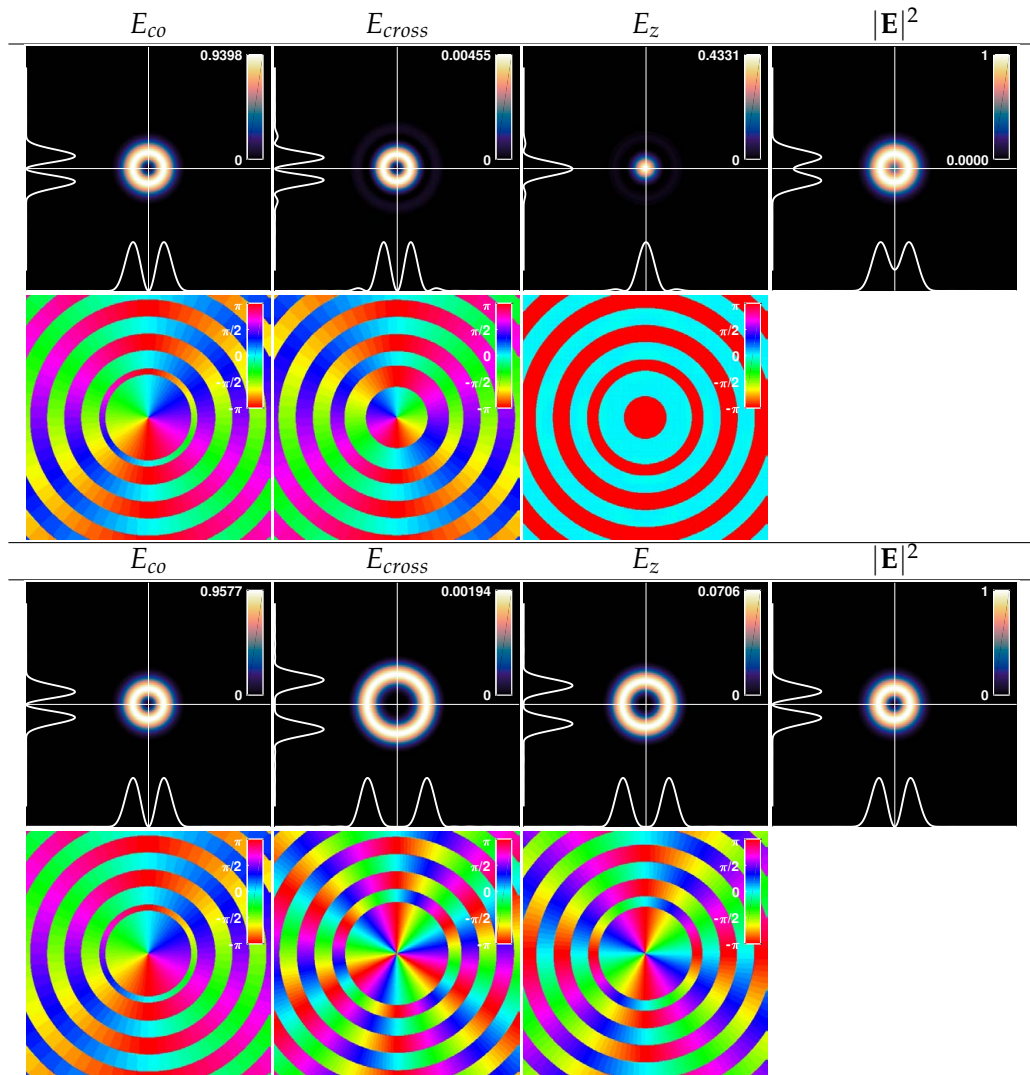


Figure 3.4: Focused field of a circularly polarized LG_{10} mode. The top two rows depict the focused field distributions of the lcp LG_{10} mode, and the bottom two rows of the rcp LG_{10} mode, similar to the figures above.

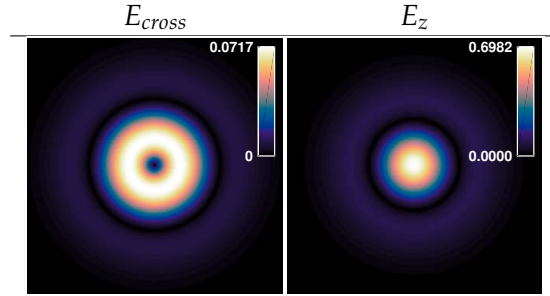


Figure 3.5: SO coupling: p -modes in cross- and z -polarization components. The low intensities are enhanced by plotting the absolute value of the amplitude instead of the intensity.

where l_{foc} is the vortex order of the focused field component. In terms of modes, tabulated for the incident circularly polarized LG_{10} mode, we observe:

Table 3.3: Modes in the focused components of a circularly polarized LG_{10} mode.

	$s = -1$	$s = 1$	$N = \ell + 2p$
co	LG_{10}	LG_{10}	1
cross	LG_{-11}	LG_{30}	3
z	LG_{01}	LG_{20}	2

Focused field of an incident circularly polarized LG_{20} mode

For the LG_{20} mode, the story is much the same. However, because the z -polarization component of the lcp does have a vortex core, we see that the vortex is much more robust. We must note that the cross-polarization component does not have a vortex core and therefore we have a tiny on-axis intensity even for the LG_{20} mode. Tabulated for the LG_{20} mode:

Table 3.4: Modes in the focused components of a circularly polarized LG_{20} mode.

	$s = -1$	$s = 1$	$N = \ell + 2p$
co	LG_{20}	LG_{20}	2
cross	LG_{02}	LG_{40}	4
z	LG_{-11}	LG_{30}	3

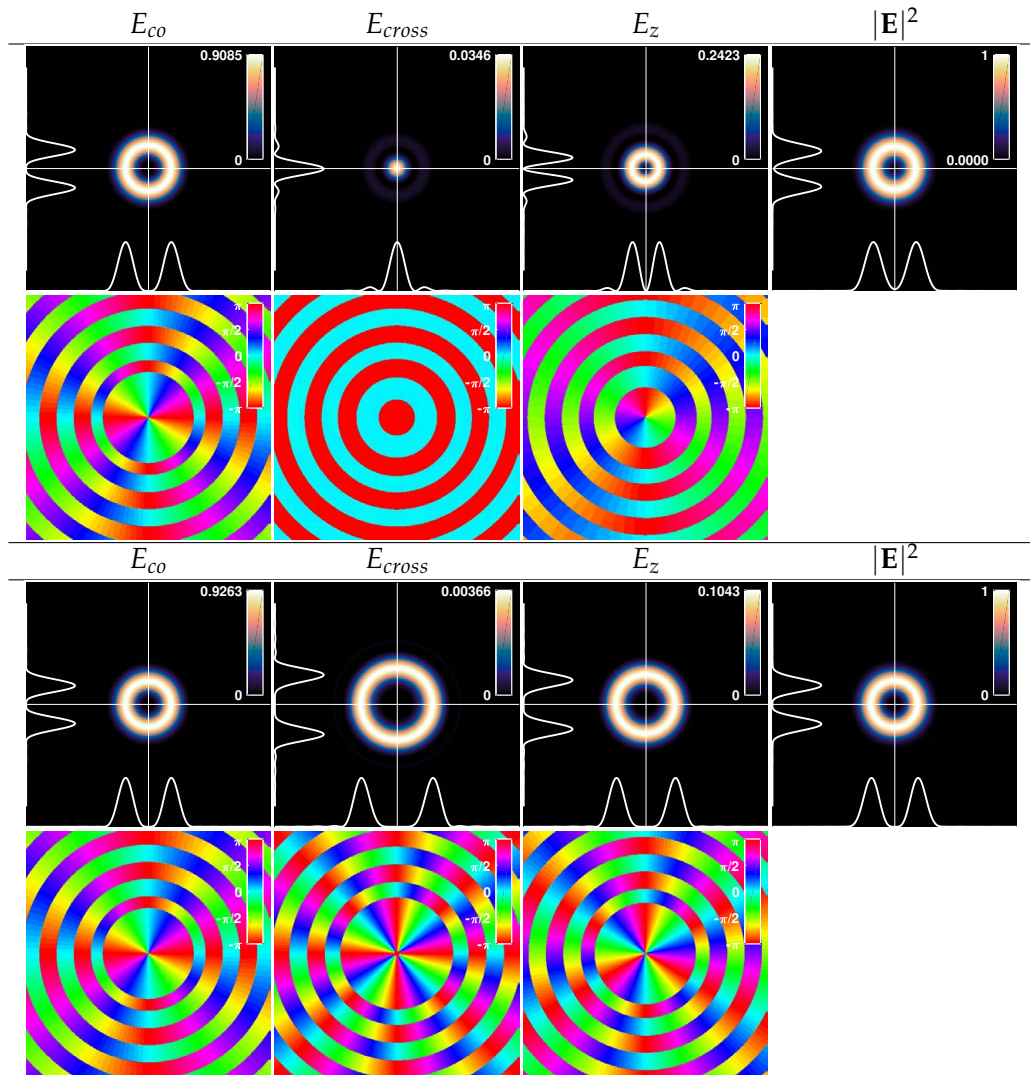


Figure 3.6: Focused field of a circularly polarized LG_{20} mode. The top two rows depict the focused field distributions of the lcp LG_{20} mode, and the bottom two rows of the rcp LG_{20} mode.

Focused fields of the incident radially and azimuthally polarized doughnut modes

Apart from the modes already discussed, we found the following modes in the literature [1, 57, 58, 63].⁴ The radially polarized doughnut mode can be written as:

$$u^{\text{rad}} = \frac{\rho}{w_0} e^{-\rho^2/w_0^2} \hat{\rho} = u_{10}^{\text{HG}} \hat{x} + u_{01}^{\text{HG}} \hat{y}, \quad (3.6)$$

and the azimuthally polarized doughnut mode as:

$$u^{\text{azi}} = \frac{\rho}{w_0} e^{-\rho^2/w_0^2} \hat{\phi} = -u_{01}^{\text{HG}} \hat{x} + u_{10}^{\text{HG}} \hat{y}. \quad (3.7)$$

These modes are interesting because they do not disrupt the cylindrical symmetry of the focusing apparatus. Furthermore, the total intensity of the focused radially polarized mode shows not a Gaussian but is more similar to a top-hat profile. Basically, the flat phase doughnut mode in the radial E_ρ polarization component is combined with a large LG_{01} profile (distinguishable from the Gaussian mode by its phase structure) in the z -component. For the azimuthally polarized mode, due to symmetry considerations, the z -polarization component cancels completely and we are left with the azimuthal E_ϕ polarization component's doughnut profile. The leftover profile in the z -polarization component in the figure is due to numerical errors in MatLab. We see the leftover fourfold intensities of the z components of the focused HG_{01} and HG_{10} modes.

Table 3.5: Modes in the focused components of a radially or azimuthally polarized doughnut mode.

	radial mode	N	azimuthal mode	N
x	HG_{10}	1	HG_{01}	1
y	HG_{01}	1	HG_{10}	1
z	LG_{01}	2	—	—

⁴Our results are essentially the same as in the literature, indicating that the methods used to simulate the focused field are correct.

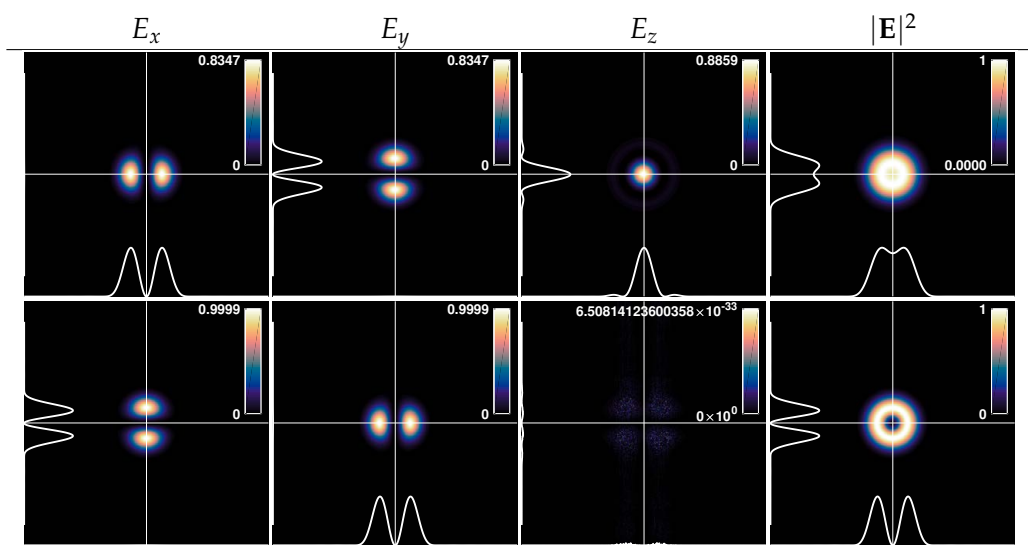


Figure 3.7: Focused fields of the radial and azimuthally polarized doughnut modes. The top row depicts the focused field distributions of the radially polarized doughnut mode, and the bottom row of the azimuthally polarized doughnut mode. The phases of the transverse polarization components in a Cartesian basis are similar to that of the z-polarization component of a focused Gaussian mode: The HG_{10} phase step together with the radial phase steps observed earlier. (Not plotted.)

3.2 Methodology

In order to calculate Equation 2.25:

$$\mathbf{E}_{\text{out}}(\mathbf{r}) = -\frac{if}{\lambda} \int_{\Omega} \mathbf{E}_t(\theta, \phi) e^{-i\mathbf{k}\cdot\mathbf{r}} d\Omega, \quad (3.8)$$

as outlined in Section 2.3, several different methods can be utilized. We have programmed four distinct methods with MATLAB.

The first most obvious method is by performing brute force integration (BF). For each position it calculates the integral over each element in the 2D array $\mathbf{E}_t(\theta, \phi)$, or rather $\mathbf{E}_t(\rho, \phi)$, multiplied by the exponent $e^{-i\mathbf{k}\cdot\mathbf{r}}$, where \mathbf{k} can be written as:

$$\mathbf{k} = k_0 \begin{pmatrix} \rho \cos(\phi) \\ \rho \sin(\phi) \\ f \sqrt{1 - (\rho/f)^2} \end{pmatrix}, \quad (3.9)$$

This method is obviously slow, but yields the most trustworthy results. Fortunately, it is easy to adapt the method to only calculate a single plane, which is adequately fast.

The second method is by performing the azimuthal integral analytically [1, 58]. This method is implemented in two equivalent ways. Namely, the first way (AA1) predefines the integrals from Subsection 2.3.3 for each mode. The second (AA2) calculates a symbolic expression for the full vectorial field in terms of a single integral over θ by means of a small algorithm. It is possible to set up an algorithm for this because the azimuthal integral is always of the same form. The algorithm first calculates the formula for the transmitted field \mathbf{E}_t and rewrites it in such a way that there are only linear terms of $\sin n\phi'$ and $\cos n\phi'$. After this step, it performs the integral by substituting each term of $\sin n\phi'$ with $2\pi(i^n)J_n(k_0\rho \sin \theta) \sin \phi$ according to Equation 2.37.

The reason for separating the analytical methods AA1 and AA2, that solely differ in the way they are implemented, is because the AA2 method is a bit slow in its implementation due to the way MATLAB converts the symbolic expressions to a 2D or 3D grid. However, due to the algorithmic nature, the AA2 method is superior over the AA1 method, as it is easy to make errors in the lengthy mathematical expressions that we see in Section A.4.

The AA1 method, in fact, becomes slower for higher-order modes because it needs to calculate more and more integrals, such that the AA2 method is better overall. The AA methods are faster than the BF method, as they only need to integrate over a single variable, instead of two for the BF method.

Next are the two Fourier implementations discussed in Subsection 2.3.1 and Subsection 2.3.2. These are implemented with a Chirp-Z transform (CZT) instead of a Fast Fourier Transform (FFT), as we are only interested in a small volume near the focus for which the Debye integral is valid. Cutting off the Fourier transform at small values greatly increases the speed of the transform. These two methods are implemented as a 2D transform (2DCZT) [52] and a 3D transform (3DCZT) [50, 51, 55]. These methods are extremely fast in their implementation but are hard to program correctly. For instance, for the 3DCZT method, it is very difficult to implement a spherical shell that is infinitesimally thin on a Cartesian grid. For both, there are probably issues with sampling. Another downside is that these methods need to use 3D grids (or z planes for the 2DCZT method) in order to work, which limits the sampling size when programmed on an ordinary computer.

For each method, the symbolic expressions for HG and LG modes are generated by making use of a Rodrigues' formula for Laguerre and Hermite polynomials.⁵ For the BF, 2DCZT and 3DCZT methods, the input fields are calculated as followed. The input modes are calculated on a 2D array and subsequently set in a cell array of length 2 denoting the transverse polarization directions. In the second step, Equation 2.19 is performed upon the input field to obtain the transmitted field $\mathbf{E}_t(\mathbf{r}')$. Subsequently, in the third step, the method as described above is implemented. The resultant object is a 3D array with 3 cells denoting the 3 polarization directions.

Implementing these methods, we ran into many problems. As of now, not all problems have been addressed. To give an idea of some of the issues that are left, the methods will be compared to one another in the next section.

⁵See Wikipedia Rodrigues' Formula, consulted 18-11-2019.

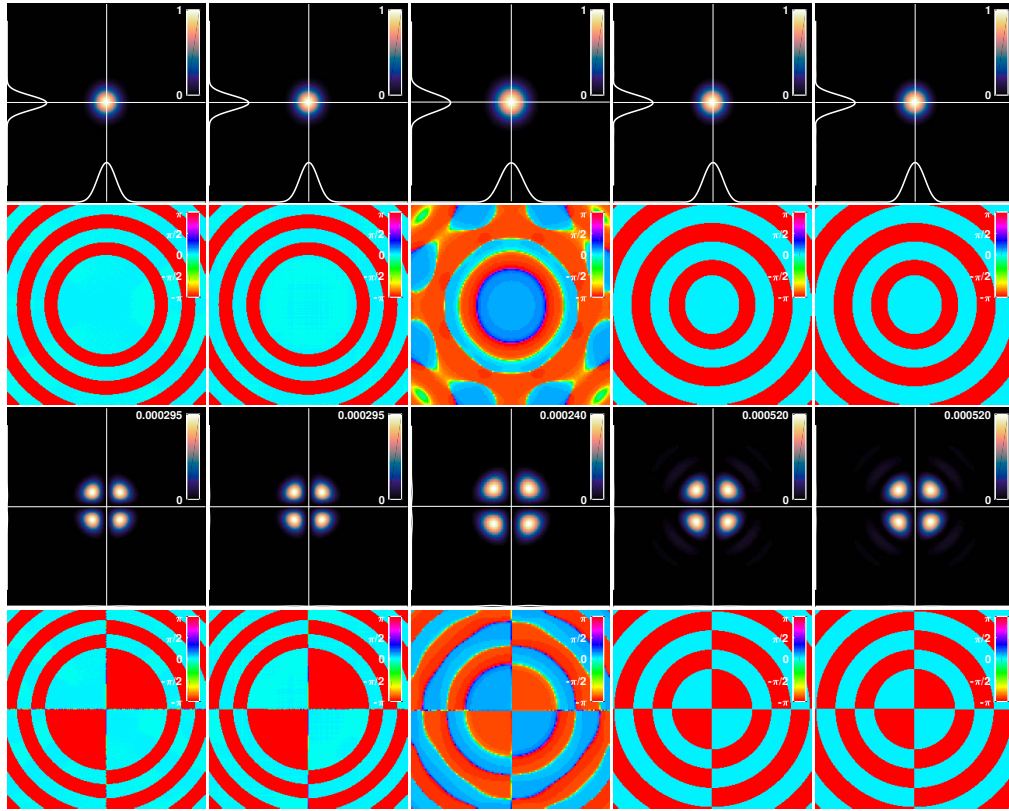


Figure 3.8: Method comparison: Focused linearly polarized Gaussian mode, with $NA = 0.9$, $f = 2$ mm and $w_0 = 1000$. From left to right are the BF, 2DCZT, 3DCZT, AA1 and AA2 methods. The top two rows depict the co-polarization component and the lower two rows depict the cross-polarization component.

3.3 Method comparison

To compare the methods, we will use a fundamental Gaussian mode prepared in one transverse polarization direction. First, we look at a single z -plane at $z = 0$, where all methods seem to function properly. In Figure 3.8 we observe that qualitatively, the results are very similar. Indeed, both AA1 and AA2 output the exact same results, as they eventually use the same expressions. Between the other methods, there are some differences that are hardly visible in the intensities, but more clearly in the phase. As we can see, the phase of the 3DCZT method does not accurately mimic that of the other methods. However, we see that this only happens in an area with low intensities, where phase information is less important. Between the BF, 2DCZT and both AA methods, we observe that the circular phase

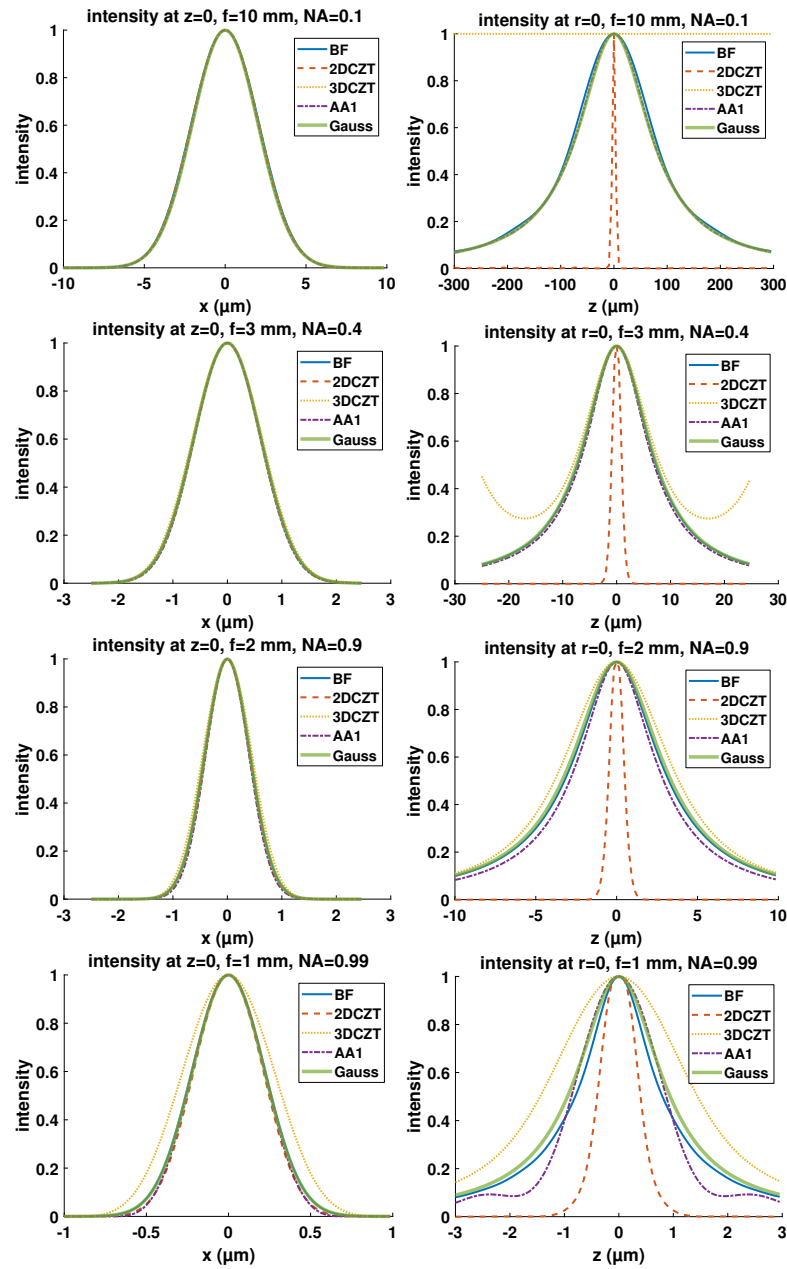


Figure 3.9: Method comparison: Cross-sections for different values of NA and f . All figures depict the co-polarization component of a focused linearly polarized Gaussian beam. The left column is the intensity of a cross-section at $z = y = 0$ and the right column at $\rho = 0$. The results of the four methods together with a Gaussian intensity are plotted. The Gaussian is the green curve and is plotted with the expected beam waist.

steps are not at the same distance. This indicates a small difference in the way the incident beam is cut off on the aperture, yielding a different phase step ring structure.

To investigate the differences in more detail, cross sections are taken in Figure 3.9 at the $z = y = 0$ line on the left and on the optical axis on the right. For the focal plane, we see that the methods almost exactly agree for small NA, but that for high NA small differences appear, with the largest differences in the 3DCZT method. All in all, in the focus, all methods accurately simulate a focused Gaussian with the expected beam waist:

$$w_{0,\text{focus}} = \frac{\lambda}{\pi \arctan(w_{0,\text{input}}/f)}. \quad (3.10)$$

For the axial cross-section, large differences appear. The 2DCZT method does not accurately simulate a Gaussian at all and we believe that sampling and/or spacing issues are the reason this method is failing. The 3DCZT method fails for low NA, where the sampling of the spherical shell becomes more difficult. For the other methods, BF most accurately simulates the Gaussian, while the AA1 method runs into problems for extremely high NA.

Finally, the methods differ in the amount of time they take to calculate the focus field. The main motivation to use the difficult to implement CZT methods is because they speed up the computational time significantly. In the Figure 3.10, we see that the BF method is slowest, followed by AA2, AA1, 3DCZT and finally, the fastest is the 2DCZT method. We also see that regardless of the number of points, the AA2 method takes a couple of seconds to initialize. This is due to the computation of the symbolic expressions. We note that the initialization of the AA2 method can be made significantly faster if it would not be programmed in MatLab.

All in all, if one is interested in the $z = 0$ plane, the 2DCZT method has yielded the best results. It is very fast and yields essentially the same results as the BF method. For 3D results, the only method that accurately simulates the Gaussian for very high NA was the brute force method, with large deviations in the other methods. For the CZT methods, one should be very careful about sampling in case of low NA.

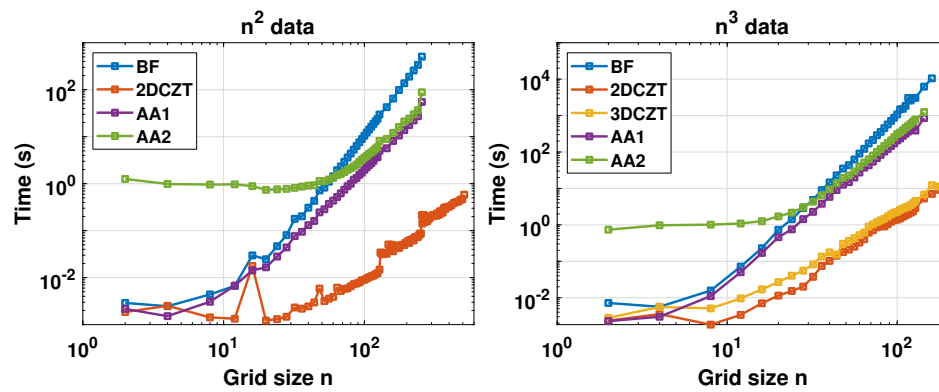


Figure 3.10: Comparison of calculation duration for the algorithms. On the y-axis is the time in seconds, on the x-axis is the length of the grid. Left: Calculation on a $n \times n$ square grid. Right: Calculation on a $n \times n \times n$ grid. Note that the 3DCZT can only be implemented on a 3D grid. The sampling size of the incident beam is kept the same. This means for the BF, 2DCZT methods an $n \times n$ input field grid and for the AA methods an n long θ vector that is integrated over.

Experimental Method & Setup

This chapter explains in detail the experimental procedures of this research. The first part of the chapter describes the setup, of which the schematic can be found in Figure 4.1, and by which method the focused vortex modes are generated. The second part describes the near field scanning technique utilized to measure the intensity distribution of the strongly focused beam.

4.1 Mode preparation

The optical field is produced by a 637 nm laser diode (Thorlabs LP637-SF70) transmitted through a single mode fiber (P1-630A-FC-2). The mode is directed into a horizontal polarization by the subsequent $\lambda/2$ -plate (633 nm-AR) and linear polarizer (LPVIS100-MP). At this stage, together with a laser diode controller (LDC 205 C and TED 200 C), absorptive filters regulate the total intensity of the beam.

After a, solely practically important, mirror, a 50/50 non-polarizing beam-splitter (BS016) creates a new perpendicular optical path on which the phase tailored beam will operate.

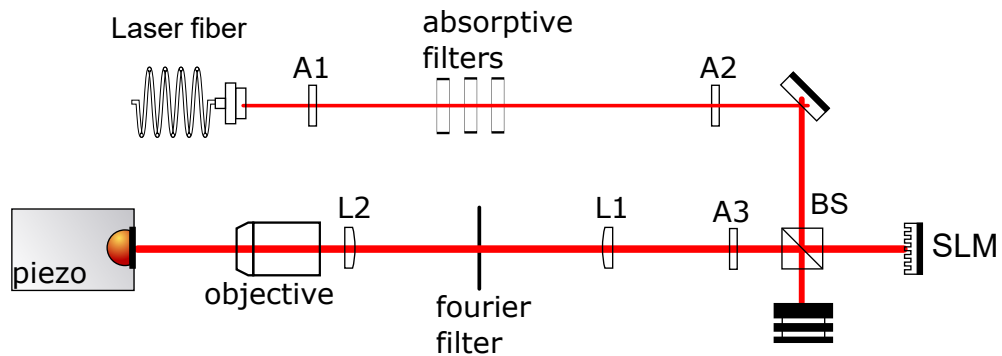


Figure 4.1: Schematic of the complete setup. Distances not to scale. The elements $A1$ and $A2$ are respectively a $\lambda/2$ -plate and a polarizer. The element $A3$ is either empty or a waveplate. Lens $L1$ has a focal length of 20 cm and is the first lens of the telescope. Lens $L2$ has a focal length of 20 cm or 40 cm and is the second lens of the telescope.

4.1.1 Spatial Light Modulator (SLM)

On one side of the beamsplitter, shortly thereafter, a SLM is placed. The SLM is a very useful device to create vortex modes [64–66]. In principle, a SLM modulates only the phase distribution of the incident light and reflects a beam of which the phase is tailored.

A SLM is made out of liquid crystal pixels of which the height can be varied separately. It can thus modulate the phase by creating a height pattern on the grid of liquid crystals. Reflected light obtains a phase shift $2\pi\lambda/h$ where h is the relative height of the pixels. In this way, it is possible to create phase vortices for LG modes, phase discontinuity lines for HG modes and so on. See Figure 4.2(b).

By creating a blazed grating pattern, see Figure 4.2(a), the SLM can also function as a blazed grating to eliminate zeroth-order reflection. By making judicious use of a blazed grating reflection, one could also use a SLM as an amplitude modulator [67–70]. However, judging from the Fourier plane images shown in Figure 4.4, this was not deemed necessary.

The SLM utilized (Holoeye Pluto series) has an active area of $15.36 \text{ mm} \times 8.64 \text{ mm}$ and a pixel size of $8 \mu\text{m}^2$. The SLM is operated by a LabView program written by Wolfgang Löffler, and, at a tilt of 0.004 rad such that it operates at a first-order reflection instead of zeroth-order direct reflection.

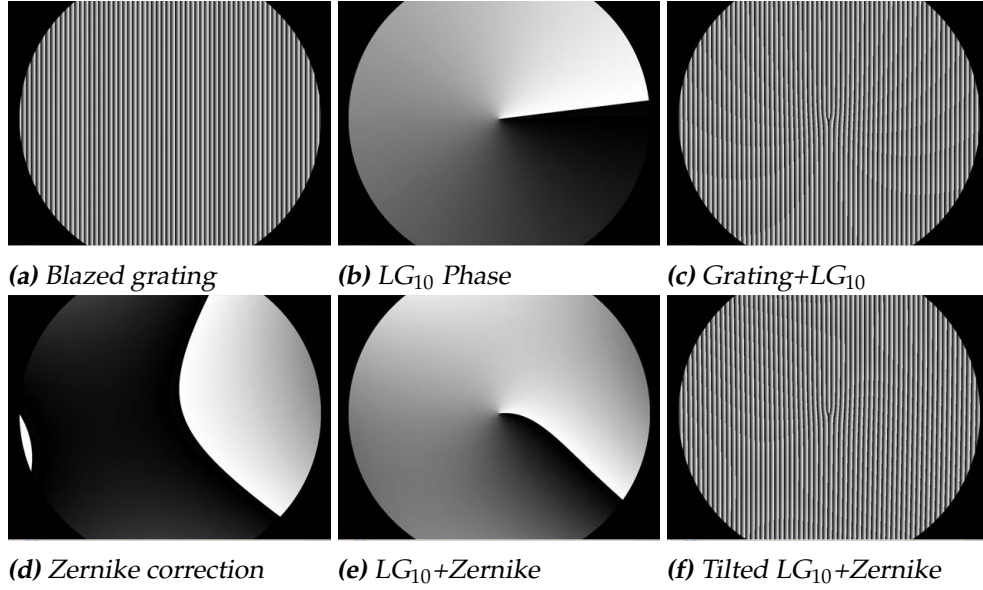


Figure 4.2: This figure shows the phase ramp programmed onto the Spatial Light Modulator (SLM). Figure (a) shows a simple phase ramp to emulate a blazed grating. (b) shows the phase vortex structure of an LG_{10} mode. Figure (c) adds these two elements together to the familiar pitchfork structure. In the lower row, the Zernike corrections are added. Figure (d) shows only the Zernike correction, (e) includes the LG_{10} phase ramp and Figure (f) shows the final resultant phase structure of a tilted LG_{10} mode with Zernike corrections.

Apart from the phase structure of the LG modes, the phase distribution is tailored by making use of the Zernike polynomials (an orthogonal basis of the unit disc) [56]. They are defined in cylindrical coordinates as:

$$Z_n^m(\rho, \phi) = \begin{cases} R_n^m(\rho) \cos(m\phi) & m \geq 0, \\ R_n^{-m}(\rho) \sin(-m\phi) & m \leq 0, \end{cases} \quad (4.1)$$

with

$$R_n^m(\rho) = \begin{cases} \sum_{k=0}^{(n-m)/2} \frac{(-1)^k (n-k)!}{k! \left(\frac{n+m}{2}-k\right)! \left(\frac{n-m}{2}-k\right)!} \rho^{n-2k} & n-m \text{ even,} \\ 0 & n-m \text{ odd.} \end{cases} \quad (4.2)$$

The first few Zernike polynomials are the following and can be used for what is written on the right:

$$\begin{aligned} Z_0^0 &= 1 && \text{Piston, (0)} \\ Z_1^{-1} &= 2\rho \sin(\phi) && \text{Y-tilt, (1)} \end{aligned}$$

$Z_1^1 = 2\rho \cos(\phi)$	X-tilt, (2)
$Z_2^{-2} = \sqrt{6}\rho^2 \sin(2\phi)$	Oblique astigmatism, (3)
$Z_2^0 = \sqrt{3}(2\rho^2 - 1)$	(De)focus, (4)
$Z_2^2 = \sqrt{6}\rho^2 \cos(2\phi)$	Vertical astigmatism, (5)
$Z_3^{-3} = \sqrt{8}\rho^3 \sin(3\phi)$	Vertical trefoil, (6)
$Z_3^{-1} = \sqrt{8}(3\rho^3 - 2\rho) \sin(\phi)$	Vertical coma, (7)
$Z_3^1 = \sqrt{8}(3\rho^3 - 2\rho) \cos(\phi)$	Horizontal coma, (8)
$Z_3^3 = \sqrt{8}\rho^3 \cos(3\phi)$	Oblique trefoil. (9)

As we can see in Figure 4.3 and in the equations above, especially polyno-

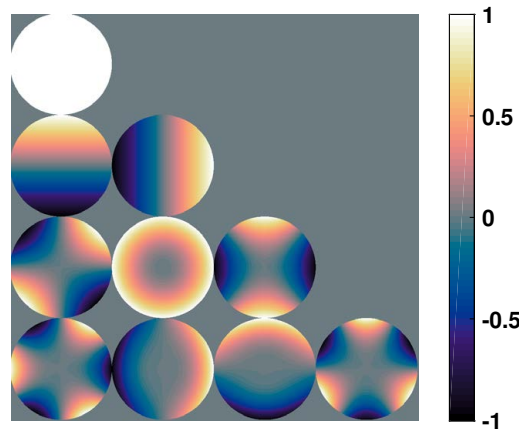


Figure 4.3: The first nine Zernike polynomials according to the OSA/ANSI index.

mials 3, 5, 6 and 9 are useful for shaping the phase distribution. The final utilized SLM hologram can be seen in Figure 4.2(f).

The parameters of the SLM program are adjusted by visual guidance with a camera (Spiricon SP620U) at the Fourier plane of a 1 m lens (, which is placed instead of lens L1 in Figure 4.1 together with a mirror to divert the beam to the camera). The results of this can be seen in Figure 4.4.

The element A3 of Figure 4.1 controls the polarization direction of the phase tailored beam. For horizontal polarization, it is empty. For vertical polarization a $\lambda/2$ -plate at 45 degrees is inserted, or a $\lambda/4$ -plate at ± 45 degrees for rcp or lcp.

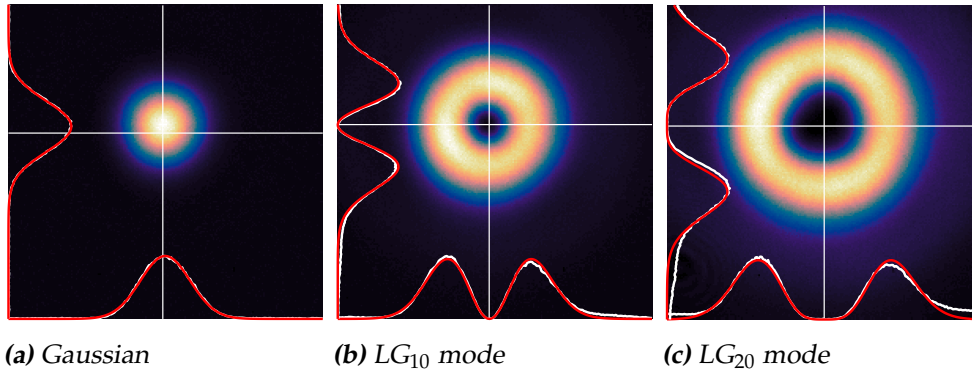


Figure 4.4: The three fundamental modes in the Fourier plane. The white curves are cross-sectional plots at the white lines. The red curves are fits of the respective modes. The images are of an area of $880 \times 880 \mu\text{m}$.

Lastly, a telescope is installed with a set of planar-convex lenses of which the first is a 20 cm lens and the second either 20 cm or 40 cm, depending on the need to increase the beam diameter. At the Fourier plane of the first lens, a large pinhole ($\varnothing 0.3 \text{ mm}$) is used as a Fourier filter and to select the correct order of the blazed grating of the SLM. In Figure 4.5 the modes are depicted just before entering the microscope objective.

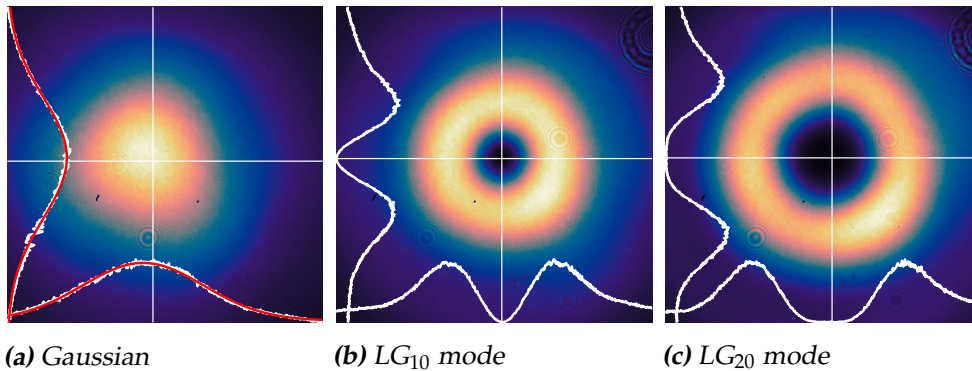


Figure 4.5: The three fundamental modes incident on the objective. The images are of an area of $2.62 \times 2.62 \text{ mm}$. The curves have been fitted in MATLAB. The beam waist parameter w_0 of the Gaussian is calculated with the Spiricon software to be $w(z) = 1.07 \pm 0.01 \text{ mm}$ for the 20 cm lens and $w(z) = 1.98 \pm 0.02 \text{ mm}$ for the 40 cm lens (not plotted).

After the mode preparation, the field is focused into a small volume with a microscope objective. Several different objectives have been utilized to perform the focusing, see Table 4.1. The microscope objectives have different apertures. Therefore, for the $4\times$, $10\times$, and $20\times$ objectives we have

used the 40 cm lens and for the 50 \times and 100 \times objectives we have used the 20 cm lens.

Table 4.1: List of utilized microscope objectives and their specifications. M stands for magnification, NA is the numerical aperture, WD the working distance, f the focal length and D the diameter of the opening aperture. All of the objectives are infinity corrected. One can calculate the focal length by the specified tube lengths L and the magnification with $f = L/M$. For Olympus $L = 180$ mm and for Nikon $L = 200$ mm.

	M	NA	WD (mm)	f (mm)	D (mm)
Olympus Plan N	4 \times	0.1	4.9	45	9.8
Olympus Mplan N	10 \times	0.25	10.6	18	11.7
Olympus Plan	20 \times	0.40	1.2	9	9.2
Nikon LU Plan EPI	50 \times	0.80	1.0	4	6.8
Nikon TU Plan APO	100 \times	0.90	2.0	2	4.7

4.2 Near Field Scanning Technique

To characterize the strongly focused light it is insufficient to simply place a camera to capture the light, as the pixel size of a camera is much bigger than the structure of the beam under investigation. Therefore, we have utilized a tiny probe that locally measures the field distribution. By scanning this probe with an XYZ-piezo stage, one can make a full 3D reconstruction of the intensity distribution of the strongly focused field.

To measure the intensity at a given location of the strongly focused field, we insert a $\varnothing 1.3(2)$ μm pinhole, see Figure 4.6 for an electron micrograph of the pinhole. The total intensity transmitted through the pinhole is measured with a photodiode (PDA 36A-EC), usually with a gain of 70 dB, at each scanning location. The pinhole is fixed on top of the photodiode.

The pinhole is fixed on top of a piezo stage (PI P-611 3S, controlled with PI E-517) with a $100 \times 100 \times 100$ μm scan range and resolution of 1 nm that functions as the scanning apparatus. For increased versatility, the piezo-cube is placed on top of a translation stage with a $25 \times 25 \times 25$ mm scan range and a resolution of 95 nm (controlled by a Newport ESP 300).

All these objects are operated with a LabView program written for this project. This program has two important features, besides scanning over the required volume. The first is that it can combine the translation stage and piezo cube to increase the scan range of the piezo cube with minimal loss of resolution. Secondly, the voltage from the photodiode is measured by averaging over 10 samples where the sample rate is 1000 Hz with an RSE configuration.¹

¹See the National Instruments website for more information, accessed 27-9-2019.

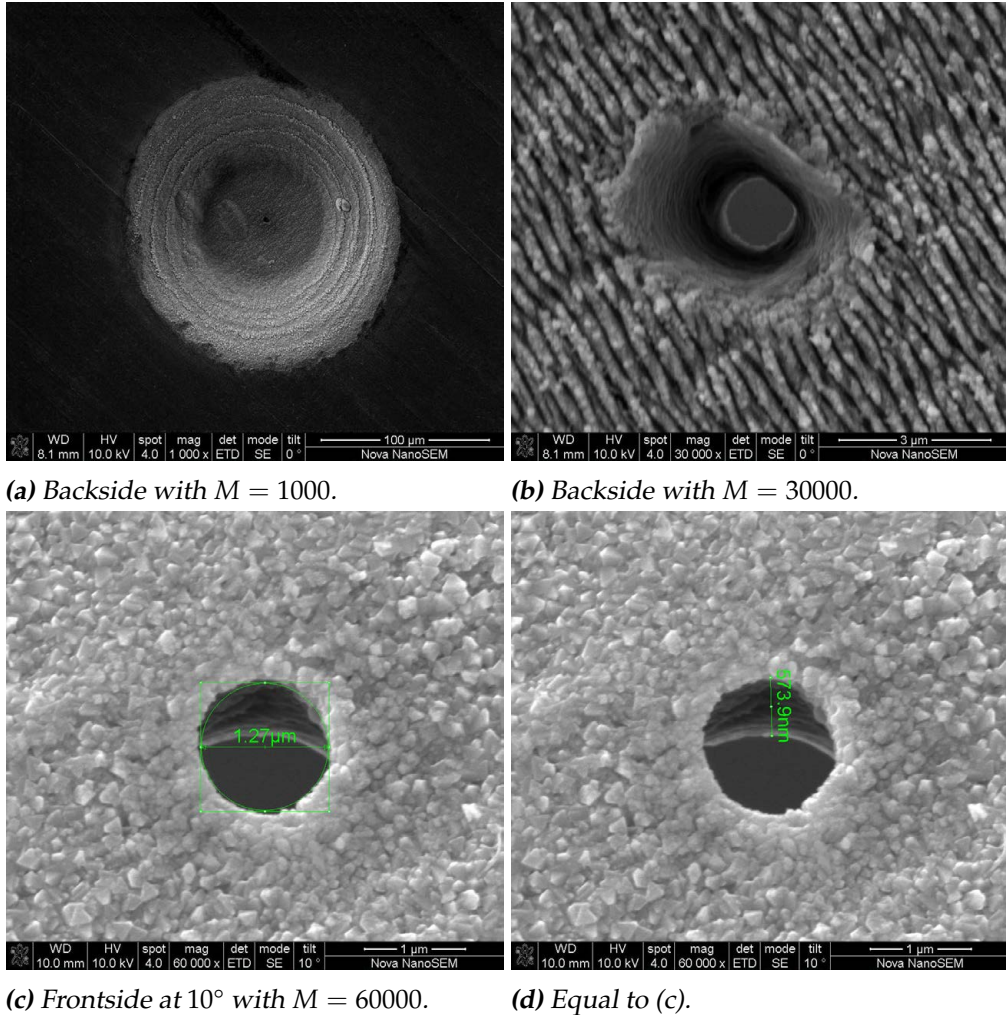


Figure 4.6: Electron micrographs of the pinhole. The roughly $1\ \mu\text{m}$ pinhole is manufactured by Thorlabs and made out of 302 stainless steel. Figure (a) shows the backside at a magnification of 1000. The plate appears to be etched away in a cone shape in order to decrease the thickness of the otherwise $0.6\ \text{mm}$ plate at the pinhole. Figure (b), at a magnification of 30000, shows the pinhole ‘tunnel’ most clearly. We also see that the backside exit is not perfectly circular. Figure (c), at a magnification of 60000, shows that the frontside is highly circular and the on-screen measurement shows that it has a diameter of $1.27\ \mu\text{m}$. The frontside figures are taken under an angle of 10° in order to calculate the thickness of the plate at the pinhole. According to the on-screen measurement in Figure (d), the thickness of the plate at the pinhole is $574\ \text{nm} / \tan(10^\circ) = 3.26\ \mu\text{m}$.

Chapter 5

Results and Discussion

This chapter discusses the results of this research. The first section discusses the action of the pinhole and the second section treats the observed spin-orbit interaction. In the third section it is discussed whether or not we have achieved superresolution. For a full systematic overview of the measurements, see Appendix C.

5.1 Pinhole action

The pinhole may well be the most ancient object of study in optics, dating back to Greek and (independently) Chinese writers in the 4th century BC. The first competent ray optics description of the ‘camera obscura’ can be found in the Book of Optics written by one of the most influential Arabic scholars Ibn-al Haytham in the 11th century AC.¹ For the last couple of centuries characterizations of the diffracted image behind a pinhole remained one of the central problems in classical optics. The problem was essentially solved in the 19th century by Kirchhoff’s scalar diffraction theory for pinholes with diameters larger than the wavelength. In the previous chapters, we have used the vectorial version of Kirchoff’s theory

¹See Wikipedia Camera Obscura, accessed 25-11-2019.

to calculate the strongly focused field [71].

In the 20th century, the interest shifted to subwavelength pinholes for which Kirchoff's theory failed. The theory is first adapted to subwavelength holes in optically thin films by Bethe in the 1940s [72] and later, Roberts [73] investigated optically thick films, for which the circular wave-guide modes of the hole were essential to understand the transmission of light through the hole. Bethe's model turned out to be insufficient, which was revealed in the late 90s by measurements of the extraordinary transmission by Ebbesen et al. [74] due to excitations of surface plasmons on the hole edges. This phenomenon generated a lot of interest in surface plasmons and optical transmission through sub-wavelength holes [71, 75] and shows the complexity of optical transmission of small holes.

The pinhole we have utilized in the experiments lies neither in the sub-wavelength regime where $kr \ll 1$, with r the radius of the pinhole and k the wavenumber, nor in the regime where $kr \gg 1$, where we can use Kirchoff's scalar theory. This means we should expect deviations from Kirchoff's theory manifesting as an effect on the optical transmission of each separate vector component [76].

According to Kirchoff's geometrical theory, we expect the pinhole to measure the total intensity incident on the circular aperture that constitutes the pinhole. We simulated this behavior by simply taking the simulated field, as calculated in Chapter 3, and convoluting this field with a circular aperture. Finally, we take the intensity of the calculated convolution of the field. In Figure 5.1, we compared the measured intensity with the simulated intensity. The intensity has been measured with the method described in Chapter 4.

In Figure 5.1 we see that the finite size of the pinhole only becomes relevant for more tightly focused fields, as there is little to no difference between the simulated and measured Gaussian beam profiles for the measurements with the $20\times$ objective. For the strongly focused field, however, we see a larger Gaussian width in the experiment as compared to the simulations (red curve bottom right panel), but the distribution remains fully Gaussian, as we can see from the red Gaussian curve fit in the leftmost panel. The yellow and purple curves in the bottom right panel show the simulated and convoluted field, with either a radial step function transmission (CA, circular aperture) or a Gaussian transmission function (GA, Gaussian aperture). At the simulated effective diameters of the pinhole, there is only a small

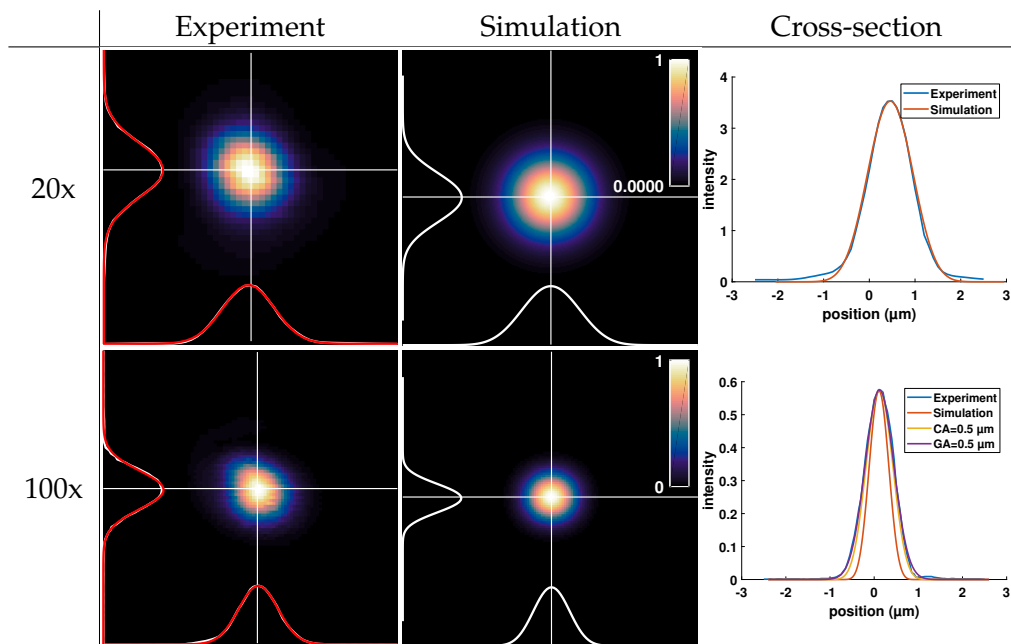


Figure 5.1: In this figure, we compare the measured Gaussian with the simulations. The two rows show measurements with the 20x Olympus objective and the 100x Nikon objective. On the left, the figures show the $5 \times 5 \mu\text{m}$ scan of a focused linearly polarized Gaussian beam, with a resolution of $0.1 \mu\text{m}$ and $0.05 \mu\text{m}$ for the 20x and 100x objective respectively. On the right, cross-sections are plotted with the experiment and simulation. For the 100x objective, the pinhole action has also been plotted with an effective radius of $0.5 \mu\text{m}$. The circular aperture pinhole is simulated here as a step function (CA) or as a Gaussian function (GA) with an effective width. The middle two figures show the simulations, with the lower simulated with the pinhole as a GA of $0.5 \mu\text{m}$. The white curves on the left four figures are cross-sections at the white lines, and the red curve is a Gaussian fit of the white curve.

difference noticeable between the circular aperture or a Gaussian aperture. We can thus use either to simulate the action of the pinhole.² The value of the effective radius of the simulation of the pinhole is $0.5 \mu\text{m}$, which is close to the measured radius of $1.27/2 = 0.64 \mu\text{m}$.³ The widths of simulation (without convolution), and experiment do not agree precisely, as can be seen in the bottom right panel of Figure 5.1, but we see that through an easy step of a convolution with a circular aperture we find almost perfect

²In MATLAB it is much faster to convolute with a boolean array, thus we will use a circular aperture in what follows.

³See Figure 4.6.

agreement with the Gaussian measurement.

For Gaussian beams, we have established that the pinhole functions quite neatly as a geometrical aperture that can be described with Kirchoff's theory. The pinhole captures the intensity profile of the focused beam accurately, with only small deviations from the simulations. However, in the next section it will become clear that Kirchoff's theory is not the full story for pinholes with a radius of the order of the wavelength.

5.2 Spin-orbit interaction

In the measurements with a $\text{NA} > 0.25$ we also observe SO interaction, as predicted in Chapter 3.⁴ In Figure 5.2, we see quite clearly the difference between the combinations of $\ell = 1, s = 1$ ($\text{LG}_{10}|rcp\rangle$) and $\ell = 1, s = -1$ ($\text{LG}_{10}|lcp\rangle$) for the $20\times$ objective ($\text{NA} = 0.4$), which show spin-orbit interaction.⁵ It is interesting to see that the spin-orbit interaction is only observable in the focus. In the top-right two panels of Figure 5.2, we see the spin-orbit interaction persist over approximately $8\ \mu\text{m}$.

In Figure 5.3 and Figure 5.4, we see that the SO effect is much stronger in the experiment than in the simulations of the focused field of a pure LG mode. Especially for the $100\times$ objective, see Figure 5.4, the vortex core is not perfectly in the center and is completely destroyed in the case of opposite OAM and SAM. In fact, it appears that our simulation method of a convolution with a circular step function decreases the SO interaction manifest in the non-zero on-axis intensity.⁶

This can in part be understood by background perturbations in the field that tend to destroy the superoscillatory vortex core [78], and displace the vortex from the center [79], see panel (b) and (e) of Figure 5.5. More importantly, the stronger spin-orbit interaction can be explained by an enhanced transmission of the z -polarization component, which effectively increases the NA and increases the spin-orbit interaction. In Figure 5.5, we have simulated the pinhole as a convolution with a circular aperture in

⁴We discern no difference between the polarization directions for both $4\times$ and $10\times$ objectives. See Figure C.1.

⁵This has also been observed experimentally by Bokor [77].

⁶Compare Figure 5.4 with the intensity in Figure 3.4.

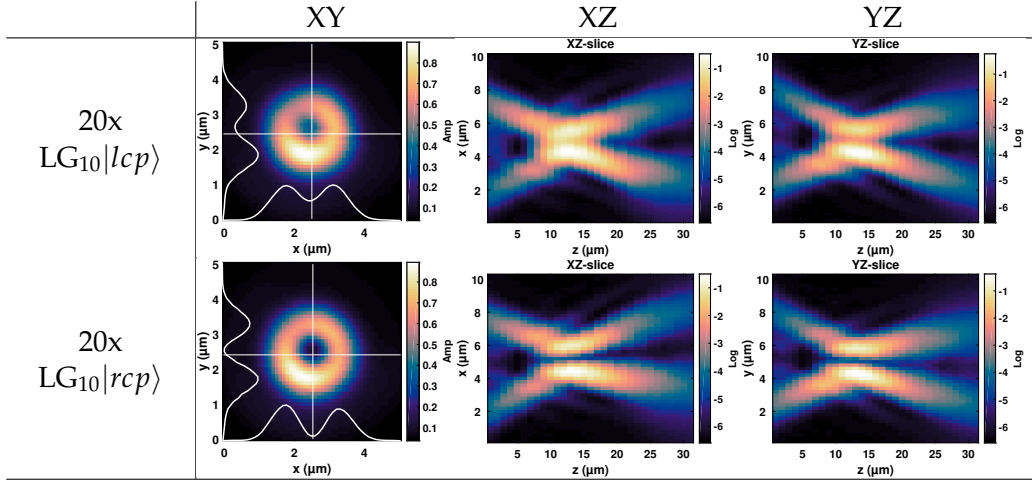


Figure 5.2: Results with the 20 \times Olympus microscope objective. Here, 2D slices are plotted in each direction. Each XY-plane (or z-position) is measured with a resolution of 0.1 μm , while the resolution in z is 1 μm . The intensities for the XZ- and YZ- slices on the right have been plotted logarithmically.

all panels. In Panel (a) and (c) the lcp and rcp with normal convolution are depicted. In panel (b) we have added a small plane wave perturbation to the incident field. In the lower panels, the same fields are depicted, but the optical transmission of the z-component of the *field* is enhanced with a factor of 4. We observe that these two effects of perturbation and enhanced transmission of the z-component can yield results similar to the measurements. We also observe that these two effects do not destroy the vortex core in case of rcp.

All in all, we conclude that deviations from the geometrical circular aperture (Kirchoff's theory) cannot be neglected for transmission function of the pinhole and that small pinholes have an enhanced axial transmission function.⁷

⁷This has been researched in more detail by Yi et al. [76].

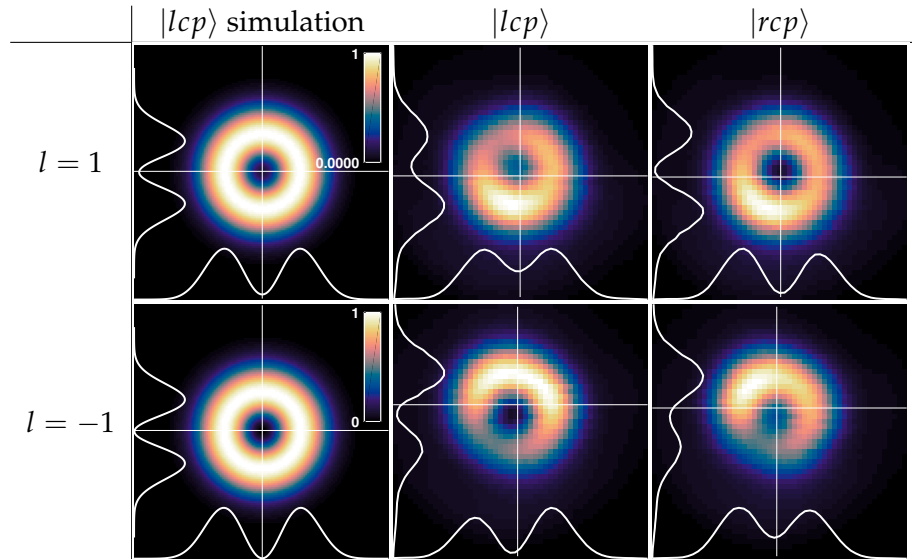


Figure 5.3: Results with the $20\times$ objective for LG_{10} modes with a comparison to the simulations. The images on the left are simulated on a 128×128 grid convoluted with a step function circular aperture with a radius of $0.5 \mu\text{m}$. Each of the four images on the right is scanned with a resolution of $0.1 \mu\text{m}$.

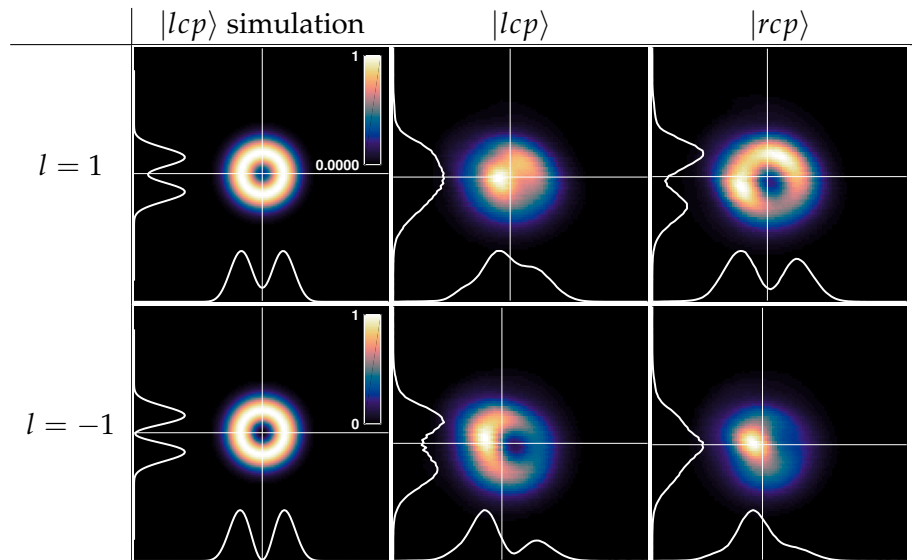


Figure 5.4: Results with the $100\times$ Nikon objective for LG_{10} modes with a comparison to the simulations. The images on the left are simulated on a 128×128 grid convoluted with a step function circular aperture with a radius of $0.5 \mu\text{m}$. Each of the four images on the right is scanned with a resolution of $0.05 \mu\text{m}$.

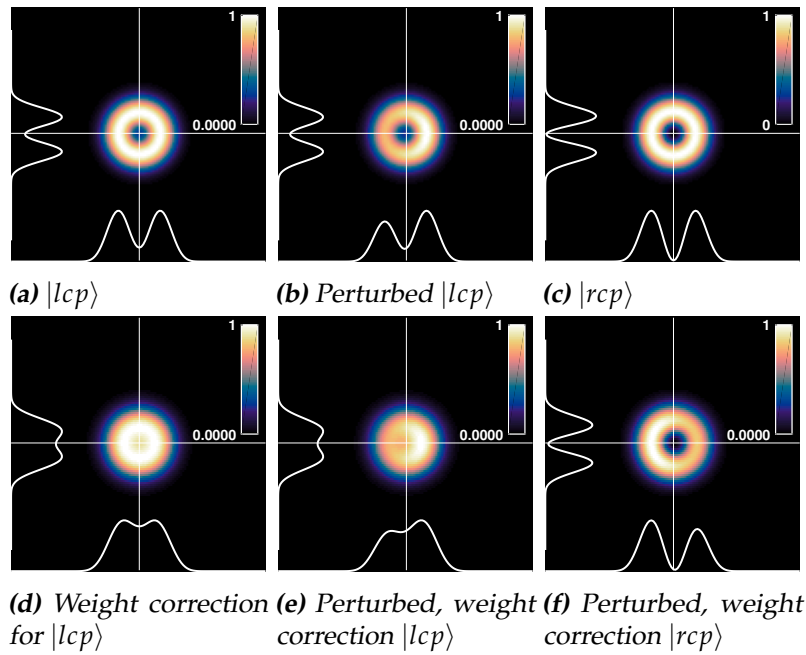


Figure 5.5: Enhanced z -polarization effect of the pinhole convolution. In the top panels, the pinhole is simulated as a circular aperture, while in the bottom panels the pinhole is simulated as a circular aperture with an enhanced transmission of the z -polarization direction with a factor 4. Panel (a) and (d) depict a focused $LG_{10}|lcp\rangle$ mode. Panel (b) and (e) depict the same mode, but perturbed with a plane wave with an amplitude of 0.1 times amplitude of the incident mode. Panel (c) and (f) depict a focused $LG_{10}|rcp\rangle$ mode.

5.3 Superresolution

To establish what is subdiffraction or superresolution, we must first establish the diffraction limit for our focusing apparatus. In theory, this is derived using the numerical aperture of the focusing apparatus according to the Abbe limit: $d = 1.22\lambda/2\text{NA}$.⁸ The measured beam waists in the focal plane are slightly bigger than expected for the high NA objectives, which can be understood with convolution, as discussed in previous section.

Table 5.1: This table lists the experimental beam waist $w_{0,exp}$ parameters, according to 2D fits of the focal planes, the theoretical beam waist $w_{0,theory}$, according to Equation 3.10, and, the theoretical (diffraction) limit d for the given objective's NA.

obj.	NA	$w_{0,exp}$ (μm)	$w_{0,theory}$ (μm)	d (μm)
20 \times	0.4	0.91 ± 0.01	0.936	0.971
50 \times	0.8	0.90 ± 0.01	0.769	0.486
100 \times	0.9	0.49 ± 0.01	0.410	0.432

A higher-order vortex mode is always unstable, and will split up under perturbations [4, 80]. Due to the same perturbations that afflict the measurements of the LG₁₀ mode, we observe the vortices of the LG₂₀ mode slightly split. This allows us to try and measure the distance between the two vortex cores. Evidently, if this distance is smaller than the diffraction limit, the measurement shows superresolution. In Figure 5.6, we can deduce from the anti-parallel OAM and SAM figures (top left and bottom right), which have a vortex core of strength 1, that the vortex size is about 7 pixels or 0.35 μm in diameter. For the parallel figures (top right and bottom left), the vortex core has strength 3 and it is visible that they are slightly split. We estimated the distance between the vortices of the top right figure to be:

$$d_{12} = 0.45 \pm 0.1 \mu\text{m}, \quad d_{13} = 0.4 \pm 0.1 \mu\text{m}, \quad d_{23} = 0.2 \pm 0.1 \mu\text{m}. \quad (5.1)$$

This indicates that we have measured with superresolution, albeit not very far below the diffraction limit. Nevertheless, this is a surprising result, considering that the diameter of the pinhole is 1.27 μm and the measured distances are of the order of the wavelength, and much smaller than the diameter of the pinhole.

⁸It may be more practical, however, to compare with a different measure. The measure more relevant to an underfilled microscope objective is the spot size of the focused Gaussian in the focal plane.

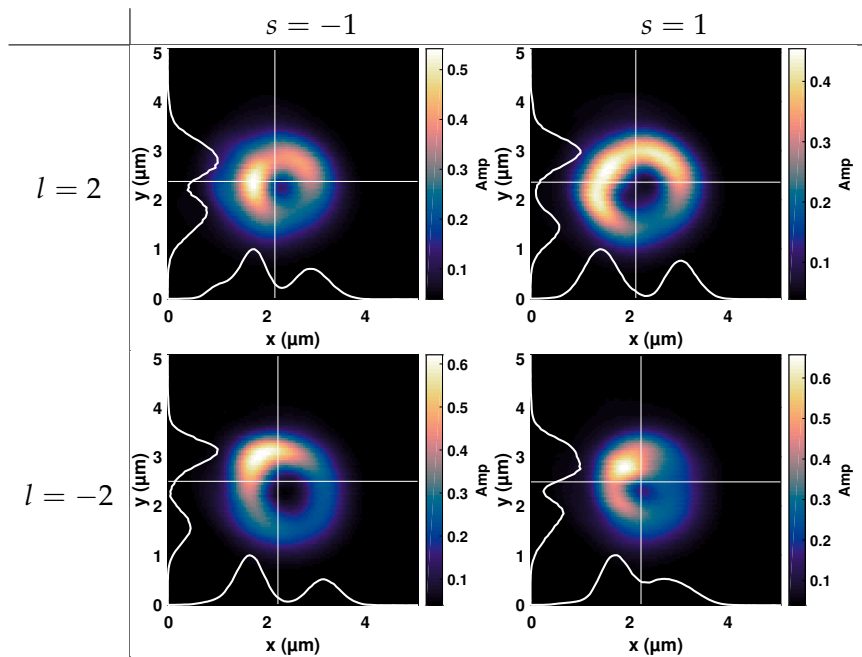


Figure 5.6: Results with the $100\times$ Nikon objective for LG_{20} modes. Each of the four images is scanned with a resolution of $0.05\ \mu\text{m}$. On the left are the incident lcp modes and on the right the rcp modes.

Another argument that the method is a superresolution method, which is perhaps less compelling, is that we can see a vortex structure in the focused beam at all, as this structure is evidently smaller of size than the Gaussian beam. Being able to discern structure smaller than the focused Gaussian is the same as being able to measure with superresolution.

Conclusion and Outlook

6.1 Conclusion

In this thesis, we have seen that it is possible to produce structured fields that remain structured when tightly focused. We measured the structure to be smaller than the diffraction limit. We have been able to show this using a relatively straightforward near field scanning technique using a simple pinhole, which was capable of measuring these structures. Most surprisingly, the pinhole was able to discern structures smaller than its size.

We have also shown several methods to simulate the vectorial focused field, correctly predicting the spin-orbit interaction that was also present in the measurements.

6.2 Outlook

We were able in this thesis to characterize the intensity of the strongly focused field quite accurately using a relatively simple three-dimensional near field scanning technique. However, the precise polarization dependent transmission function of the pinhole is not yet fully characterized. More insight can be gained by varying the pinhole dimensions while keeping

the beam parameters the same. Furthermore, it is probably possible to improve upon the measurement technique by using more sensitive photo-detectors and background control to measure the vortex position more precisely. However, the resolution is ultimately limited by the diameter of the pinhole.

In this thesis, we have used a small aperture to characterize the intensity of the strongly focused field, where the aperture was the subdiffraction probe. It is also possible to characterize the full vectorial field distribution by making use of nanoparticles as the near field scanning probe. By Mie scattering, the light scattering off a nanoparticle will reflect the different vector components of the focused field in the spatial distribution of the scattered light. By collecting the light after the scattering event, one can reconstruct the full vectorial field. This would be the logical step forward for characterizing strongly focused fields on the nanoscale. The method described here has been proposed and implemented by Bauer et al. [10, 58, 81–83]. We planned to implement this method as well, but the good results using the pinhole stopped us from doing so.

Theoretical Derivations

A.1 Optical Propagator

For any wavefront S , we can calculate the optical field at a point \mathbf{r} by integrating over the field at the wavefront together with the optical propagator or Green's function $G(\mathbf{r}, \mathbf{r}')$ [1, pp. 45-47]:

$$E_{\text{out}}(\mathbf{r}) = \iint_S G(\mathbf{r}, \mathbf{r}') E_{\text{in}}(\mathbf{r}') dS. \quad (\text{A.1})$$

From the plane wave solution, of which the amplitude is invariant upon propagation, we may guess that the form of the propagator for such a wave is:

$$G(\mathbf{r}, \mathbf{r}') \propto \frac{1}{s} e^{iks}, \quad (\text{A.2})$$

where $s = |\mathbf{r} - \mathbf{r}'|$. This is a spherical wave. We can calculate the proportionality constant by again considering the propagation of a plane wave. Consider a plane wave traveling in the z -direction from the plane $z = 0$ to a plane far away $kz \gg 1$. In other words, taking $E_{\text{in}} = E_0 e^{ikz - i\omega t}$, then Equation A.1 yields for the point $(0, 0, z)$

$$E_{\text{out}}(0, 0, z) = \iint_S \frac{C}{s} e^{iks} E_0 e^{-i\omega t} dS, \quad (\text{A.3})$$

where we can approximate the exponent

$$s = \sqrt{z^2 + \rho'^2} = z \sqrt{1 + \frac{\rho'^2}{z^2}} \approx z \left(1 + \frac{\rho'^2}{2z^2} + \dots \right), \quad (\text{A.4})$$

where $x'^2 + y'^2 = \rho'^2$. We approximate the denominator with a simple $s \approx z$ to obtain:

$$E_{\text{out}}(0, 0, z) = \frac{E_0 C}{z} e^{i(kz - \omega t)} \iint_S e^{ik \frac{\rho'^2}{2z}} dS. \quad (\text{A.5})$$

Integrating over the whole plane in polar coordinates results in:

$$E_{\text{out}}(0, 0, z) = \frac{2\pi E_0 C}{z} e^{i(kz - \omega t)} \int_0^\infty e^{ik \frac{\rho'^2}{2z}} \rho' d\rho' = i\lambda C E_0 e^{i(kz - \omega t)}. \quad (\text{A.6})$$

In order to keep the plane wave invariant $E_{\text{out}} = E_{\text{in}}$ we must have $C = 1/i\lambda$. Thus, we find the optical propagator in free space to be:

$$G(\mathbf{r}, \mathbf{r}') = \frac{e^{iks}}{i\lambda s}. \quad (\text{A.7})$$

A.2 Fraunhofer Diffraction and the 2D Fourier Transform

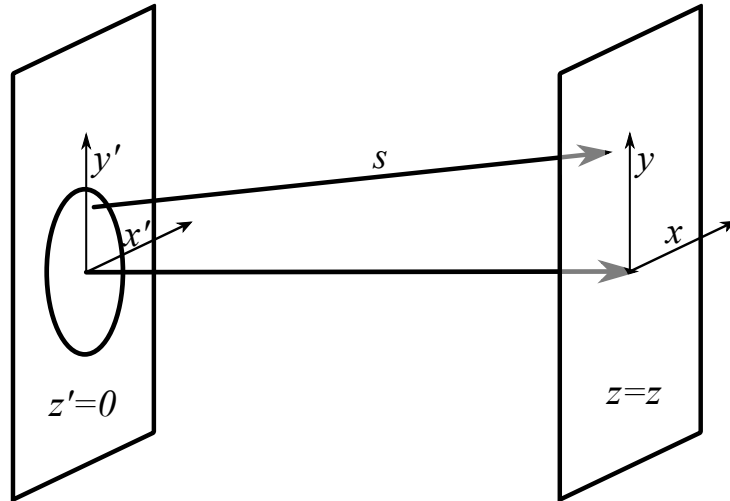


Figure A.1: Geometrical construction for Fraunhofer diffraction.

In Figure A.1 the geometry for Fraunhofer diffraction is shown. This figure shows a general aperture at $z' = 0$ on which a field E_{in} is incident. The aperture is small with respect to the propagation length, or, in other words,

that the source is paraxial. This is called the Fraunhofer regime ($z \gg x', y'$, far-field regime). Here, we can approximate:

$$\begin{aligned} s &= \sqrt{z^2 + (x - x')^2 + (y - y')^2} \approx z + \frac{x^2 + y^2 + y'^2 + x'^2 - 2xx' - 2yy'}{2z} \\ &\approx z + \frac{\rho^2}{2z} - \frac{xx' + yy'}{z}, \end{aligned} \quad (\text{A.8})$$

with $\rho^2 = x^2 + y^2$.¹ Filling this in Equation A.1 we can calculate the diffracted field:

$$\begin{aligned} E_{\text{out}}(\mathbf{r}) &= \iint_S E_{\text{in}}(\mathbf{r}') \frac{e^{ik\left(z + \frac{\rho^2}{2z} - \frac{xx' + yy'}{z}\right)}}{i\lambda z} dS \\ &= -\frac{i}{\lambda z} e^{ik\left(z + \frac{\rho^2}{2z}\right)} \iint_S E_{\text{in}}(\mathbf{r}') e^{-ik\left(\frac{xx' + yy'}{z}\right)} dx' dy'. \end{aligned} \quad (\text{A.9})$$

Note that we can substitute $kx/z = k \sin \theta_x = k_x$ such that:

$$E_{\text{out}}(\mathbf{r}) = -\frac{i}{\lambda z} e^{-ik\left(\frac{\rho^2}{2z} + z\right)} \int_S E_{\text{in}}(\mathbf{r}') e^{-i(k_x x' + k_y y')} dx' dy'. \quad (\text{A.10})$$

This is the Fraunhofer diffraction formula. Given the definition of the Fourier transform:

$$E_{\text{in}}(k_x, k_y) = \int_S E_{\text{in}}(x, y) e^{-i(k_x x + k_y y)} \frac{dx' dy'}{2\pi}, \quad (\text{A.11})$$

we find:

$$E_{\text{out}}(\mathbf{r}) = -\frac{ik}{z} e^{-ik\left(\frac{\rho^2}{2z} + z\right)} \mathcal{F}[E_{\text{in}}(\mathbf{r}')] (k_x, k_y). \quad (\text{A.12})$$

The Fraunhofer diffraction formula is valid in general for scalar fields, but can be generalized for each vector field component, as long as the image itself is also paraxial, which in essence means that the direction of the vector field remains unchanged [2, Ch. 10.3].

The stability of the LG and HG modes can also be understood under paraxial propagation. The Fourier transform of a Gaussian is another Gaussian. Together with the general rules for Fourier Transforms one can deduce the following rule: $\mathcal{F}[x^n f(x)](\omega) = \left(i \frac{d}{d\omega}\right)^n \mathcal{F}[f(x)](\omega)$ which in turn yields that the Fourier transform a polynomial times a Gaussian is again a polynomial of the same order times a Gaussian. In other words, the LG and HG modes are invariant under paraxial propagation.

¹The last approximation step takes us from the Fresnel to the Fraunhofer approximation.

A.3 Vector Transformation Matrix

The transformation in Section 2.2.2:

$$\mathbf{E}_t = (t_s(\mathbf{E}_{in} \cdot \hat{\phi})\hat{\phi} + t_p(\mathbf{E}_{in} \cdot \hat{\rho})\hat{\theta}) \sqrt{\cos \theta}, \quad (\text{A.13})$$

can be expressed as a matrix:

$$\mathbf{E}_t = \mathbf{M}\mathbf{E}_{in} \sqrt{\cos \theta}. \quad (\text{A.14})$$

In spherical output and cylindrical input coordinates we can write:

$$\begin{pmatrix} \hat{r} \\ \hat{\theta} \\ \hat{\phi} \end{pmatrix} = \begin{pmatrix} 0 & 0 & 1 \\ t_p & 0 & 0 \\ 0 & t_s & 0 \end{pmatrix} \begin{pmatrix} \hat{\rho} \\ \hat{\phi} \\ \hat{z} \end{pmatrix}. \quad (\text{A.15})$$

We can also express both sides in Cartesian coordinates by using the rotations matrices for rotating to cylindrical coordinates:

$$\begin{pmatrix} \hat{\rho} \\ \hat{\phi} \\ \hat{z} \end{pmatrix} = \begin{pmatrix} \cos \phi & \sin \phi & 0 \\ -\sin \phi & \cos \phi & 0 \\ 0 & 0 & 1 \end{pmatrix} \begin{pmatrix} \hat{x} \\ \hat{y} \\ \hat{z} \end{pmatrix} \quad (\text{A.16})$$

and from spherical coordinates back to Cartesian coordinates:

$$\begin{pmatrix} \hat{x} \\ \hat{y} \\ \hat{z} \end{pmatrix} = \begin{pmatrix} \sin \theta \cos \phi & \cos \theta \cos \phi & -\sin \phi \\ \sin \theta \sin \phi & \cos \theta \sin \phi & \cos \phi \\ \cos \theta & -\sin \theta & 0 \end{pmatrix} \begin{pmatrix} \hat{r} \\ \hat{\theta} \\ \hat{\phi} \end{pmatrix}, \quad (\text{A.17})$$

such that the full transformation matrix in Cartesian coordinates is:

$$\mathbf{M} = \begin{pmatrix} \sin \theta \cos \phi & \cos \theta \cos \phi & -\sin \phi \\ \sin \theta \sin \phi & \cos \theta \sin \phi & \cos \phi \\ \cos \theta & -\sin \theta & 0 \end{pmatrix} \begin{pmatrix} 0 & 0 & 1 \\ t_p & 0 & 0 \\ 0 & t_s & 0 \end{pmatrix} \begin{pmatrix} \cos \phi & \sin \phi & 0 \\ -\sin \phi & \cos \phi & 0 \\ 0 & 0 & 1 \end{pmatrix} \quad (\text{A.18})$$

$$= \frac{1}{2} \begin{pmatrix} t_s + t_p \cos \theta - (t_s - t_p \cos \theta) \cos 2\phi & -(t_s - t_p \cos \theta) \sin 2\phi & 2 \sin \theta \cos \phi \\ -(t_s - t_p \cos \theta) \sin 2\phi & t_s + t_p \cos \theta + (t_s - t_p \cos \theta) \cos 2\phi & 2 \sin \theta \sin \phi \\ -2t_p \sin \theta \cos \phi & -2t_p \sin \theta \sin \phi & 2 \cos \theta \end{pmatrix}. \quad (\text{A.19})$$

This is the same result as in Lin [50]. Finally, we note that as there is no axial component of the paraxial incident field \mathbf{E}_{in} , we might as well drop the third column and write:

$$\mathbf{M} = \frac{1}{2} \begin{pmatrix} t_s + t_p \cos \theta - (t_s - t_p \cos \theta) \cos 2\phi & -(t_s - t_p \cos \theta) \sin 2\phi \\ -(t_s - t_p \cos \theta) \sin 2\phi & t_s + t_p \cos \theta + (t_s - t_p \cos \theta) \cos 2\phi \\ -2t_p \sin \theta \cos \phi & -2t_p \sin \theta \sin \phi \end{pmatrix}. \quad (\text{A.20})$$

A.4 Full analytic solutions of the azimuthal integral

The Debye integral (Equation 2.25) can be partly solved analytically for the azimuthal integral [1, pp. 59-68]. First, let us write this integral in terms of the coordinates of the sphere ϕ' and θ' :

$$\mathbf{E}_{\text{out}}(\rho, \phi, z) = -\frac{if}{\lambda} \int_0^{\theta_{\text{max}}} \int_0^{2\pi} \mathbf{E}_t(\theta', \phi') e^{ikz \cos \theta' + ik\rho \sin \theta' \cos(\phi' - \phi)} \sin \theta' d\phi' d\theta'. \quad (\text{A.21})$$

If the incident field is polarized along the x-axis, we can then express the transmitted field \mathbf{E}_t on the spherical surface as

$$\mathbf{E}_t(\theta, \phi) = \mathbf{E}_{\text{in}}(\theta, \phi) \frac{\sqrt{\cos \theta}}{2} \begin{pmatrix} 1 + \cos \theta - (1 - \cos \theta) \cos 2\phi \\ -(1 - \cos \theta) \sin 2\phi \\ -2 \cos \phi \sin \theta \end{pmatrix}. \quad (\text{A.22})$$

Similarly, if the incident field is polarized in the y-axis, we obtain:

$$\mathbf{E}_t(\theta, \phi) = \mathbf{E}_{\text{in}}(\theta, \phi) \frac{\sqrt{\cos \theta}}{2} \begin{pmatrix} -(1 - \cos \theta) \sin 2\phi \\ 1 + \cos \theta + (1 - \cos \theta) \cos 2\phi \\ -2 \sin \phi \sin \theta \end{pmatrix}. \quad (\text{A.23})$$

Next, let us calculate the incident field \mathbf{E}_{in} of the first few HG modes in terms of the spherical coordinates (f, θ, ϕ) , where $x = f \sin \theta \cos \phi$, $y = f \sin \theta \sin \phi$ by construction:

$$\begin{aligned} u_{00}^{\text{HG}}(\mathbf{r}) &= e^{-f^2 \sin^2 \theta / w_0^2}, \\ u_{10}^{\text{HG}}(\mathbf{r}) &= 2 \frac{f}{w_0} \sin \theta \cos \phi e^{-f^2 \sin^2 \theta / w_0^2}, \\ u_{01}^{\text{HG}}(\mathbf{r}) &= 2 \frac{f}{w_0} \sin \theta \sin \phi e^{-f^2 \sin^2 \theta / w_0^2}, \\ u_{11}^{\text{HG}}(\mathbf{r}) &= 2 \frac{f^2}{w_0^2} \sin^2 \theta \sin \phi \cos \phi e^{-f^2 \sin^2 \theta / w_0^2}, \\ u_{02}^{\text{HG}}(\mathbf{r}) &= \left(4 \frac{f^2}{w_0^2} \sin^2 \theta \sin^2 \phi - 2\right) e^{-f^2 \sin^2 \theta / w_0^2}, \\ u_{20}^{\text{HG}}(\mathbf{r}) &= \left(4 \frac{f^2}{w_0^2} \sin^2 \theta \sin^2 \phi - 2\right) e^{-f^2 \sin^2 \theta / w_0^2}. \end{aligned} \quad (\text{A.24})$$

Note that inserting these equations into Equation A.21, there is always the following common factor

$$f_W(\theta) \equiv e^{-f^2 \sin^2 \theta / w_0^2} \sqrt{\cos \theta} \sin \theta e^{ikz \cos \theta} \quad (\text{A.25})$$

that we will write as such. The azimuthal integral can now be evaluated with the following two standard integrals:

$$\begin{aligned} \int_0^{2\pi} \cos(n\phi) e^{ix \cos(\phi' - \phi)} d\phi' &= 2\pi(i^n) J_n(x) \cos(n\phi), \\ \int_0^{2\pi} \sin(n\phi) e^{ix \cos(\phi' - \phi)} d\phi' &= 2\pi(i^n) J_n(x) \sin(n\phi), \end{aligned} \quad (\text{A.26})$$

where J_n is the n th-order Bessel function. In principle, what is left is an integral over the single variable θ . Extending upon the definitions of Novotny [1, p. 61], it is useful to introduce these abbreviations for the following integrals:

$$\begin{aligned} I_{00} &= \int_0^{\theta_{\max}} f_W(\theta) (1 + \cos \theta) J_0(k\rho \sin \theta) d\theta, & I_{01} &= \int_0^{\theta_{\max}} f_W(\theta) \sin \theta J_1(k\rho \sin \theta) d\theta, \\ I_{02} &= \int_0^{\theta_{\max}} f_W(\theta) (1 - \cos \theta) J_2(k\rho \sin \theta) d\theta, & I_{10} &= \int_0^{\theta_{\max}} f_W(\theta) \sin^2 \theta J_0(k\rho \sin \theta) d\theta, \\ I_{11} &= \int_0^{\theta_{\max}} f_W(\theta) \sin \theta (1 + 3 \cos \theta) J_1(k\rho \sin \theta) d\theta, & I_{12} &= \int_0^{\theta_{\max}} f_W(\theta) \sin \theta (1 - \cos \theta) J_1(k\rho \sin \theta) d\theta, \\ I_{13} &= \int_0^{\theta_{\max}} f_W(\theta) \sin^2 \theta J_2(k\rho \sin \theta) d\theta, & I_{14} &= \int_0^{\theta_{\max}} f_W(\theta) \sin \theta (1 - \cos \theta) J_3(k\rho \sin \theta) d\theta, \\ I_{15} &= \int_0^{\theta_{\max}} f_W(\theta) \sin^2 \theta (1 - \cos \theta) J_0(k\rho \sin \theta) d\theta, & I_{16} &= \int_0^{\theta_{\max}} f_W(\theta) \sin^3 \theta J_1(k\rho \sin \theta) d\theta, \\ I_{17} &= \int_0^{\theta_{\max}} f_W(\theta) \sin^2 \theta (1 + \cos \theta) J_2(k\rho \sin \theta) d\theta, & I_{18} &= \int_0^{\theta_{\max}} f_W(\theta) \sin^3 \theta J_3(k\rho \sin \theta) d\theta, \\ I_{19} &= \int_0^{\theta_{\max}} f_W(\theta) \sin^2 \theta (1 - \cos \theta) J_4(k\rho \sin \theta) d\theta. \end{aligned}$$

Note that these integrals are still functions of the output coordinates (ρ, z) meaning that we still have to perform each integral numerically for each field point that we want to evaluate. Using these abbreviations, we can finally write down the focal fields of the various modes (neglecting overall normalization $-ikf/2 \cdot (f/w_0)^{n+m}$):

$$E_{00,x}^{\text{HG}}(\mathbf{r}) = \begin{pmatrix} I_{00} + I_{02} \cos 2\varphi \\ I_{02} \sin 2\varphi \\ -2iI_{01} \cos \varphi \end{pmatrix}, \quad E_{00,y}^{\text{HG}}(\mathbf{r}) = \begin{pmatrix} I_{02} \sin 2\varphi \\ I_{00} - I_{02} \cos 2\varphi \\ -2iI_{01} \sin \varphi \end{pmatrix},$$

$$\begin{aligned}
E_{10,x}^{\text{HG}}(\mathbf{r}) &= \begin{pmatrix} i(I_{11} \cos \varphi + I_{14} \cos 3\varphi) \\ -i(I_{12} \sin \varphi - I_{14} \sin 3\varphi) \\ -2I_{10} + 2I_{13} \cos 2\varphi \end{pmatrix}, & E_{10,y}^{\text{HG}}(\mathbf{r}) &= \begin{pmatrix} -i(I_{12} \sin \varphi - I_{14} \sin 3\varphi) \\ i((I_{11} + 2I_{12}) \cos \varphi - I_{14} \cos 3\varphi) \\ 2I_{13} \sin 2\varphi \end{pmatrix}, \\
E_{01,x}^{\text{HG}}(\mathbf{r}) &= \begin{pmatrix} i((I_{11} + 2I_{12}) \sin \varphi + I_{14} \sin 3\varphi) \\ -i(I_{12} \cos \varphi + I_{14} \cos 3\varphi) \\ 2I_{13} \sin 2\varphi \end{pmatrix}, & E_{01,y}^{\text{HG}}(\mathbf{r}) &= \begin{pmatrix} -i(I_{12} \cos \varphi + I_{14} \cos 3\varphi) \\ i(I_{11} \sin \varphi - I_{14} \sin 3\varphi) \\ -2I_{10} - 2I_{13} \cos 2\varphi \end{pmatrix}, \\
E_{11,x}^{\text{HG}}(\mathbf{r}) &= \begin{pmatrix} -2I_{17} \sin 2\varphi - I_{19} \sin 4\varphi \\ I_{19} \cos 4\varphi - I_{15} \\ 2i(I_{18} \sin 3\varphi - I_{16} \sin \varphi) \end{pmatrix}, & E_{11,y}^{\text{HG}}(\mathbf{r}) &= \begin{pmatrix} I_{19} \cos 4\varphi - I_{15} \\ -2I_{17} \sin 2\varphi + I_{19} \sin 4\varphi \\ -2i(I_{18} \cos 3\varphi + I_{16} \cos \varphi) \end{pmatrix},
\end{aligned}$$

$$\begin{aligned}
E_{20,x}^{\text{HG}}(\mathbf{r}) &= \begin{pmatrix} 4I_{10} - 3I_{15} - 2\frac{w_0^2}{f^2}I_{00} - \left(2\frac{w_0^2}{f^2}I_{02} + 4(I_{17} - I_{13})\right) \cos 2\varphi - I_{19} \cos 4\varphi \\ 2\left(2I_{13} - I_{17} - \frac{w_0^2}{f^2}I_{02}\right) \sin 2\varphi - I_{19} \sin 4\varphi \\ 2i\left(2\frac{w_0^2}{f^2}I_{01} - 3I_{16}\right) \cos \varphi + 2iI_{18} \cos 3\varphi \end{pmatrix}, \\
E_{20,y}^{\text{HG}}(\mathbf{r}) &= \begin{pmatrix} 2\left(2I_{13} - I_{17} - \frac{w_0^2}{f^2}I_{02}\right) \sin 2\varphi - I_{19} \sin 4\varphi \\ -I_{15} + 4I_{10} - 2\frac{w_0^2}{f^2}I_{00} - \left(4I_{13} - 2\frac{w_0^2}{f^2}I_{02}\right) \cos 2\varphi + I_{19} \cos 4\varphi \\ 2i\left(2\frac{w_0^2}{f^2}I_{01} - I_{16}\right) \sin \varphi + 2iI_{18} \sin 3\varphi \end{pmatrix}, \\
E_{02,x}^{\text{HG}}(\mathbf{r}) &= \begin{pmatrix} -I_{15} + 4I_{10} - 2\frac{w_0^2}{f^2}I_{00} + \left(4I_{13} - 2\frac{w_0^2}{f^2}I_{02}\right) \cos 2\varphi + I_{19} \cos 4\varphi \\ 2\left(2I_{13} - I_{17} - \frac{w_0^2}{f^2}I_{02}\right) \sin 2\varphi + I_{19} \sin 4\varphi \\ 2i\left(2\frac{w_0^2}{f^2}I_{01} - I_{16}\right) \cos \varphi - 2iI_{18} \cos 3\varphi \end{pmatrix}, \\
E_{02,y}^{\text{HG}}(\mathbf{r}) &= \begin{pmatrix} 2\left(2I_{13} - I_{17} - \frac{w_0^2}{f^2}I_{02}\right) \sin 2\varphi + I_{19} \sin 4\varphi \\ 4I_{10} - 3I_{15} - 2\frac{w_0^2}{f^2}I_{00} + \left(2\frac{w_0^2}{f^2}I_{02} + 4(I_{17} - I_{13})\right) \cos 2\varphi - I_{19} \cos 4\varphi \\ 2i\left(2\frac{w_0^2}{f^2}I_{01} - 3I_{16}\right) \sin \varphi - 2iI_{18} \sin 3\varphi \end{pmatrix},
\end{aligned}$$

where the x or y denotes in which direction the incident beam is polarized. Other polarization directions or the lowest order LG modes can be decomposed in these basic modes. For instance, the first order LG mode can be written as:

$$E_{10,x}^{\text{LG}} = E_{10,x}^{\text{HG}} - iE_{01,x}^{\text{HG}} \quad (\text{A.27})$$

and a rcp HG₁₀ mode is:

$$E_{10,rcp}^{\text{HG}} = E_{10,x}^{\text{HG}} - iE_{10,y}^{\text{HG}}, \quad (\text{A.28})$$

combining to a rcp LG₁₀ mode:

$$E_{10,rcp}^{\text{LG}} = E_{10,x}^{\text{HG}} - iE_{01,x}^{\text{HG}} - iE_{10,y}^{\text{HG}} - E_{01,y}^{\text{HG}}. \quad (\text{A.29})$$

Appendix **B**

Simulation Results

In this appendix, we will list the full simulation results. All figures are simulated with the parameters from Equation 3.2, with the 2DCZT method, and, on a 512×512 grid for the $z = 0$ plane and with the BF method on a 256×256 grid for the $y = 0$ plane. All LG-modes from $\ell, p = 0, 0$ to $2, 2$ are simulated. At the end, the azimuthal and radially polarized doughnut modes are depicted.

Each figure is built up in the following way: The columns indicate the polarization components. The first two columns are in the regular transverse Cartesian basis, whilst the next two columns give the same field in the right-hand and left-hand circular basis. The fifth column is the longitudinal z -component and the sixth column depicts the total intensity, adding the transverse and longitudinal components. There are 8 rows per figure, two for each incident polarization.

B.1 Focal planes of LG modes

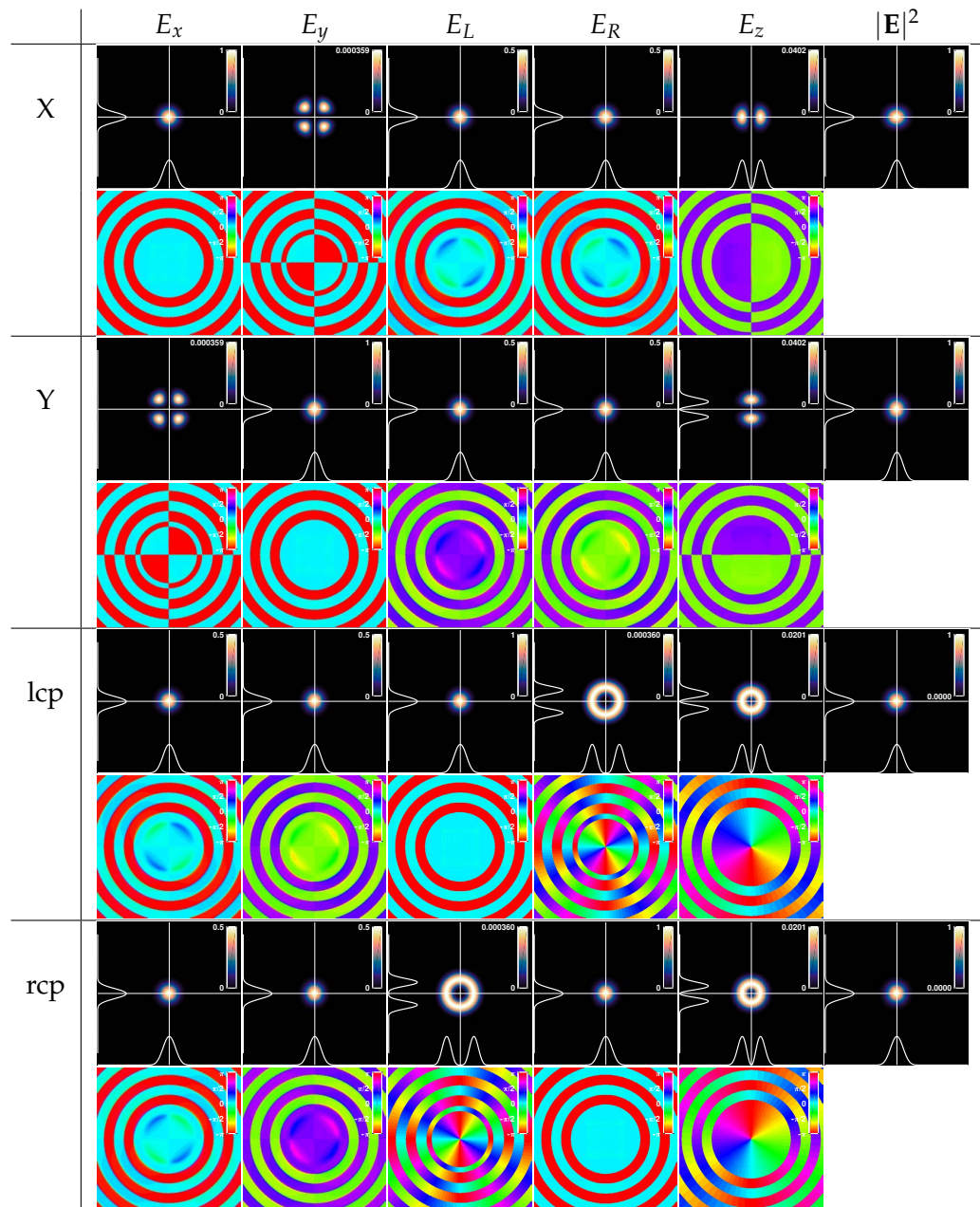


Figure B.1: Focused Gaussian beam.

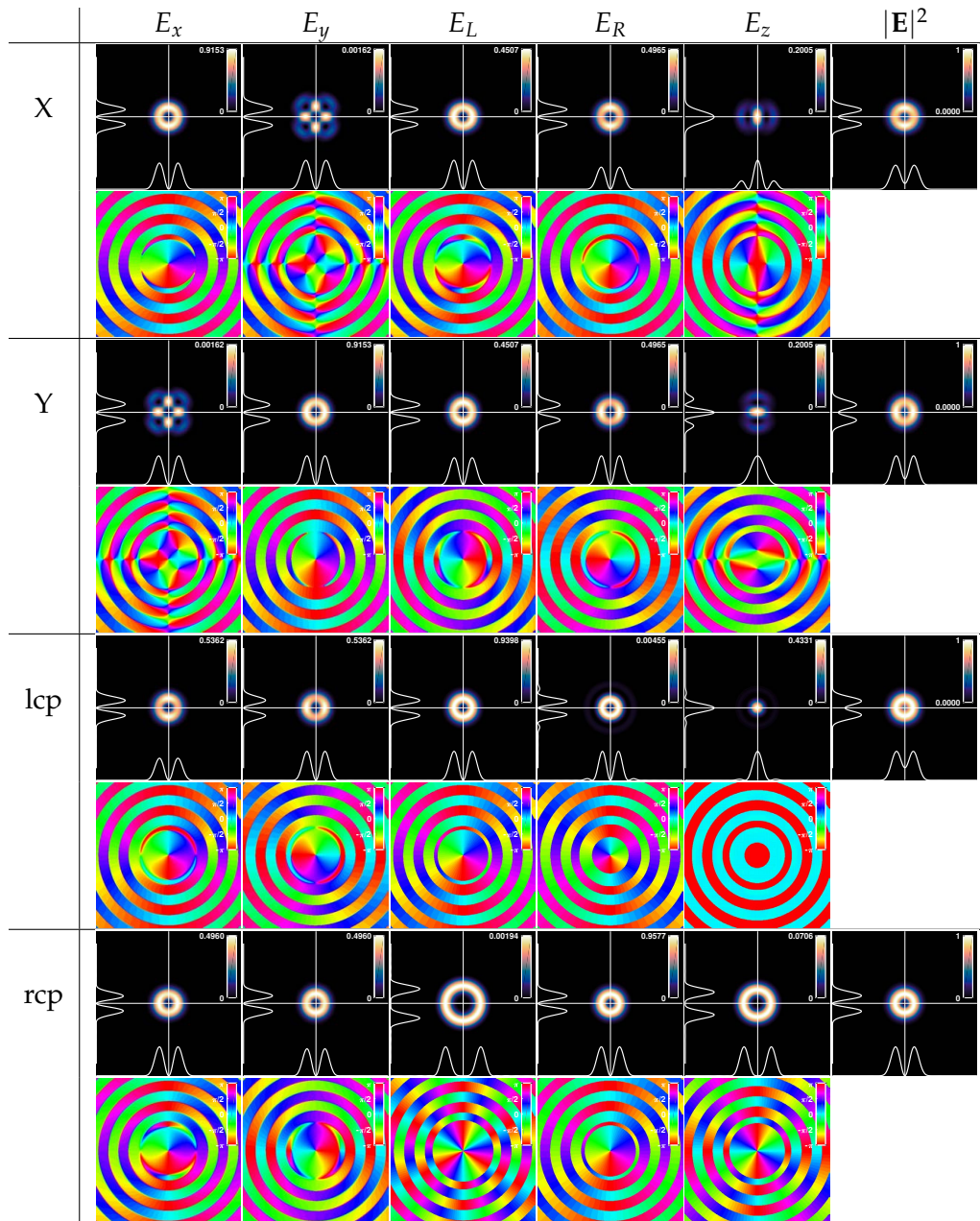


Figure B.2: Focused LG_{10} mode.

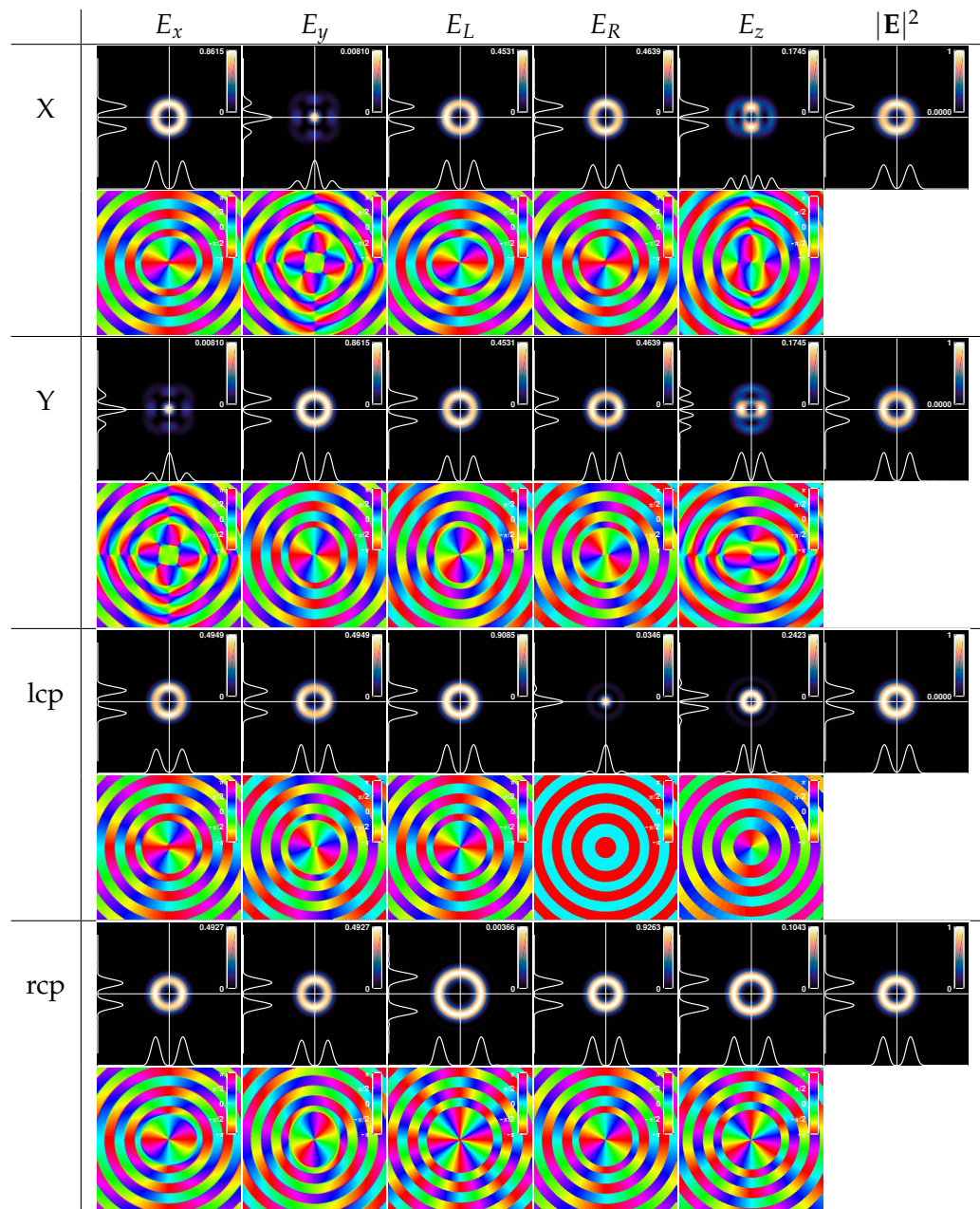


Figure B.3: Focused LG_{20} mode.

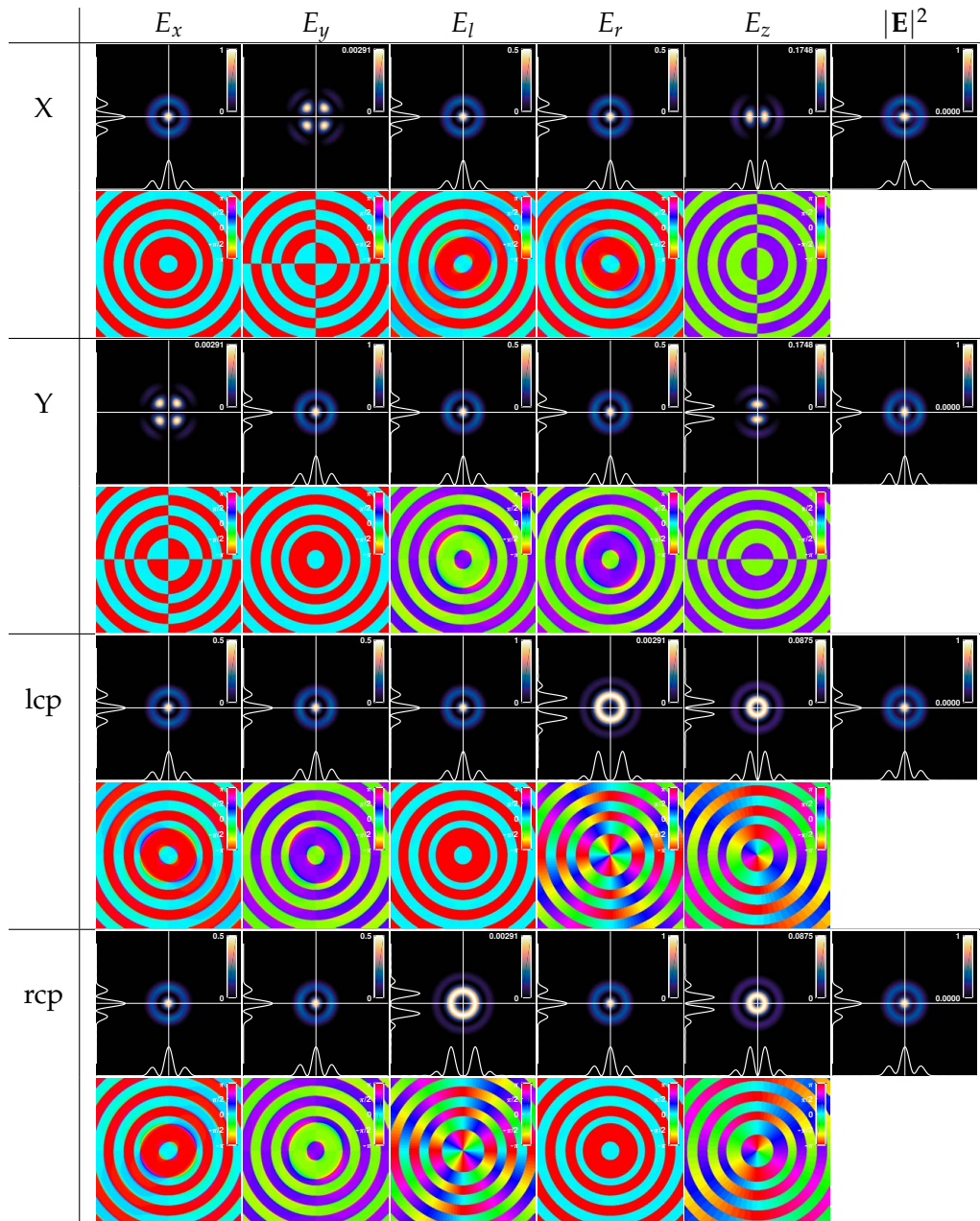


Figure B.4: Focused LG_{01} mode.

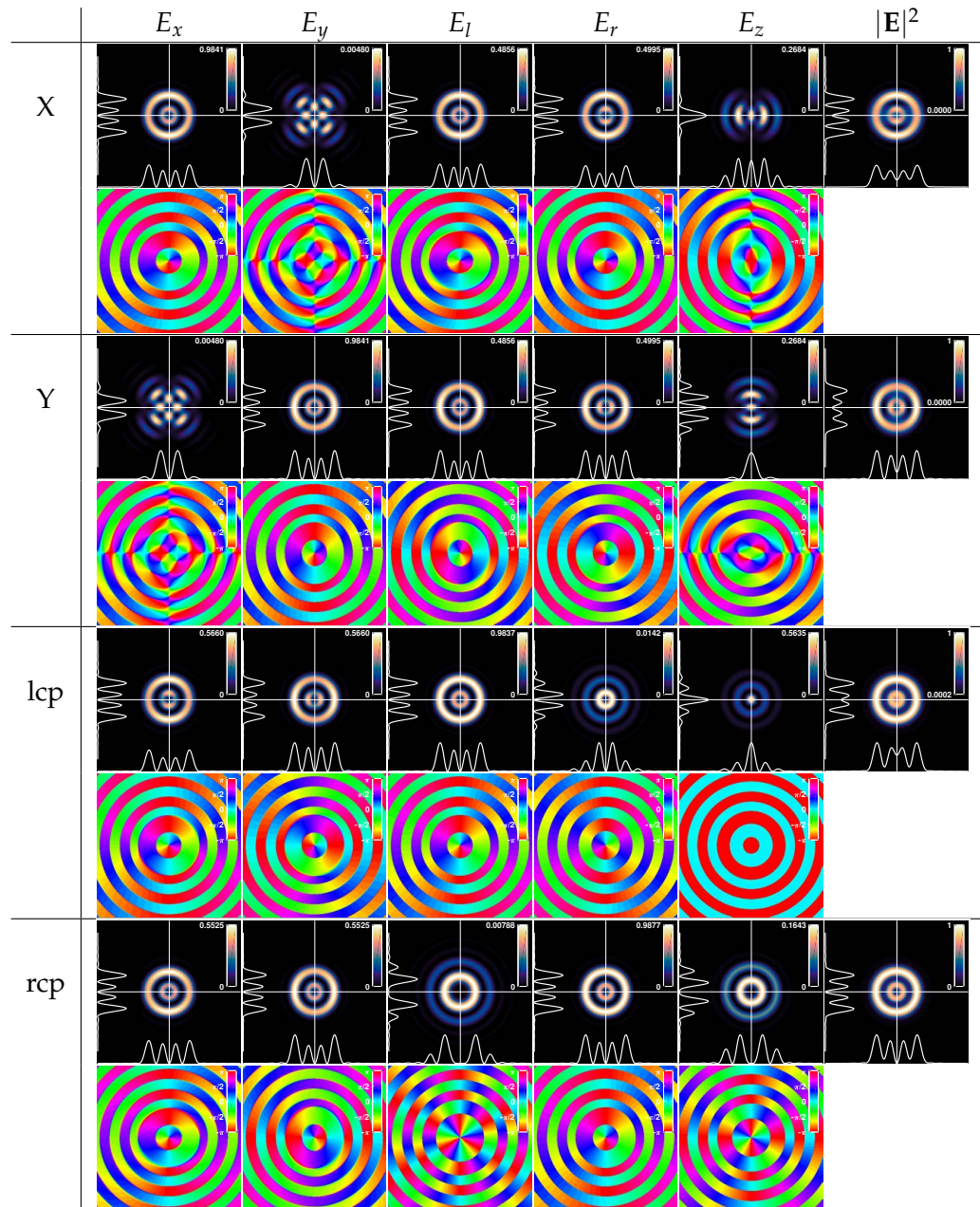


Figure B.5: Focused LG_{11} mode.

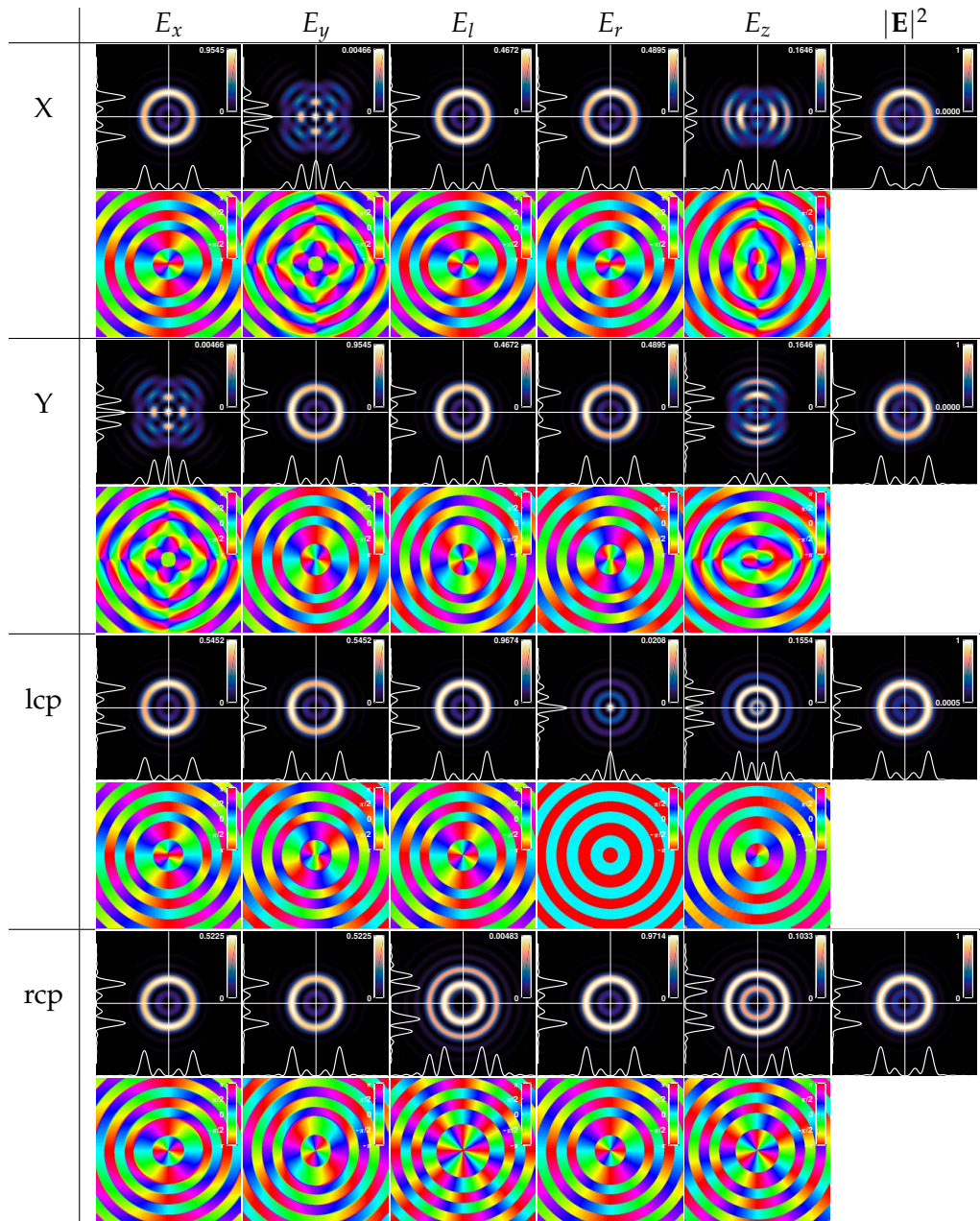


Figure B.6: Focused LG_{21} mode.

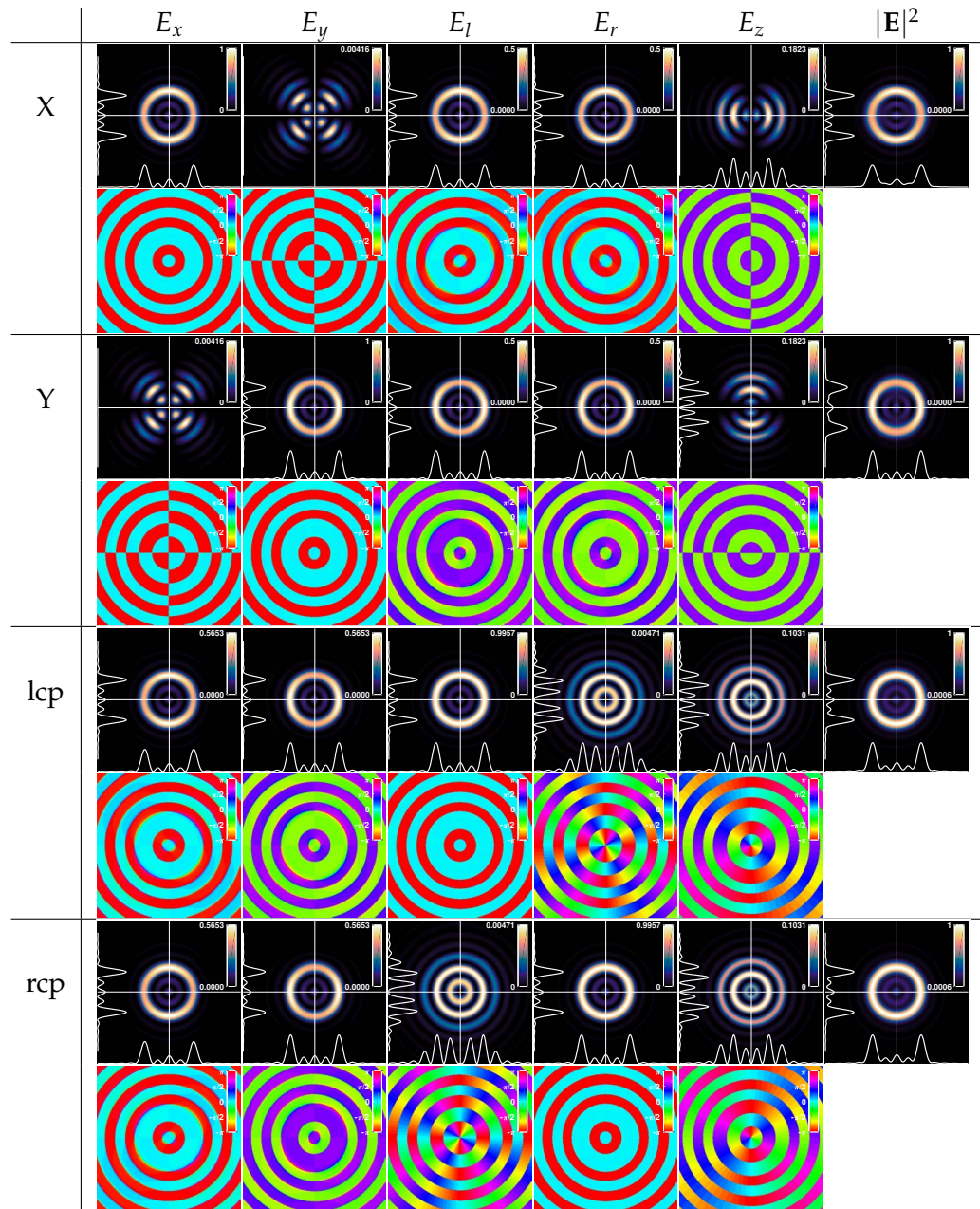


Figure B.7: Focused LG_{02} mode.

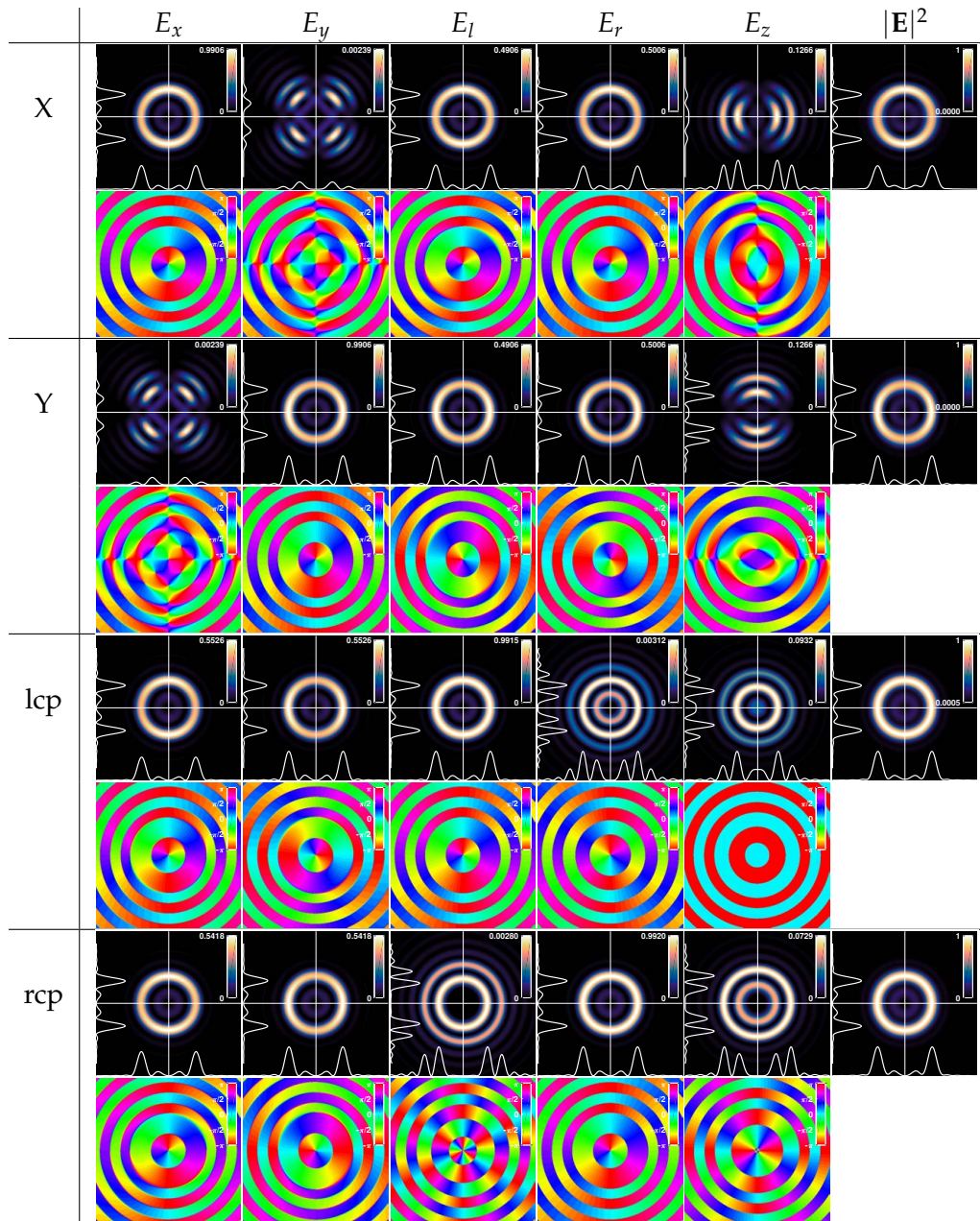


Figure B.8: Focused LG_{12} mode.

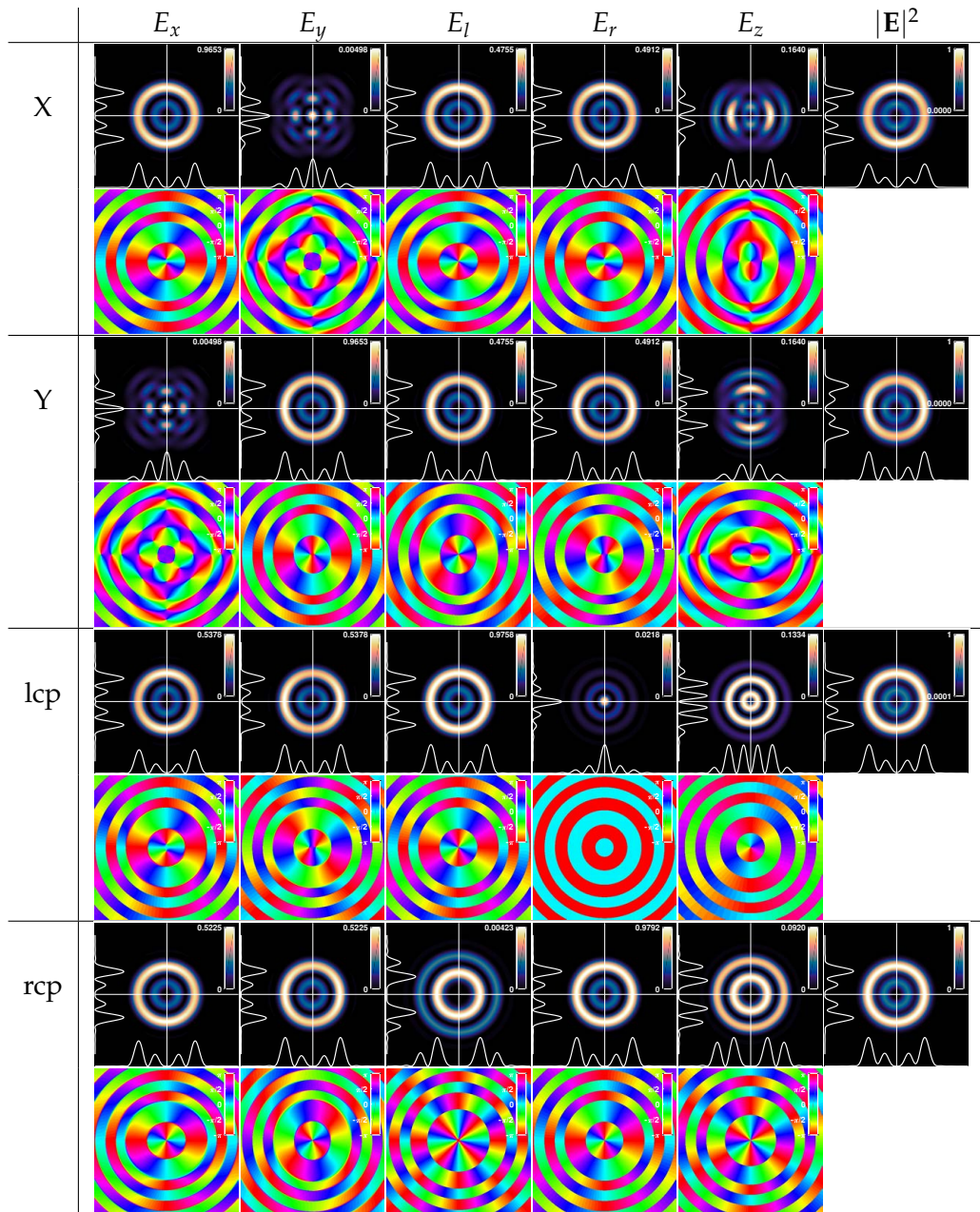


Figure B.9: Focused LG_{22} mode.

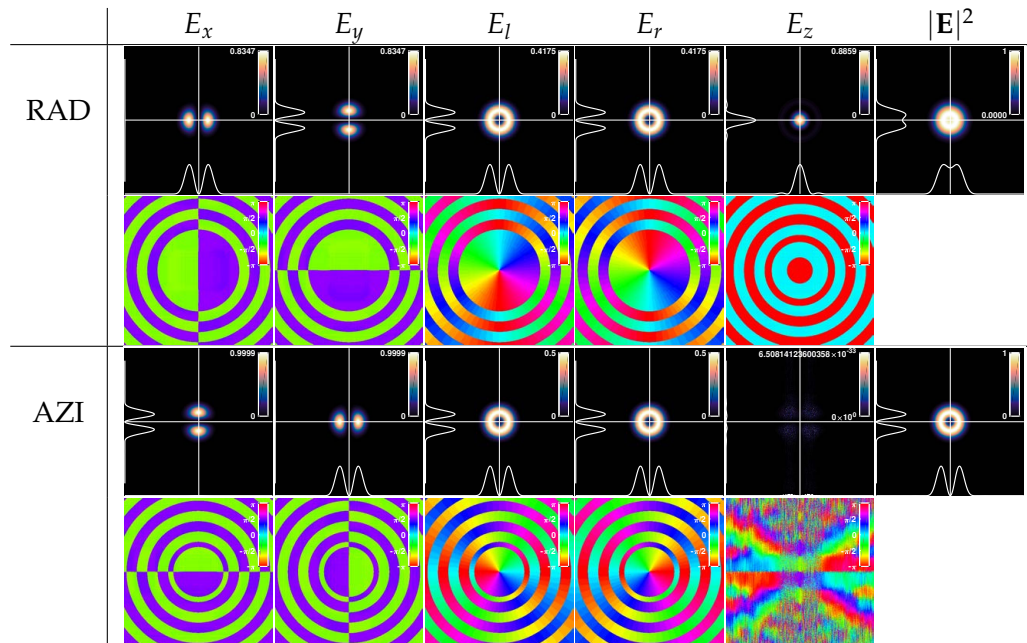
B.1.1 Radially and azimuthally polarized doughnut modes

Figure B.10: Focused azimuthal and radial doughnut modes.

B.2 XZ-slices of LG modes

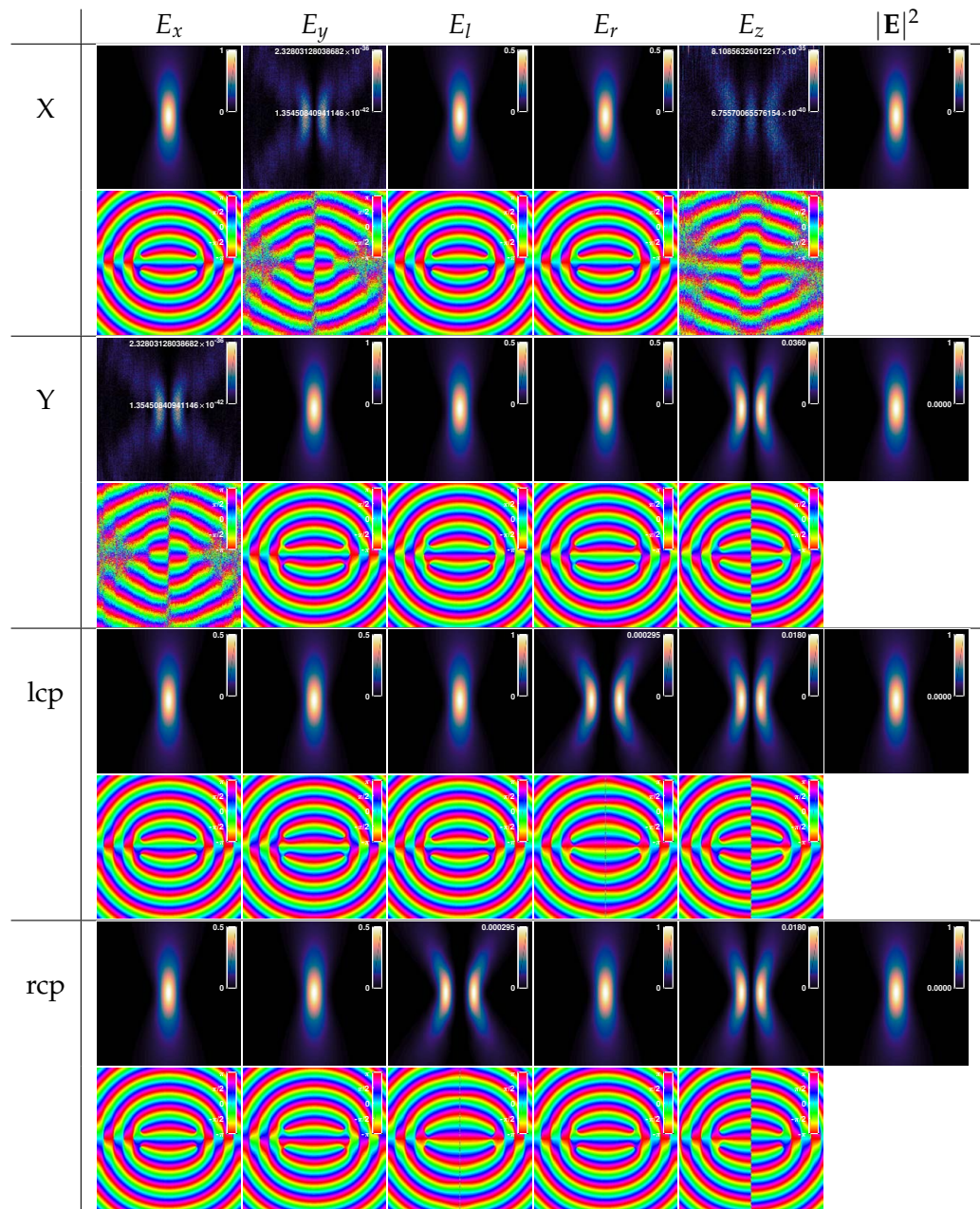


Figure B.11: Focused Gaussian mode.

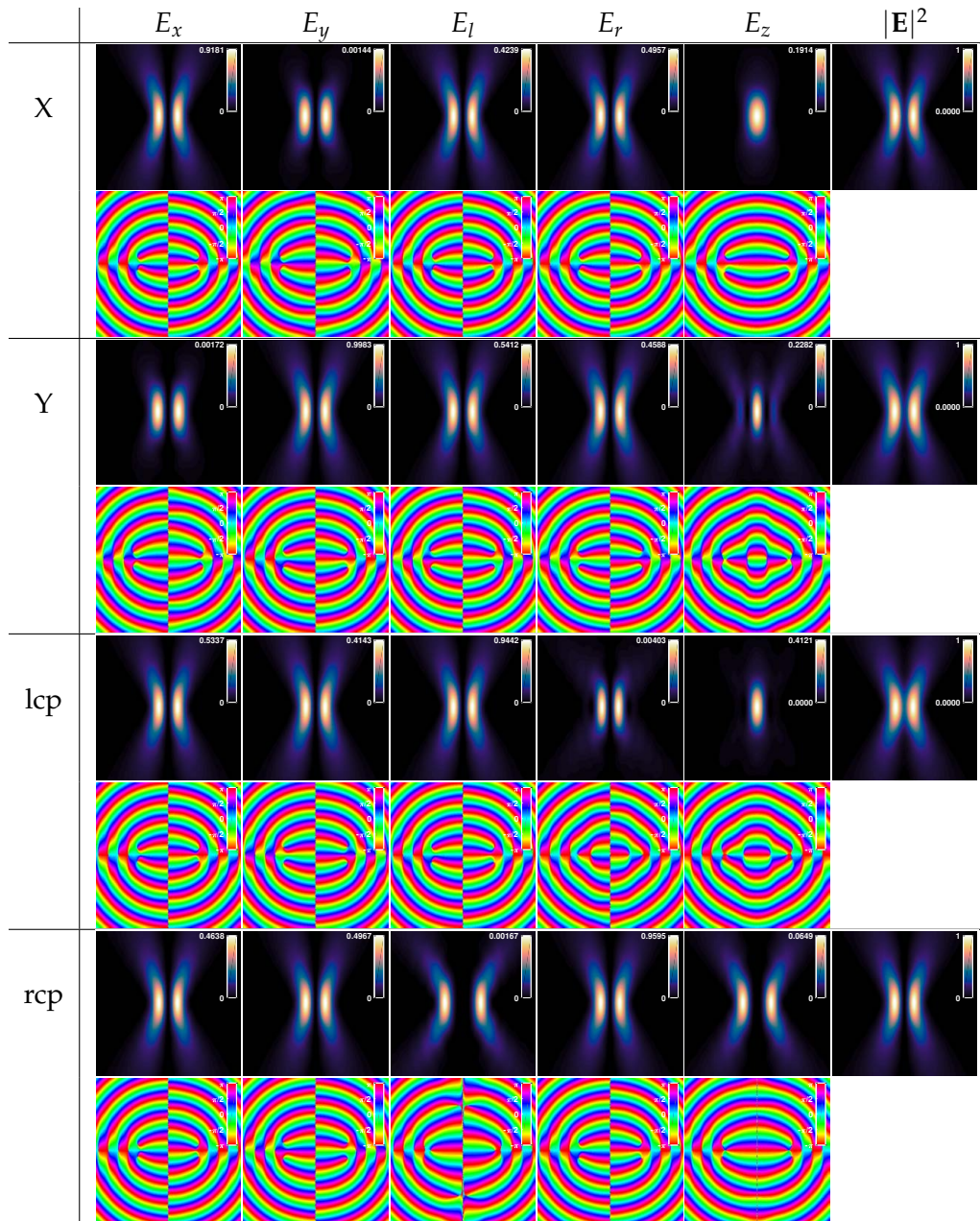


Figure B.12: Focused LG_{10} mode.

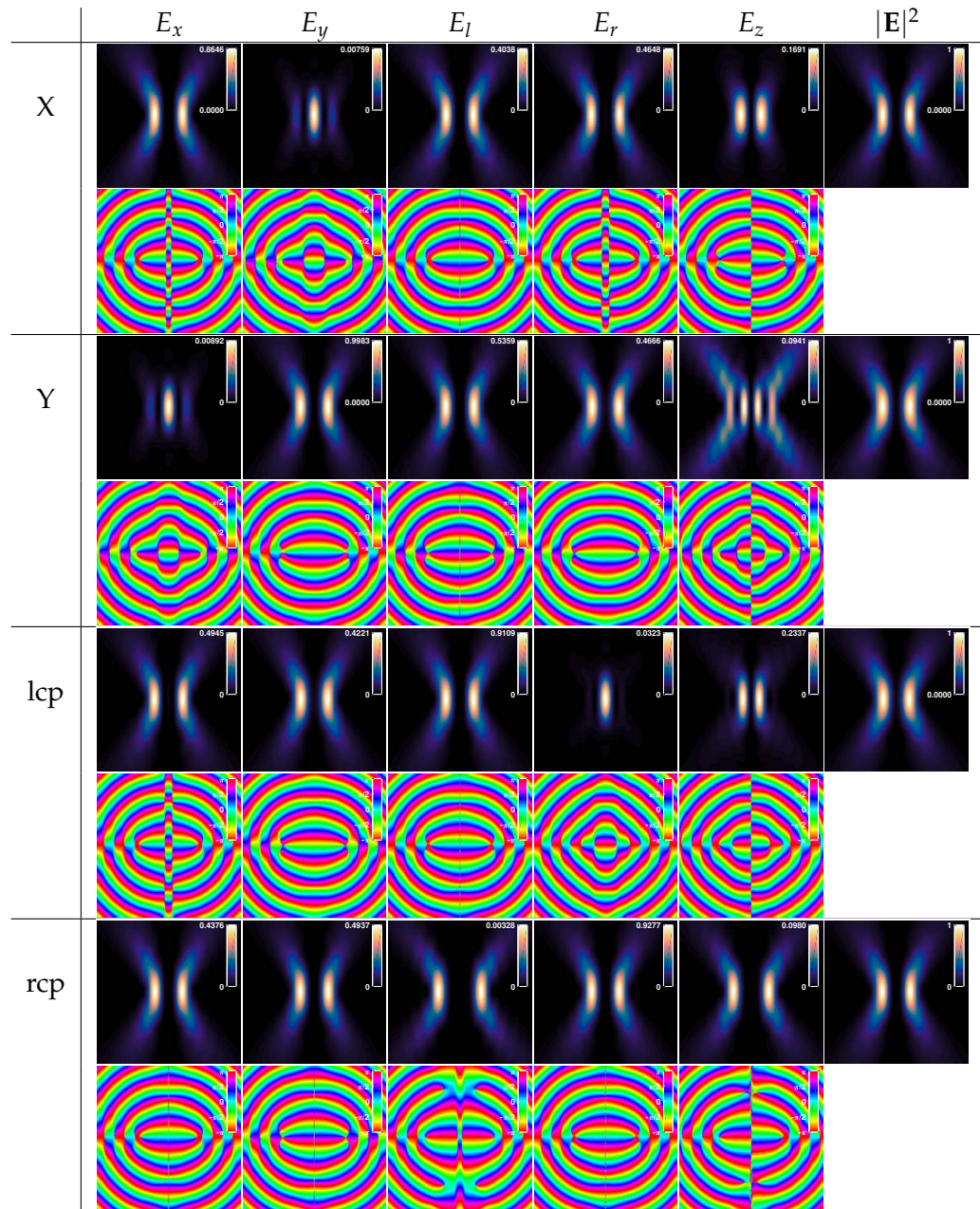


Figure B.13: Focused LG_{20} mode.

Appendix C

Experimental Results

In this appendix we will list the full experimental results from the pinhole measurements. All focal plane figures are of a $5 \times 5 \mu\text{m}$ scan, although the resolution is not always the same. The white curves are 1D cross-sections at the white lines and the red curve is a Gaussian fit. For each image the colorscale is normalized. In reality, the intensity becomes lower for higher-order modes.

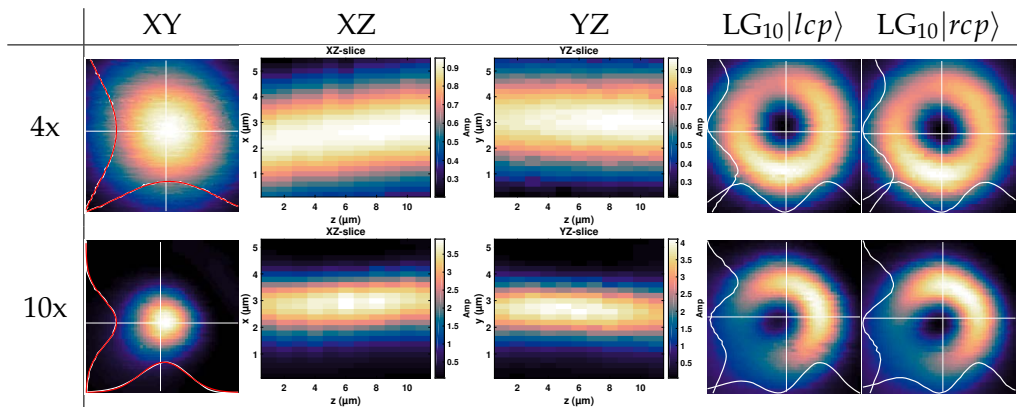


Figure C.1: Results with the $4\times$ and $10\times$ Olympus objective. The left figure is the focal plane image of a focused horizontally polarized Gaussian incident beam with scanning steps of $0.05 \mu\text{m}$ and $0.1 \mu\text{m}$ for the $4\times$ and $10\times$ objective respectively. The next two columns depict slices in the XZ and YZ plane that are $11 \mu\text{m}$ wide with $1 \mu\text{m}$ resolution. The right two columns are focal plane images of a focused incident LG_{10} mode prepared in lcp and rcp respectively, scanned with a resolution of $0.2 \mu\text{m}$ and $0.1 \mu\text{m}$ for the $4\times$ and $10\times$ objective respectively.

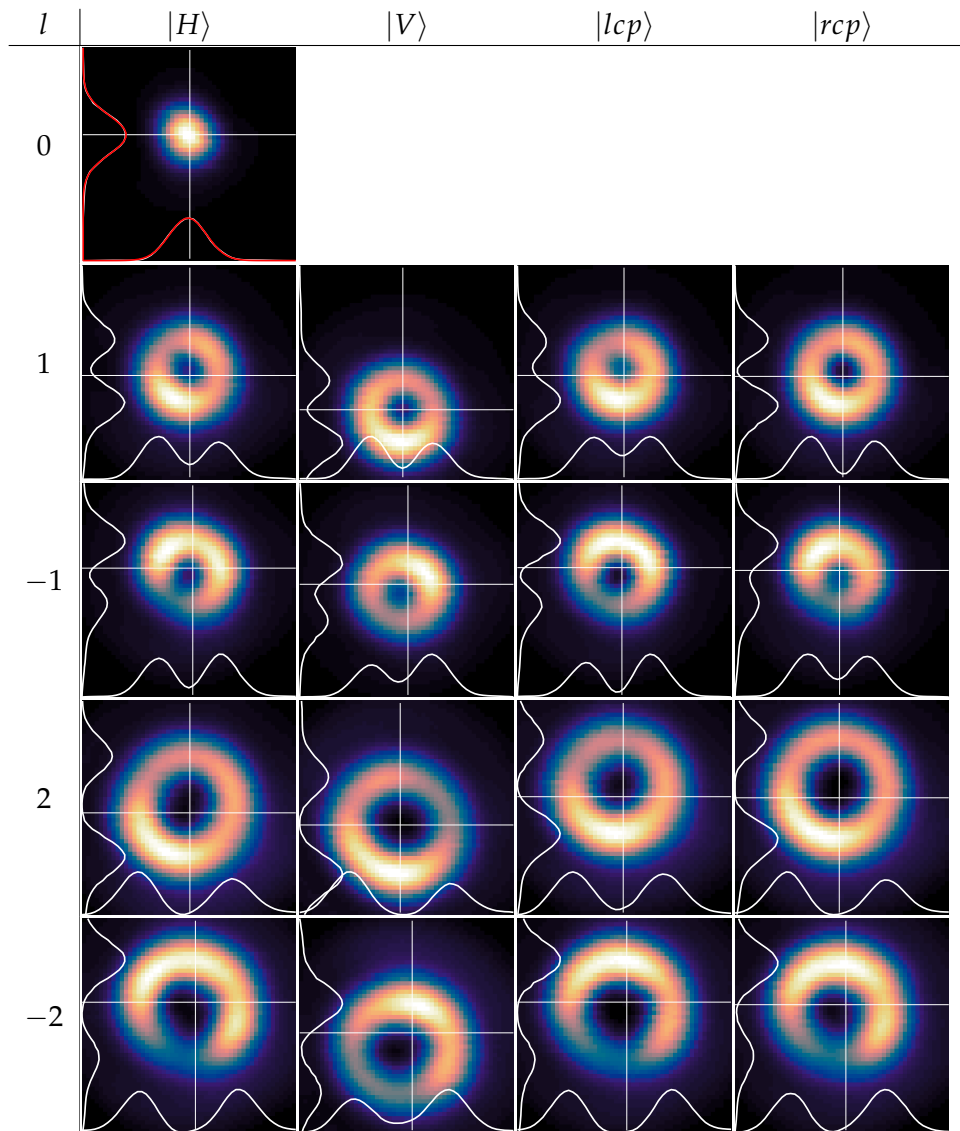


Figure C.2: Results with the $20\times$ Olympus objective. Each image is scanned with a resolution of $0.1\ \mu\text{m}$. The rows denote different azimuthal indices of the incident LG modes and the columns indicate the incident polarization direction.

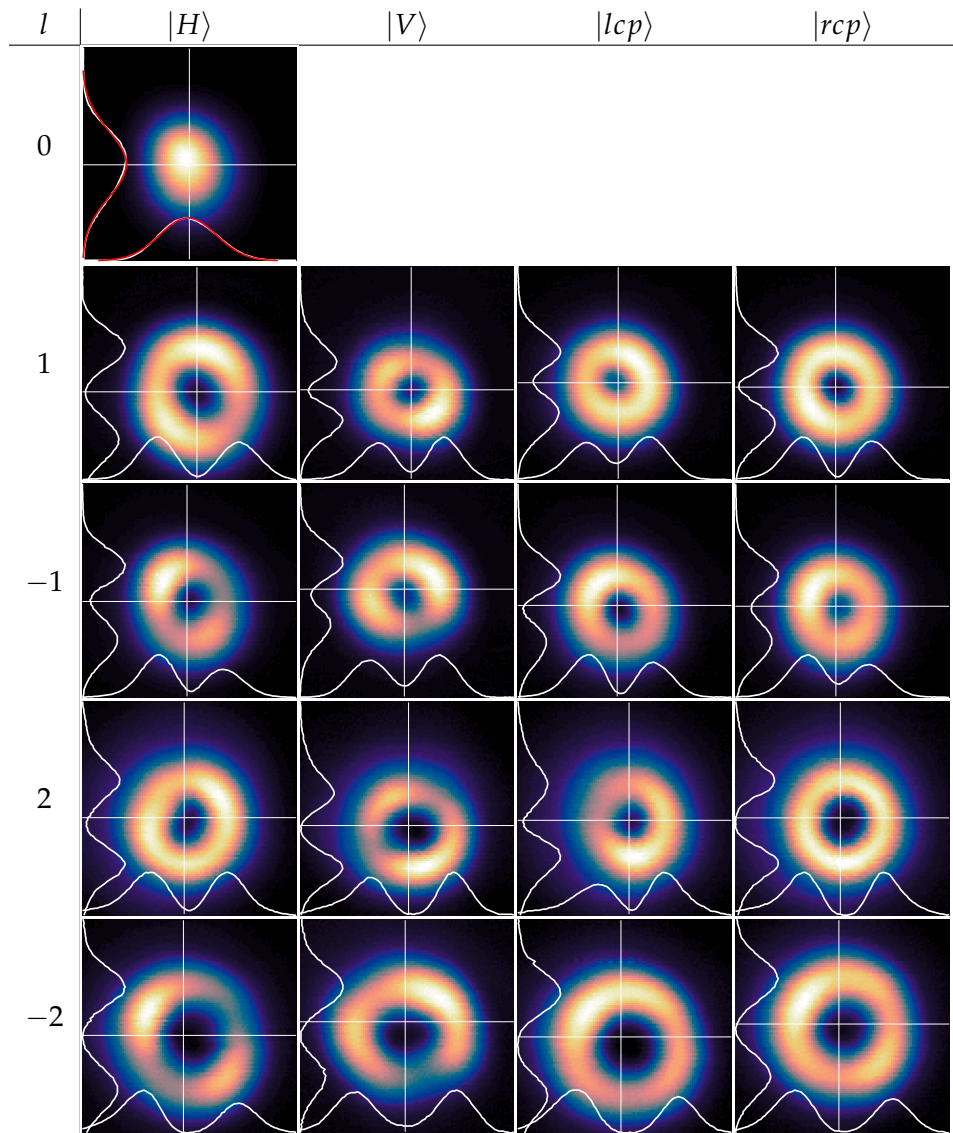


Figure C.3: Results with the 50 \times Nikon objective. Each image is scanned with a resolution of 0.05 μm .

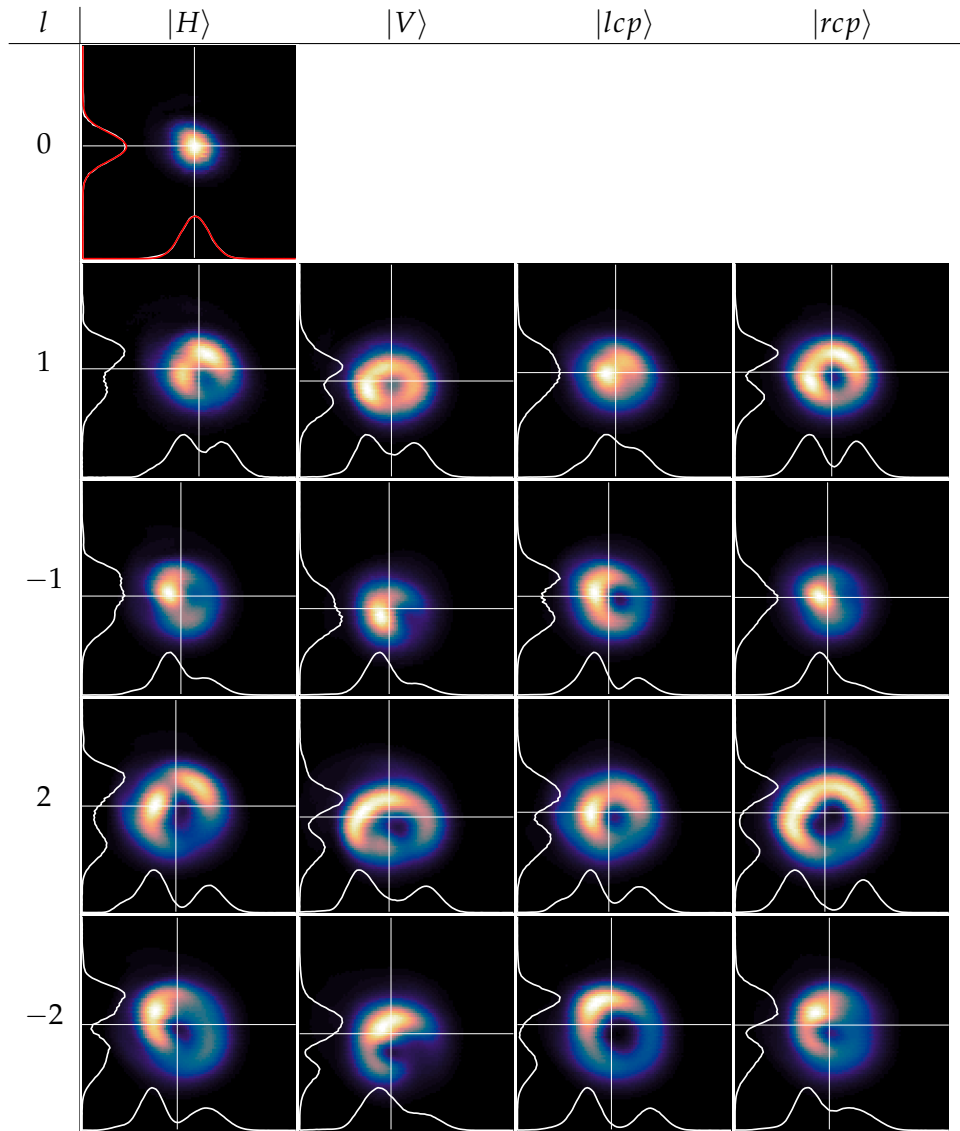


Figure C.4: Results with the $100\times$ Nikon objective. Each image is scanned with a resolution of $0.05\ \mu\text{m}$.

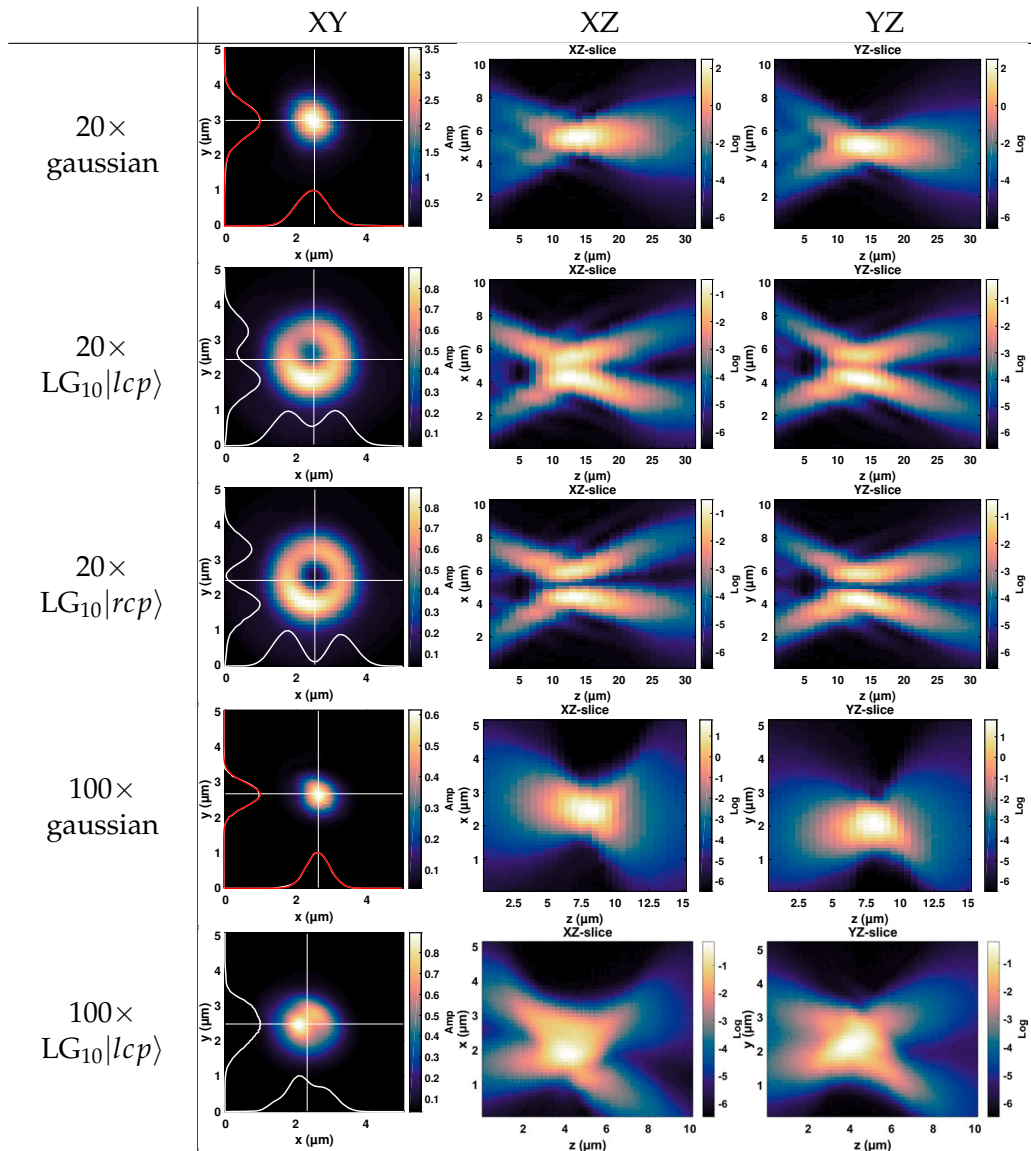


Figure C.5: $20\times$ and $100\times$ Objective 2D slices in each direction. Each plane in z has the same resolution as above, while the resolution in z is $1\ \mu\text{m}$ and $0.1\ \mu\text{m}$ for the $20\times$ and $100\times$ objectives respectively. The intensities for the slices on the right have been plotted logarithmically.

References

- [1] L. Novotny and B. Hecht, *Principles of Nano-Optics*, Cambridge University Press, Cambridge, 2006.
- [2] J. Peatross and M. J. Ware, *Physics of light and optics*, 2016.
- [3] Rayleigh, XXXI. *Investigations in optics, with special reference to the spectroscope*, The London, Edinburgh, and Dublin Philosophical Magazine and Journal of Science **8**, 261 (1879).
- [4] M. Berry et al., *Roadmap on superoscillations*, Journal of Optics **21**, 053002 (2019).
- [5] J. Bechhoefer, *What is superresolution microscopy?*, American Journal of Physics **83**, 22 (2015).
- [6] R. Heintzmann and M. G. L. Gustafsson, *Subdiffraction resolution in continuous samples*, Nature Photonics **3**, 362 (2009).
- [7] L. Schermelleh, R. Heintzmann, and H. Leonhardt, *A guide to super-resolution fluorescence microscopy*, The Journal of Cell Biology **190**, 165 (2010).
- [8] E. Synge, XXXVIII. *A suggested method for extending microscopic resolution into the ultra-microscopic region*, The London, Edinburgh, and Dublin Philosophical Magazine and Journal of Science **6**, 356 (1928).
- [9] F. Simonetti, *Multiple scattering: The key to unravel the subwavelength world from the far-field pattern of a scattered wave*, Physical Review E **73**, 036619 (2006).
- [10] T. Bauer, S. Orlov, U. Peschel, P. Banzer, and G. Leuchs, *Nanointerferometric amplitude and phase reconstruction of tightly focused vector beams*, Nature Photonics **8**, 23 (2014).

-
- [11] G. H. Yuan, E. T. F. Rogers, and N. I. Zheludev, '*Plasmonics*' in free space: observation of giant wavevectors, vortices and energy backflow in superoscillatory optical fields, arXiv:1805.11794 [physics] (2018).
- [12] D. W. Pohl, W. Denk, and M. Lanz, *Optical stethoscopy: Image recording with resolution $\lambda/20$* , Applied Physics Letters **44**, 651 (1984).
- [13] N. I. Zheludev, *What diffraction limit?*, Nature Materials **7**, 420 (2008).
- [14] F. Qin, K. Huang, J. Wu, J. Teng, C.-W. Qiu, and M. Hong, *A Supercritical Lens Optical Label-Free Microscopy: Sub-Diffraction Resolution and Ultra-Long Working Distance*, Advanced Materials **29**, 1602721 (2017).
- [15] E. T. F. Rogers, J. Lindberg, T. Roy, S. Savo, J. E. Chad, M. R. Dennis, and N. I. Zheludev, *A super-oscillatory lens optical microscope for subwavelength imaging*, Nature Materials **11**, 432 (2012).
- [16] R. K. Amineh and G. V. Eleftheriades, *2D and 3D sub-diffraction source imaging with a superoscillatory filter*, Optics Express **21**, 8142 (2013).
- [17] G. Chen, K. Zhang, A. Yu, X. Wang, Z. Zhang, Y. Li, Z. Wen, C. Li, L. Dai, S. Jiang, and F. Lin, *Far-field sub-diffraction focusing lens based on binary amplitude-phase mask for linearly polarized light*, Optics Express **24**, 11002 (2016).
- [18] J. Lindberg, *Mathematical concepts of optical superresolution*, Journal of Optics **14**, 083001 (2012).
- [19] E. T. F. Rogers and N. I. Zheludev, *Optical super-oscillations: sub-wavelength light focusing and super-resolution imaging*, Journal of Optics **15**, 094008 (2013).
- [20] G. Gbur, *Using superoscillations for superresolved imaging and subwavelength focusing*, Nanophotonics **8**, 205 (2019).
- [21] G. Chen, Z.-Q. Wen, and C.-W. Qiu, *Superoscillation: from physics to optical applications*, Light: Science & Applications **8**, 56 (2019).
- [22] E. Betzig and J. K. Trautman, *Near-Field Optics: Microscopy, Spectroscopy, and Surface Modification Beyond the Diffraction Limit*, Science **257**, 189 (1992).
- [23] H. J. Landau and H. O. Pollak, *Prolate Spheroidal Wave Functions, Fourier Analysis and Uncertainty - II*, Bell System Technical Journal **40**, 65 (1961).
- [24] D. Slepian and H. O. Pollak, *Prolate Spheroidal Wave Functions, Fourier Analysis and Uncertainty - I*, Bell System Technical Journal **40**, 43 (1961).
- [25] M. Berry, *Faster than Fourier*, in *Quantum Coherence and Reality; celebrating the 60th Birthday of Yakir Aharonov*, edited by J. Anandan and J. Safko, World Scientific, Singapore, 1994.

- [26] Y. Aharonov, D. Z. Albert, and L. Vaidman, *How the result of a measurement of a component of the spin of a spin-1/2 particle can turn out to be 100*, *Physical Review Letters* **60**, 1351 (1988).
- [27] Y. Aharonov, J. Anandan, S. Popescu, and L. Vaidman, *Superpositions of time evolutions of a quantum system and a quantum time-translation machine*, *Physical Review Letters* **64**, 2965 (1990).
- [28] M. V. Berry and S. Popescu, *Evolution of quantum superoscillations and optical superresolution without evanescent waves*, *Journal of Physics A: Mathematical and General* **39**, 6965 (2006).
- [29] M. R. Dennis, A. C. Hamilton, and J. Courtial, *Superoscillation in speckle patterns*, *Optics Letters* **33**, 2976 (2008).
- [30] Y. Aharonov, F. Colombo, I. Sabadini, D. C. Struppa, and J. Tollaksen, *Some mathematical properties of superoscillations*, *Journal of Physics A: Mathematical and Theoretical* **44**, 365304 (2011).
- [31] M. V. Berry, *Waves near zeros*, in *Conference on Coherence and Quantum Optics*, page CMB1, Rochester, New York, 2007, OSA.
- [32] M. V. Berry, *A note on superoscillations associated with Bessel beams*, *Journal of Optics* **15**, 044006 (2013).
- [33] K. Y. Bliokh, F. J. Rodriguez-Fortuno, F. Nori, and A. V. Zayats, *Spin-orbit interactions of light*, *Nature Photonics* **9**, 796 (2015).
- [34] K. Y. Bliokh, M. A. Alonso, E. A. Ostrovskaya, and A. Aiello, *Angular momenta and spin-orbit interaction of nonparaxial light in free space*, *Physical Review A* **82**, 063825 (2010).
- [35] Y. Zhao, J. S. Edgar, G. D. M. Jeffries, D. McGloin, and D. T. Chiu, *Spin-to-Orbital Angular Momentum Conversion in a Strongly Focused Optical Beam*, *Physical Review Letters* **99**, 073901 (2007).
- [36] E. Greenfield, R. Schley, I. Hurwitz, J. Nemirovsky, K. G. Makris, and M. Segev, *Experimental generation of arbitrarily shaped diffractionless superoscillatory optical beams*, *Optics Express* **21**, 13425 (2013).
- [37] L. Mandel and E. Wolf, *Optical coherence and quantum optics*, Cambridge University Press, Cambridge, 1995.
- [38] J. W. Goodman, *Introduction to Fourier optics*, Roberts & Company, Englewood, Colorado, third edition edition, 2005.
- [39] M. Born, E. Wolf, and A. B. Bhatia, *Principles of optics: electromagnetic theory of propagation, interference and diffraction of light*, Cambridge Univ. Press, Cambridge, 7th ed., 11th reprinting edition, 2016.

-
- [40] M. Lax, W. H. Louisell, and W. B. McKnight, *From Maxwell to paraxial wave optics*, Physical Review A **11**, 1365 (1975).
- [41] A. E. Siegman, *Lasers*, University Science Books, Mill Valley, California, 1986.
- [42] H. Kogelnik and T. Li, *Laser Beams and Resonators*, Applied Optics **5**, 1550 (1966).
- [43] W. L. Erikson and S. Singh, *Polarization properties of Maxwell-Gaussian laser beams*, Physical Review E **49**, 5778 (1994).
- [44] E. Abramochkin and V. Volostnikov, *Beam transformations and nontransformed beams*, Optics Communications **83**, 123 (1991).
- [45] L. Allen, M. W. Beijersbergen, R. J. C. Spreeuw, and J. P. Woerdman, *Orbital angular momentum of light and the transformation of Laguerre-Gaussian laser modes*, Physical Review A **45**, 8185 (1992).
- [46] A. T. O'Neil and J. Courtial, *Mode transformations in terms of the constituent Hermite-Gaussian or Laguerre-Gaussian modes and the variable-phase mode converter*, Optics Communications **181**, 35 (2000).
- [47] Y. Wang, Y. Chen, Y. Zhang, H. Chen, and S. Yu, *Generalised Hermite-Gaussian beams and mode transformations*, Journal of Optics **18**, 055001 (2016).
- [48] C. Rosales-Guzman, B. Ndagano, and A. Forbes, *A review of complex vector light fields and their applications*, Journal of Optics **20**, 123001 (2018).
- [49] E. Abbe, *VII.-On the Estimation of Aperture in the Microscope.*, Journal of the Royal Microscopical Society **1**, 388 (1881).
- [50] J. Lin, O. G. Rodriguez-Herrera, F. Kenny, D. Lara, and J. C. Dainty, *Fast vectorial calculation of the volumetric focused field distribution by using a three-dimensional Fourier transform*, Optics Express **20**, 1060 (2012).
- [51] C. W. McCutchen, *Generalized Aperture and the Three-Dimensional Diffraction Image*, JOSA **54**, 240 (1964).
- [52] M. Leutenegger, R. Rao, R. A. Leitgeb, and T. Lasser, *Fast focus field calculations*, Optics Express **14**, 11277 (2006).
- [53] Richards B., Wolf E., and Gabor Dennis, *Electromagnetic diffraction in optical systems, II. Structure of the image field in an aplanatic system*, Proceedings of the Royal Society of London. Series A. Mathematical and Physical Sciences **253**, 358 (1959).

- [54] Wolf E. and Gabor Dennis, *Electromagnetic diffraction in optical systems - I. An integral representation of the image field*, Proceedings of the Royal Society of London. Series A. Mathematical and Physical Sciences **253**, 349 (1959).
- [55] J. Lin, X.-C. Yuan, S. S. Kou, C. J. R. Sheppard, O. G. Rodriguez-Herrera, and J. C. Dainty, *Direct calculation of a three-dimensional diffracted field*, Optics Letters **36**, 1341 (2011).
- [56] B. R. Boruah and M. A. A. Neil, *Focal field computation of an arbitrarily polarized beam using fast Fourier transforms*, Optics Communications **282**, 4660 (2009).
- [57] H. Gross, W. Singer, and M. Totzeck, *Vector Diffraction*, in *Handbook of Optical Systems*, pages 523–588, John Wiley & Sons, Ltd, 2006.
- [58] T. Bauer, *Probe-based nano-interferometric reconstruction of tightly focused vectorial light fields*, Friedrich-Alexander-Universitaet Erlangen-Nuernberg (FAU), 2017.
- [59] T. A. Nieminen, A. B. Stilgoe, N. R. Heckenberg, and H. Rubinsztein-Dunlop, *Angular momentum of a strongly focused Gaussian beam*, Journal of Optics A: Pure and Applied Optics **10**, 115005 (2008).
- [60] D. Ganic, X. Gan, and M. Gu, *Focusing of doughnut laser beams by a high numerical-aperture objective in free space*, Optics Express **11**, 2747 (2003).
- [61] R. K. Singh, P. Senthilkumaran, and K. Singh, *Focusing of linearly and circularly polarized Gaussian background vortex beams by a high numerical aperture system afflicted with third-order astigmatism*, Optics Communications **281**, 5939 (2008).
- [62] V. V. Klimov, D. Bloch, M. Ducloy, and J. R. Rios Leite, *Mapping of focused Laguerre-Gauss beams: The interplay between spin and orbital angular momentum and its dependence on detector characteristics*, Physical Review A **85**, 053834 (2012).
- [63] K. S. Youngworth and T. G. Brown, *Focusing of high numerical aperture cylindrical-vector beams*, Optics Express **7**, 77 (2000).
- [64] N. R. Heckenberg, R. McDuff, C. P. Smith, and A. G. White, *Generation of optical phase singularities by computer-generated holograms*, Optics Letters **17**, 221 (1992).
- [65] N. R. Heckenberg, R. McDuff, C. P. Smith, H. Rubinsztein-Dunlop, and M. J. Wegener, *Laser beams with phase singularities*, Optical and Quantum Electronics **24**, S951 (1992).

-
- [66] J. A. Davis, J. Guertin, and D. M. Cottrell, *Diffraction-free beams generated with programmable spatial light modulators*, *Applied Optics* **32**, 6368 (1993).
- [67] J. A. Davis, D. M. Cottrell, J. Campos, M. J. Yzuel, and I. Moreno, *Encoding amplitude information onto phase-only filters*, *Applied Optics* **38**, 5004 (1999).
- [68] J. Leach, M. R. Dennis, J. Courtial, and M. J. Padgett, *Vortex knots in light*, *New Journal of Physics* **7**, 55 (2005).
- [69] T. Ando, Y. Ohtake, N. Matsumoto, T. Inoue, and N. Fukuchi, *Mode purities of Laguerre-Gaussian beams generated via complex-amplitude modulation using phase-only spatial light modulators*, *Optics Letters* **34**, 34 (2009).
- [70] E. Bolduc, N. Bent, E. Santamato, E. Karimi, and R. W. Boyd, *Exact solution to simultaneous intensity and phase encryption with a single phase-only hologram*, *Optics Letters* **38**, 3546 (2013).
- [71] C. Genet and T. W. Ebbesen, *Light in tiny holes*, *Nature* **445**, 39 (2007).
- [72] H. A. Bethe, *Theory of Diffraction by Small Holes*, *Physical Review* **66**, 163 (1944).
- [73] A. Roberts, *Electromagnetic theory of diffraction by a circular aperture in a thick, perfectly conducting screen*, *JOSA A* **4**, 1970 (1987).
- [74] T. W. Ebbesen, H. J. Lezec, H. F. Ghaemi, T. Thio, and P. A. Wolff, *Extraordinary optical transmission through sub-wavelength hole arrays*, *Nature* **391**, 667 (1998).
- [75] F. J. Garcia-Vidal, L. Martin-Moreno, T. W. Ebbesen, and L. Kuipers, *Light passing through subwavelength apertures*, *Reviews of Modern Physics* **82**, 729 (2010).
- [76] J.-M. Yi, A. Cuche, F. de Leon-Perez, A. Degiron, E. Laux, E. Devaux, C. Genet, J. Alegret, L. Martin-Moreno, and T. W. Ebbesen, *Diffraction Regimes of Single Holes*, *Physical Review Letters* **109**, 023901 (2012).
- [77] N. Bokor, Y. Iketaki, T. Watanabe, and M. Fujii, *Investigation of polarization effects for high-numerical-aperture first-order Laguerre-Gaussian beams by 2D scanning with a single fluorescent microbead*, *Optics Express* **13**, 10440 (2005).
- [78] M. V. Berry, *Suppression of superoscillations by noise*, *Journal of Physics A: Mathematical and Theoretical* **50**, 025003 (2016).
- [79] J. P. Torres, A. Alexandrescu, and L. Torner, *Quantum spiral bandwidth of entangled two-photon states*, *Physical Review A* **68**, 050301 (2003).
-

-
- [80] F. Ricci, W. Löffler, and M. van Exter, *Instability of higher-order optical vortices analyzed with a multi-pinhole interferometer*, *Optics Express* **20**, 22961 (2012).
- [81] T. Bauer, P. Banzer, E. Karimi, S. Orlov, A. Rubano, L. Marrucci, E. Santamato, R. W. Boyd, and G. Leuchs, *Observation of optical polarization Möbius strips*, *Science* **347**, 964 (2015).
- [82] T. Bauer, P. Banzer, F. Bouchard, S. Orlov, L. Marrucci, E. Santamato, R. W. Boyd, E. Karimi, and G. Leuchs, *Multi-twist polarization ribbon topologies in highly-confined optical fields*, *arXiv:1901.11337 [physics]* (2019).
- [83] M. Neugebauer, P. Wozniak, A. Bag, G. Leuchs, and P. Banzer, *Polarization-controlled directional scattering for nanoscopic position sensing*, *Nature Communications* **7**, 11286 (2016).